Experimental and numerical investigation of split sleeve cold expansion of AZ31B magnesium alloy

by

Sasan Faghih

A thesis

presented to the University of Waterloo

in fulfillment of the

thesis requirement for the degree of

Master of Applied Science

in

Mechanical and Mechatronics Engineering

Waterloo, Ontario, Canada, 2018

Author's declaration

I hereby declare that I am the sole author of this thesis. This is a true copy of the thesis, including any required final revisions, as accepted by my examiners.

I understand that my thesis may be made electronically available to the public.

Abstract

The serious pollution problem caused by transportation can cause critical environmental effect such as global warming. This has drawn attention towards lighter materials for use in the transportation industry. Magnesium as the lightest structural metal has been very attractive for both researchers and industry. Use of magnesium in the transportation industry for non-structural components goes back to the 1930’s, but recently it has been under investigation for load bearing component, in which they are exposed to cyclic loading and therefore are subject to fatigue failure. Cold expansion is one of the well-known techniques for enhancing the fatigue properties notched specimen, which is used widely in aerospace.

For the first time, the feasibility of performing cold expansion on commercial AZ31B magnesium sheet is studied in this research and presented herein. Optimizing the process from the fatigue point of view is done. In order to model the process, a numerical method called variable material property (VMP), with capability of considering actual material behavior, and a finite element software, ABAQUS, were used. To verify these models, two experimental measurements have been done, using digital image correlation (DIC) technique to capture the radial displacement around the notch during loading, and residual stress measurement by X-ray diffraction method after unloading. To obtain the material behavior needed in VMP method, tension-compression and compression-tension loading-unloading tests were performed on the material.

It was shown that split sleeve cold expansion can significantly improve the fatigue life, by postponing crack initiation and decreasing the rate of crack propagation, compared with as-received notched sample. The fatigue life improvement factor gets higher in high cycle regime. In low cycle fatigue, the improvement factor is roughly 2.5x, while in high cycle it gets up to an order of magnitude. It was also shown that the optimum degree of cold expansion percentage was 5 % and 6% for 4 mm and 3.18 mm sheet, respectively. The effect of cold expansion on crack initiation and propagation life was examined using DIC technique. Fractography revealed that on untreated samples, crack initiation occurred on the notch surface, while in the samples with the optimum degree of cold expansion the crack initiation occurs internally and away from the notch surface. This has been attributed to the residual stresses induced in cold expansion process.

Acknowledgement

I would like to show my greatest appreciation to my supervisor, Professor Hamid Jahed, for his valuable advice, support, and motivation during my MASc. program.

I hereby express my sincere gratitude to my colleague, Dr. Behzad Behravesh, for his invaluable support, advice, suggestions. I also would like to offer my special thanks to my other colleagues, Amir Yazdanmehr for his help in XRD residual stress measurement, Dr. Sugrib Shaha for his appreciated help with SEM pictures. Likewise, I would like to thank my other colleagues, Dwayne Toscano, Amir Pahlevanpour for their support and guidance.

Finally, I owe my deepest gratitude to my beloved wife, Fereshtehsadat for her understanding, support, encouragement, which made this research possible. I also would like to thanks my parents for their love, motivations, support.

Dedicated to my parents

and to my wife

Table of Contents

List of figures

List of tables

List of Nomenclature:

a: Crack length

A: Cazacu-Barlat Constant

c: Cazacu-Barlat Constant

c: Paris law equation constant

$\{c\}$: Elemental compliance matrix

$\{C\}$: Global compliance matrix

CE: Cold expansion

CT: Compression-tension test

DCE: Double cold expanded

DIC: Digital image correlation

D_{hole}: Initial dimeter of the hole

$D_{Mandrel}$: Maximum diameter of the mandrel

E_{eff}: Effective Young's modulus

H: hardening rule coefficient

HCP: hexagonal close-packed

J_n: Nth Invariant of deviatoric stress tensor {k}: Elemental stiffness matrix

{K}: Global stiffness matrix

m_c: Coefficient of compressive stress

m_t: Coefficient of tensile stress

m: Paris law equation constant

n_j: Unit vector

N: number of cycles

ODDE: Opposite direction double expansion

{p}: Elemental pressure matrix

{P}: Global pressure matrix

r: Radius

r_2: External radius

S_{ij}: Components of deviatoric stress tensor

SCE: Single cold expanded

SDDE: Same direction double expansion

SEM: Scanning electron microscope

t_i^*: prescribed traction

$t_{split\ sleeve}$: Thickness of the split sleeve

TC: Tension-compression test

{U}: Global radial displacement

{u}: Elemental radial displacement

UCE: Un-cold expanded

VMP: Variable material property

XRD: X-ray diffraction

v_{eff}: Effective Poisson's ratio

ν: Poisson's ratio

ε_{eq}^{p}: Equivalent plastic strain

ε_{ij}: Total strain

ε_{ij}^{e}: Elastic strain

ε_{ij}^{p}: Plastic strain

$\varepsilon_{engineering}$: Engineering strain

ε_{true}: True strain

$\varepsilon_{plastic\ true}$: True plastic strain

σ_R: Radial stress

σ_{eq}: Equivalent stress

σ_{ij}: Component of stress tensor

$\sigma_{unloading}^{y}$: Reverse yield strength

σ_y: Yield strength

σ_{yc}: Compressive yield strength

σ_{yt}: Tensile yield strength

σ_θ: Tangential stress

σ_{true}: True stress

$\sigma_{engineering}$: Engineering stress

Γ: Surface

Ω: Volume

β: Bauschinger factor

ϕ: Hencky’s Scalar value

$\frac{da}{dN}$: Crack propagation rate

Δk: Stress intensity factor

Chapter 1. Introduction

1.1 Motivation

Greenhouse gas emissions are of concern to human beings as they cause global warming and climate change [1]. While 25% of global CO_2 emissions is attributed to transportation [2], road transportation and aviation are responsible for 74 % and 12 % of total transportation emissions [3]. As a result, finding a way to reduce these emissions is one of the fastest growing research areas. Using lightweight materials is being considered as one of the approaches to reach this goal. Initially, aluminum, being ~65% lighter than steel (Figure 1) was proposed as a replacement for steel in both automotive [4] and aerospace [5] industries. In recent years, advancement in material engineering and higher demand for reduction of global CO_2 emissions, have attracted the researcher's attention to other materials such as magnesium, which is the lightest structural metal [6] for both automotive and aerospace applications [7]. Additionally, wrought magnesium alloys have some superiority in terms of mechanical properties compared to cast magnesium, and are therefore preferable.

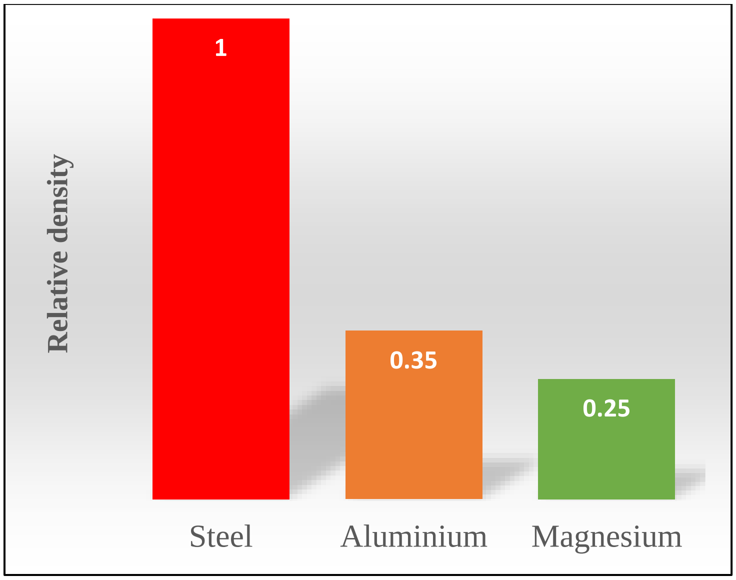

Figure 1. Relative density of magnesium, aluminium with respect to steel

Application of magnesium in the aerospace industry goes back to 1930, mostly in non-structural components such as gearbox casings [8], but these days magnesium is under study as a candidate material for load bearing components [9]. In this regard, investigating the different processes of assembly of magnesium components is very important. In aerospace, three different methods of connections are used: fastened joints (such as bolts and rivets), adhesive bonded joints, and welds; due to the high safety requirements, rivet joints are dominant in aerospace structures [10]. Rivet joints however, cause localized stress concentration in structures, making them highly susceptible to fatigue failure [11], Since fatigue failure in aircrafts can be catastrophic, fatigue analysis of rivet joints is of crucial importance. Moreover, finding ways to increase the fatigue strength of riveted structures has always attracted engineer's attention. As a result of the efforts made in this field, it was shown that compressive residual stress can significantly increase the fatigue life of riveted structures [12]. Among several methods of creating compressive residual stresses, such as shot peening [13] and laser peening [14], etc. cold expansion has been widely used in the aerospace industry [15]. The cold expansion process involves pulling an oversized mandrel or ball through the rivet hole [16], and is widely used in aerospace industry. The reason that this procedure is now well accepted by the aerospace industry is the fact that it adds no weight to the structure, it is relatively simple and low cost, and it produces a through thickness residual stress [17] and can significantly improve the fatigue life [18].

The aforementioned residual stress created by cold expansion, needs to be determined for predicting the fatigue life of components and structures. The cold expansion process is normally simulated in two steps: loading and unloading reversals. For this purpose, commercial finite element (FE) packages or available analytical solutions have to be used. The challenge in stress-strain analyses of Mg structures is the complex elastoplastic behavior, which is highly evident in wrought Mg alloys. Wrought magnesium alloys show anisotropy, i.e., the material behavior varies in different orientations [19],[20]. In addition, wrought Mg alloys exhibit asymmetric hardening behavior, i.e., the hardening curve under tension is different than that under compression [21]. Nevertheless, for many magnesium alloys such as rolled AZ31B, anisotropy is not as significant as asymmetry [22], [23]. The asymmetric hardening behavior make it impossible to model magnesium behavior in commercial FE packages such as ABAQUS and ANSYS, because they assume symmetric behavior [24]. All available models for the cold expansion process, either FE or analytical e.g. [25]–[30] adopt a hardening curve for the loading reversal and construct the hardening curve for the unloading reversal from that in the loading reversal using isotropic or kinematic hardening rules. Incompetency of typical material models for considering the complicated behavior of magnesium has led to advanced constitutive models based on continuum mechanics[31]–[33] or crystal plasticity [34][35]. Due to the inherent intricacy of using these models as well as the extensive time required for running these models, they are rarely used in real world problems. To tackle this issue, a simple numerical method called variable material property (VMP) [36], which is capable of capturing actual material behavior is used to model the cold expansion process in AZ31B-H24 magnesium alloy. Also, due to a considerable gap in literature about cold expansion of magnesium, from both modeling and experimental point of view, the feasibility of performing cold expansion also needs to be determined since AZ31B shows limited formability in room temperature [37], which is in contrast with the concept of cold expansion.

Along with this, effect of cold expansion on fatigue life of components made of AZ31B magnesium alloy is investigated.

1.2 Thesis objective

Experimental study of cold expansion process in AZ31B-H24 rolled sheet is performed. Simple numerical modeling and FE simulation is done to predict the radial displacement around the hole during the process and the residual stress when the procedure is done. The objectives of this research are as follows:

- To experimentally study the cold expansion of a wrought Mg alloy

For the first time, the feasibility of performing cold expansion in a wrought magnesium alloy is studied. An appropriate fixture for doing the test compatible with experimental measurements during test has been designed. Radial displacement during loading has been captured via DIC. The residual stress induced by the process has been measured by XRD.

- To adopt a simple numerical method, variable material property (VMP) and modifying it to account for asymmetric behavior to model both loading and unloading phases of the cold expansion process.

A proper approach for considering asymmetric behavior of wrought magnesium alloys is an essential component for modeling the cold expansion process. Therefore, the VMP numerical method has been modified to consider this behavior with an appropriate yield function.

- To model the process using finite element (ABAQUS) for sake of comparison with VMP.

For sake of comparison of VMP results, ABAQUS finite element software is used to model the process with more detail (3D, as opposed to 2D VMP), but simpler material model (symmetric). In addition, a parametric study of the effect of boundary condition in the model on residual stress distribution is performed.

- To characterize uniaxial tension-compression and compression-tension behavior of the AZ31B in high strain levels for incorporation in VMP code.

Uniaxial tension-compression and compression-tension behavior of AZ31B magnesium alloy is studied. There is a gap in literature for this behavior at high strain levels, which is needed for incorporation in VMP method.

- To study the effect of cold expansion on microstructure, texture, residual stress, and fatigue life

The created residual stress due to cold expansion affects the fatigue behavior of the specimen. This phenomenon is investigated for the first time by doing fully reversed push-pull load control fatigue test on cold expanded samples. Further, the effect of cold expansion on other aspect of material properties such as texture and microstructure is studied

1.3 Thesis layout

This thesis consists of five chapters. Chapter one declares the motivations of this research as well as the objectives of the study. In chapter two, a comprehensive background and literature review is presented, starting with a brief review of magnesium and its alloys, especially AZ31B. Then, the cold expansion process is introduced and the experimental and analytical models to date are presented. Eventually, the VMP method and its applications are reviewed. Chapter 3 deals with the experimental works performed in this research. First, the experiments pertaining to material characterization are presented, and then the structure specifically designed for the cold expansion is introduced. Then, sample preparation and DIC measurements is briefly described. Subsequently, the X-ray diffraction (XRD) method and results, hole drilling and digital image correlation (DIC) measurements are described. Feasibility of different cold expansion percentages and its effect on residual stress and fatigue life is discussed. Finally, the microstructure and texture evolution due to the cold expansion is studied and reported. Chapter 4 covers the VMP concept, the mathematical modeling, the convergence criteria, and the methodology for considering the hardening asymmetry in the VMP solution. In addition, in the FE simulation, a case study about the effect of different assumptions, such as friction between parts, and different boundary conditions is done. Eventually, chapter 5 summarizes the conclusions and some recommendations for future works.

Chapter 2. Literature review and background

This chapter presents background information and literature regarding magnesium and cold expansion. It is divided to three main sections. The first part is a review of magnesium and its alloys, specifically wrought AZ31B as the material of interest in this research. Then details of the cold expansion process are reviewed including the underlying concept, the process effect on the fatigue life of notched components, and finally, the analytical and FE models currently available. Finally, VMP method, its mathematical concept and its applications are reviewed.

2.1 Magnesium and its alloys

This section presents a review of literature regarding magnesium.

2.1.1 Applications and basic mechanical specifications

Magnesium (Mg) as the lightest structural metal, with density of 1.74 $\frac{g}{cm^3}$ compared with 2.7$\frac{g}{cm^3}$ for Aluminum and 7.86 $\frac{g}{cm^3}$ for steel [38], has attracted considerable attention from researchers in recent years [39] for use in the aerospace and automotive industry. Indeed, the application of magnesium in aerospace technologies goes back to World War I and II [40]. Figure 2 ([8]) shows some examples of magnesium usage in the early aerospace industry. In automotive industry, early use of magnesium alloys goes back to 1924 when magnesium was mostly used in the as-cast form and for non-structural purposes [41].

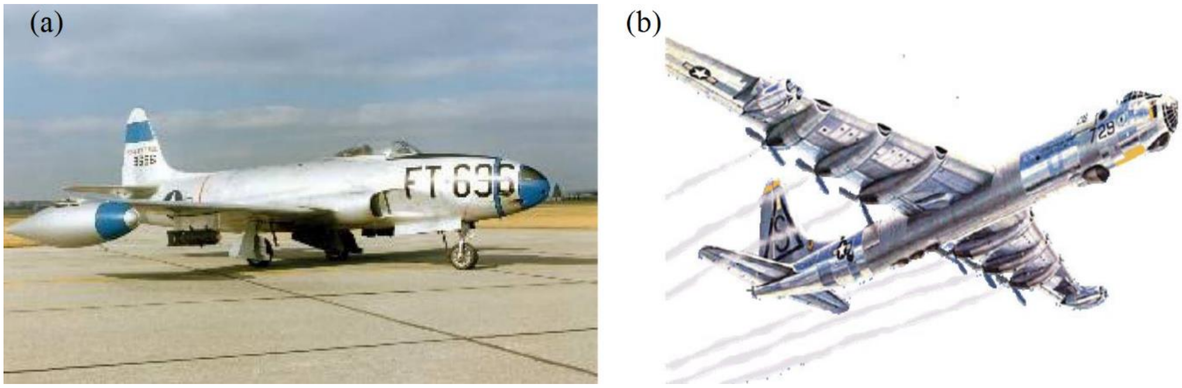

Figure 2. Example of application of magnesium in aerospace, a) Lockheed F-80C-made completely by Mg b) Convair B36 with a total of 8600 kg of Mg [8]

As mentioned in Chapter 1, in the 1930s, most magnesium use was for non-structural components [8]. Growing trend in air transportation [42] and the resulting increase in aviation CO_2 emissions, has once again attracted attention to magnesium as a candidate for replacing current materials in transportation industry. In fact, light weighting the components used in air transportation is now inevitable [43].

Besides the possible weight reduction, magnesium offers some other advantageous properties, such as good stiffness to weight ratio, good castability and good machinability [40], [44]. Plus, magnesium is the sixth most abundant element on the earth's surface [45].

Manufacturing processes for magnesium can be categorized into two general types: cast and wrought. Wrought magnesium alloys are manufactured via rolling, extrusion or forging [46]. Although wrought magnesium alloys are superior to their cast-built competitors, most magnesium used in industry are manufactured via die-casting [47], since it is cost effective and allow the building of components with complex geometries [7]. However, the wrought alloys have higher strength [48], more ductility [41] and greater homogeneity in mechanical properties.

Despite its helpful properties, magnesium and its alloys do suffer from some other undesirable features such as limited corrosion resistance, low strength at high temperatures [41] and poor formability at room and < 200°C temperatures [49], mainly due to its hexagonal close pack (HCP) structure [22]. This particular crystal structure, explains the low formability of magnesium and certain other special characteristics of magnesium alloys, which are described later in this chapter. According to Taylor's criteria [50] for arbitrary homogenous deformation, a polycrystalline structure needs five independent slip mechanisms. Because of its HCP crystal structure, [46], [51] Magnesium and its alloys, possess only two independent basal slip systems. Further investigation of magnesium's behavior revealed that there are other deformation mechanisms such as prismatic slip [52] and pyramidal slip [53]. Although all these slip mechanisms are enough to satisfy Taylor's criteria, it was shown that prismatic and pyramidal slips are very difficult to activate at room temperature [54], but are more easily activated at temperature higher than 225 ℃ [55], [56], due to a reduction in the critical resolved shear stress (CRSS) value. This fact explains the higher ductility of magnesium at elevated temperature [57].

However, another deformation mechanism is still needed at lower temperatures and studies have recognized another mechanism called “Twinning” in HCP metals [58][55].

Three twinning modes have been reported, pyramidal twinning on the $(10\bar{1}2)$ plane, also known as tension twinning, and contraction twinning on $(10\bar{1}1)$ plane and a combination of these two known as double twinning are reported in magnesium HCP structures [59]. Figure 3 shows the aforementioned slip systems and tension and compression twin in a single HCP crystal [34].

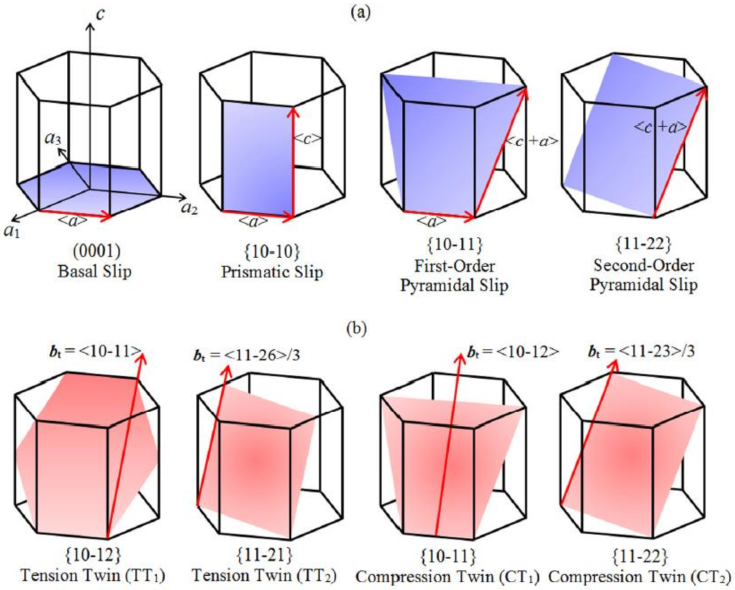

Figure 3. Schematic presentation of different deformation mechanisms, a) slips b) twin [60]

It should be noted that contrary to the slip mechanism, which allows simple shear in both forward and backward directions, twinning undergoes deformations only in one direction [35]. The amount of strain that can be accommodated by twinning is very limited. For example the maximum amount of strain for pure tension twinning is only 0.065 [61]. Further study about the effect of the twinning on ductility of HCP metals disclosed that the amount of twinning strain is proportional to the quantity of twinned grains; therefore, profuse twinning can result in higher ductility, e.g. titanium [62]. Tension twinning is activated when there is an extension along the c-axis of the HCP crystal, or compression parallel to the basal plane, which from the deformation point of view, is similar to extension along the c-axis [63][64]. Contraction twinning is activated when the c-axis of the HCP crystal is undergoing external compression [65]. Compression twin can accommodate only a very limited amount of strain, since compression along the c-axis is the least ductile deformation mechanism [66]. CRSS for tension twinning, is twice the value of a basal slip, making it the dominant deformation mode after basal slips, since the CRSS for other slip mechanisms, prismatic and pyramidal, is two orders of magnitude higher [22]. It should be noted that the value of CRSS for non-basal slip decreases significantly with an increase in temperature [67]. Consequently, at higher temperatures, these mechanisms are more likely to activate, which explains the improved formability of magnesium alloys reported at higher temperatures [68][69][70][71][72][73]. The other noteworthy aspect of tension twinning deformation is re-orientation of the HCP crystal in such a way that the c-axis of the crystal is approximately parallel to the undeformed basal plane, as depicted in Figure 4 [74].

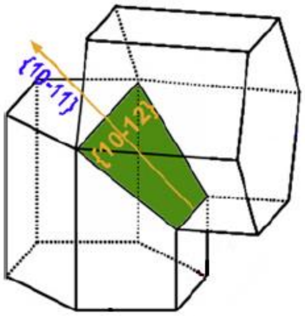

Figure 4. Schematic view of the reorientation of tension-twinned single crystal [74]

As mentioned, twinning is a one-way (polar) mode of deformation, which means it allows the strain to happen only at one direction not backward-forward as in slip mechanisms. Indeed, one of the other particular characteristics of magnesium alloys, known as asymmetric behavior, which is reported in many different magnesium alloys [75]–[78], is attributed to the contribution of the twinning in the deformation. Asymmetric yield and hardening is described as showing a different yield and hardening strength under compression and tension. This asymmetric behavior is not to be associated with strength differential effects [79] caused by hydrostatic strength in high strength steels. Considering a single HCP crystal can help understand the concept. When a single crystal is deformed, different deformation mechanisms are activated, depending on whether tension or compression occurs along its c-axis. When the applied external stimulant is less than the material yield strength, i.e., in the elastic regime, the deformation mechanism is stretching the atomic bonds, which is a reversible process [80]. As soon as the external stimulus exceeds the elastic strength of the material, plastic deformation occurs. During c-axis extension, basal slip and tensile twins are the dominant deformation mechanism, whereas during compression of the c-axis, basal slip and prismatic slips are governing the deformation Since the CRSS value for a prismatic slip is much higher than that for tensile twinning, c-axis compression results in a higher yield stress, as displayed in Figure 5 [63].

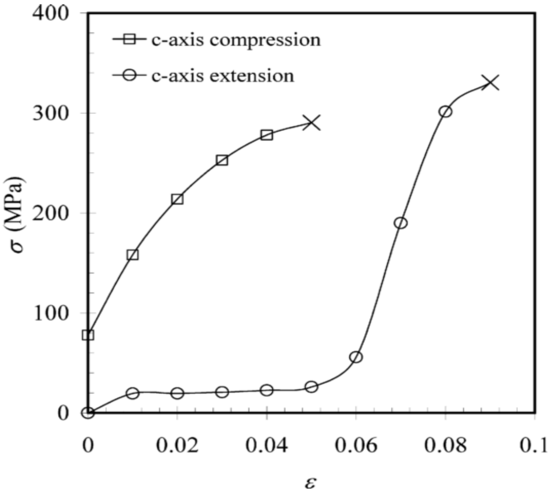

Figure 5. Single HCP crystal response to deformation along c-axis [63]

The above-explained phenomenon was for a single crystal, but can easily be extended to poly-crystal structures. Because wrought magnesium alloys are manufactured via rolling, extrusion or forging [46], the result is a highly textured material [35]. In rolled magnesium alloys, a rolling process at high temperature organizes the crystals in such a way that their c-axis are perpendicular to the surface of the sheet [81]. In other words, in-plane compression causes c-axis extension, which activates the tension twinning. Nevertheless, in the real world, HCP crystals in wrought magnesium alloys are not perfectly aligned, meaning some grains have a randomly oriented c-axis. Accordingly, in plane tension can also activate twinning in some grains [22].

Wrought magnesium alloys such as AZ31B rolled sheet and extrusion also show anisotropy, which is defined as the dependency of a material's behavior on the loading direction [23][82][83]. This feature is due to the difference in intensity between the basal texture in the transverse direction (TD) and the rolling direction (RD) [84][85]. In AZ31B-H24, it was shown that the material in TD shows a little stronger behavior when it is compared to RD. however, it was shown that while asymmetric behavior is significant in wrought AZ31B, the in-plane anisotropy is minimal [23][86].

2.1.2 Rolled AZ31B-H24- monotonic-fatigue properties

Among the available commercial magnesium alloys, AZ31 is the most used in industry [87] with vast applications in automotive and aerospace industries [88]. The chemical composition of this alloy is given in Table 1 [89].

Table 1. Chemical composition of AZ31B-H24 [89]

Composition	Al	Zn	Mn	Mg
Weight %	2.73	0.915	0.375	Bal.

Numerous studies have looked at AZ31B monotonic tension, compression and tension-compression (TC) and compression-tension (CT) behavior [90]–[95]. Tension-compression and compression tension results are all in the low or middle range regarding the value of strain (below 10%), since there is a buckling problem in compression tests of sheet materials [96].

The fatigue behavior of AZ31B has been investigated comprehensively in recent years [97]–[107] . Comparing the fatigue life of rolled AZ31B in strain control tests with fatigue life of 7050 aluminum alloy, shows that magnesium alloy is slightly better than aluminum alloys [112], which authenticates the motivation of this research, since 7-series aluminum alloys are widely used in aircraft [113]. Surprisingly unlike the fatigue behavior of smooth magnesium samples studies, that of notched specimens made of AZ31B [108], [111] has been limited. In particular, there are limited studies on crack initiation around a magnesium sheet with circular notch.

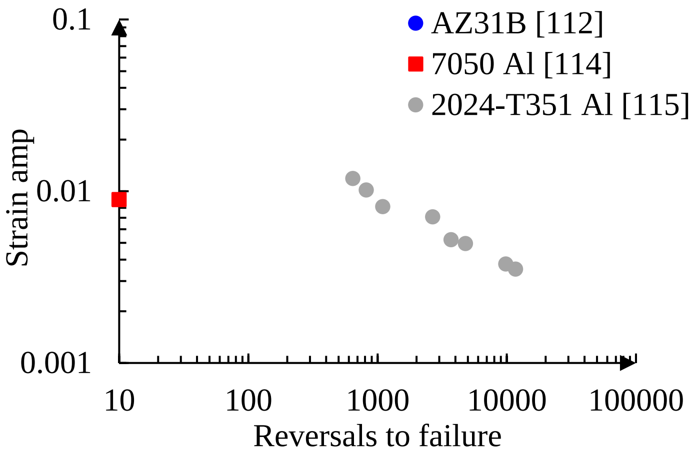

Figure 6. Strain-life curve, AZ31b vs 7050 Al [112] [114][115]

2.2 Split sleeve cold expansion

2.2.1 Background and concept of split sleeve cold expansion

Aircraft frames are multi-part structures, with rivet joints being the most common assembly technique in the aerospace industry [116]. However, they are also a critical point of the structure, since the geometry of rivet joints results in high stress concentration [117], and may lead to fatigue failure. One the most practical ways to enhance the fatigue behavior of these components is to create compressive residual stress, which can significantly improve fatigue life [118]. Many different methods have been utilized during past decades in the aerospace industry to increase fatigue life of components by creating compressive residual stress, such as shot peening and cold working methods like roller burnishing and ring coining [119]. Due to their limitation and cost, these have been replaced by other cold working methods such as hole edge expansion, direct mandrel expansion, ball expansion and split sleeve cold expansion [10]. Schematic drawings of the first three methods are shown in Figure 7.

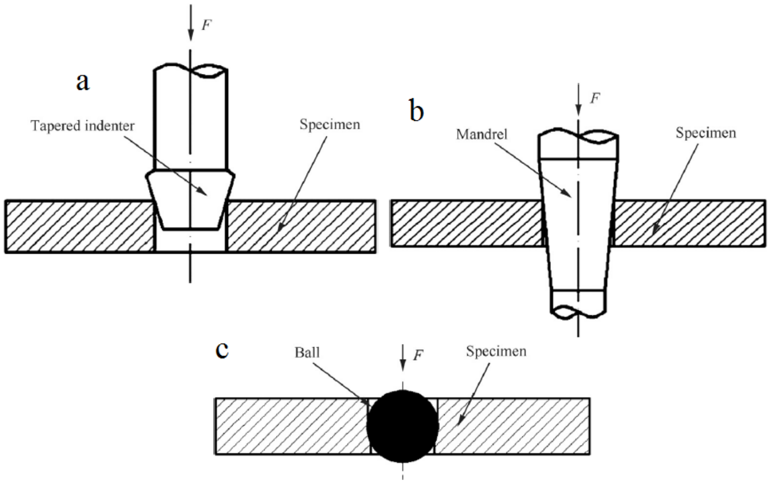

Figure 7. Cold expansion methods, a) hole edge expansion, b) tapered mandrel, c) ball expansion [10]

In hole edge expansion, only the edge of a hole is expanded, which results in a zone free of residual stress in the middle of the thickness and a non-uniform hole diameter. In mandrel and ball expansion processes, due to applied driving force and direct contact between the mandrel or ball, and work-piece, the surface of the specimen is damaged, thus the fatigue life improvement by these methods is very limited [10].

Split sleeve cold expansion was developed during the 1970s by the Boeing Company [119]. This process consists of imposing plastic deformation on the work-piece by radially expanding the hole. To do so, a tapered mandrel fitted with a split sleeve is pulled through the hole, as shown in Figure 8 [120].

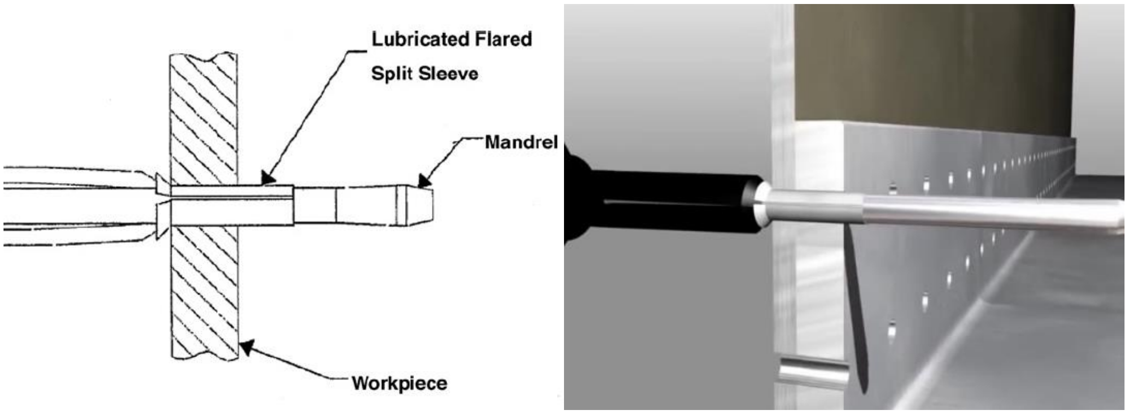

Figure 8. Schematic view of split sleeve cold expansion process [120]

Indeed, the major diameter of the mandrel is less than the diameter of the hole, but the total diameter of the mandrel and split sleeve together is greater than that of the hole, which means that pulling the mandrel through the hole while the mandrel is surrounded by the split sleeve, expands the hole radially. After removal of the mandrel, the elastically deformed zone around the hole springs back [121], which results in a compressive tangential residual stress field around the notch, which is now plastically deformed [122].

Degree of cold expansion is defined as [123] :

$$\text{CE } \% = \frac{(D_{Mandrel} + 2t_{split\ sleeve}) - D_{hole}}{D_{hole}} \times 100 \tag{1}$$

in which $D_{Mandrel}, 2t_{split\ sleeve}, D_{hole}$ are mandrel maximum diameter, split sleeve thickness and initial dimeter of the hole, respectively.

According to equation (1), the cold expansion percentage is a measure of the maximum change in diameter that the hole experiences during the loading process. After the process, because of spring back, the final diameter is less than the maximum diameter during expansion, so sometimes the cold worked piece is reamed after the process to bring the hole to the required final size [124].

2.2.2 Modeling the cold expansion process

As mentioned, cold working the fastener holes creates compressive tangential residual stress, which can result in fatigue life improvement. To predict the fatigue life of a component after cold expansion using available fatigue models, one should know the residual stress distribution. Therefore, a model than can simulate the residual stress is necessary. Accordingly, various studies have modeled the residual stress around cold worked holes, and are briefly reviewed here. Their approaches can be divided into two general categories: analytical/numerical models and finite element models.

2.2.2.1 Analytical/Numerical models

In the split sleeve cold expansion process, the split that allows the sleeve to deform more easily, results in non-uniform deformation around the split. Amjad et al. [125] has shown that this effect is localized and elsewhere around the notch, the deformation is axisymmetric. Thus in all numerical models the process is considered to be axisymmetric. The following researchers all contributed to the understanding, but as they only consider idealized material models, residual stress predictions are only approximate.

In 1943, Nadai [25] modeled the contact problem arising when a pressurized tube is inserted into a surrounding steel plate, which was a common manufacturing procedure used to prevent leakage in the tube fittings. The model of the steel plate is the one of interest here. For modeling, he assumed an infinite plate with a hole subjected to uniform pressure with plane stress condition. Von-Mises yield criteria and a perfectly plastic stress-strain curve for the material were used. After removal of the pressure, elastic behavior was adopted in the model. With a similar approach, Chang, in 1975 [26], used the solution of a thick walled cylinder devised by Sach [126] in which uniform pressure, perfectly plastic material behavior, Von-Mises yield criteria and plane strain condition, as well as elastic unloading were assumed. Then the predicted residual stress field by this method was used to analyze fatigue crack growth.

In the aforementioned solutions, the material model used to simulate the loading during mandrel insertion is perfectly plastic, however, in more-recent studies, more complex material models were used.

.

Hsu and Forman [127] proposed an analytical solution based on total deformation theory to obtain residual stress in an infinite sheet with hole subjected to internal pressure by assuming power law elastic-plastic hardening behavior and elastic unloading with plane stress condition.

In the studies reviewed to this point, the solution for the unloading was assumed to follow the elastic unloading curve, which consistently over predict the residual stress, since the elastic solution always results in higher values of stress. As first try to make the unloading solution more reasonable , in 1977, Rich and Impellizzeri [27] developed a solution for cold expansion considering reverse yielding by adopting isotropic hardening as the behavior of the material during unloading. The elastic deformation of the mandrel was also taken care of by assuming radial interference equal to the sum of the radial deformation of the mandrel with elastic behavior plus the radial displacement of the plate. Perfectly plastic material behavior was adopted for solving the loading part. Further, the residual stress was employed to study the crack initiation and growth after cold expansion.

In 1988,Wang [29] presented a closed-form solution for a cold expanded hole using J_2theory of deformation by assuming both plane strain and plane stress conditions. A modified version of the Ramberg-Osgood stress-strain curve was chosen. Elastic behavior of the mandrel was also accounted for in this model. Since it was shown that considering reverse yield significantly changes the residual stress distribution, a more complex unloading curve was proposed which considers the Bauschinger effect [128] using the formula:

$$\sigma_{unloading}^{y} = 2(1+\beta)\sigma_y - \sigma_{max} \tag{2}$$

in which, $\sigma_{unloading}^{y}$,β, σ_y,σ_{max} are, respectively, reverse yield strength, Bauschinger factor, yield strength and maximum stress that an element undergoes during loading.

By assuming different values for β,it was shown that tangential residual stress is strictly a function of reverse yield, while in contrast, peak tensile residual tangential stress is independent.

In 1991, Clark [129] inspected the residual stress field due to cold expansion, based on a model of his own [130], which was developed for modeling a pressurized thick-walled cylinder. Assumptions of modified Tresca Yield criteria, plane stress and perfectly plastic material behavior were made. To address the effect of reverse yielding on residual stress, the Bauschinger effect was considered in such a way that reverse yield stress was assumed to be a constant factor of the loading yield (1.4 was assumed for the study).

In 1993, Wanlin [131] extended the work by Hsu and Forman to take into account the effect of finite plate width and the Bauschinger effect.

Bauschinger effect was taken care of by:

$$\sigma^{y}_{unloading} = 2(1 - H)\sigma_y + 2\sigma_{max} \tag{3}$$

Where $0 \leq H \leq 1$, however the discussion regarding unloading analysis is only cursory and details are not provided.

As one of the comprehensive models of cold expansion, Ball in 1995 [30], expanded Hsu's solution by considering Bauschinger effect in a way similar to equation (2). Different hardening behavior for the solution of the unloading part using various Bauschinger coefficients as well as a Ramberg-Osgood relation for stress-strain behavior of the material was implemented in the model. A parametric study of the effect of different Bauschinger factor again highlighted the importance of considering reverse yielding. The elastic deformation of the mandrel was also included in the model. Along with this, this predicted residual stress was utilized for evaluating fatigue crack growth.

It should be mentioned that all of these models are using idealized material behavior for both loading and unloading part.

2.2.2.2 Finite element models

The arrival of computers and subsequent development of numerous finite element software products helped researchers to simulate problems in more detail. As mentioned, modeling the residual stress after cold expansion has always been very interesting for researchers. Consequently, finite element models have been proposed for modeling the cold expansion process. As one of the early attempts, a 2D model with a hole subjected to uniform pressure was proposed to simulate the cold expansion process [132]. To make the model closer to reality, two dimensional (2D) finite element models were proposed, in which a 2D plate with a circular hole was subjected to uniform displacement at the edge of the notch [133]. In this study, plane stress and plane strain conditions, as well as isotropic and kinematic hardening for the unloading part, were assumed. Similar to the solutions by analytical models, it was shown that residual tangential hoop stress heavily depends on the reverse yielding criteria [133]. To examine the effect of reverse yielding on residual stress after cold expansion, a comparison between combined hardening, purely kinematic hardening and purely isotropic hardening with experimental results, nicely emphasized the fact that if reverse yield occurs during unloading, a more precise material model (in better agreement with the experiment) can predict residual stress field more accurately [134]. As shown in Figure 9, even though the results from combined hardening are closer to the experimental measurements, still there is a significant difference, which can be attributed to the approximation of reverse yielding prediction by the combined method (Figure 9a, [134]) .

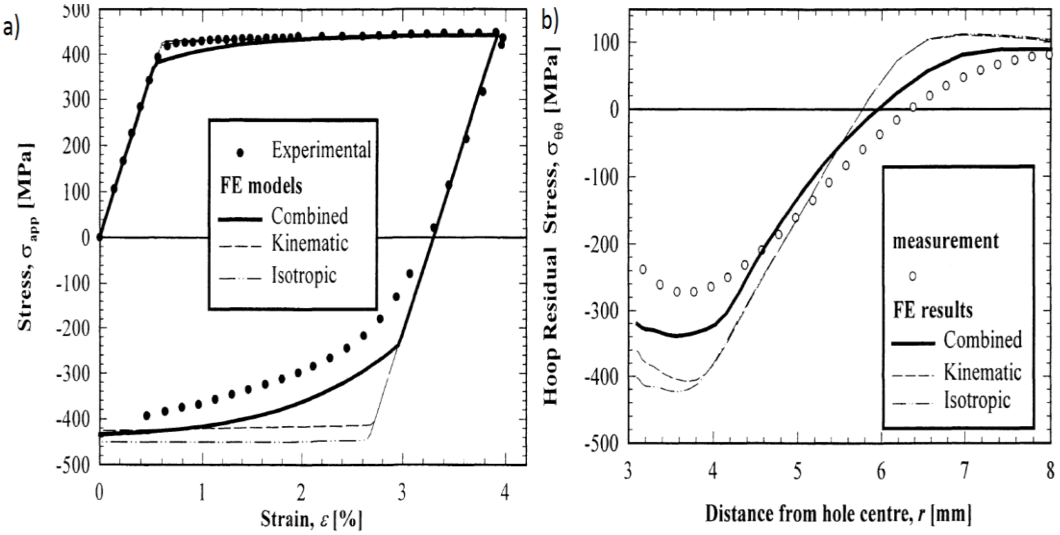

Figure 9. a) Loading-unloading behavior of Al2650, b) residual hoop stress after 4 % cold expansion [134]

More-advanced FE software made it possible for researchers to consider additional features and details, leading to a more-realistic model. In some 3D FE simulations, assuming that the effect of mandrel movement is minimized by the split sleeve, a hole was subjected to uniform displacement [124]. With similar reasoning, some researchers, such as Babu et al. [135], modeled the insertion of a mandrel by making different layers through the thickness of the work piece and applying the designated displacement at each layer at different steps, an approach that was assumed to simulate mandrel's movement through the thickness.

Adding the mandrel to the FE models revealed that there is a gradient of residual stress distribution through the thickness of the work piece [136], [137]. This non-uniform distribution of residual stress can be explained by the different boundary conditions affecting the various layers of material during the mandrel insertion. As depicted in Figure 10, when the mandrel is moved a little toward the exit face, the upper layer is already unloaded, and because of the spring back, the diameter is something between the original hole diameter and the diameter during loading. There is another layer, which is experiencing the loading scenario while the lower layers are still in a virgin condition. On the other hand, because the applied force on the mandrel is transferred to the work piece by friction, there will be some stress in the direction of the mandrel movement in the middle of the work piece, while at the entry and exit surface it has to be zero, since they are free surfaces. Therefore, these factors result in the variation of residual stress distribution through the thickness [138].

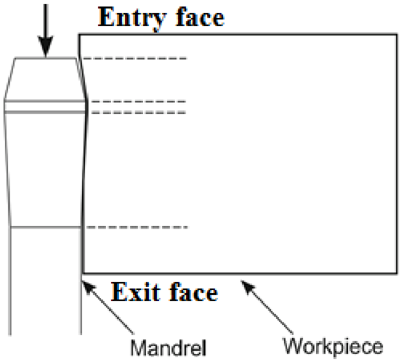

Figure 10. Different configuration of through thickness layers during mandrel insertion [138]

As a result of this gradient in the residual stress distribution, crack initiation in the cold expanded sample occurs close to the entry surface [124][139], where the mandrel first goes in, since the tangential residual stress is lower than that of the exit face [124].

Two-dimensional models are unable to capture this through thickness variation, since they assume uniform deformation through the thickness. However, by comparing the 2D and 3D models, it has been shown that the results of 2D models are very close to the results of 3D models in the mid-section [140].

Since the mandrel is usually made of high-strength steel [141], in many cases, the mandrel is modeled as a rigid body [142], [143]. Considering a deformable material for the mandrel in FE models showed that the effect of its deformation in residual stress distribution is negligible [138].

The presence of a split sleeve has also been taken into account. Comparing the results from the models with and without a split sleeve for same level of expansion revealed that split sleeve does have a significant effect on residual stress distribution. The most -affected component is the hoop stress at the entry face, whereas the effect on radial residual stress and hoop residual stress of the mid-thickness layer and exit face is minimal [142]. Further, examining the role of friction between the mandrel surface and inner surface of the split sleeve and the split sleeve and work piece determined that the effect of mandrel-split sleeve friction on residual stress is imperceptible and the assumption of no friction contact is reasonable since all split sleeves have pre-lubricated inner surface to reduce the above-mentioned friction. Only tangential residual stress at the entry face is slightly affected by friction between split sleeve and work piece [139][142][144].

From the standpoint of fatigue performance, the weakest point of the cold expanded component, which is the entry site due to its lower residual hoop stress, controls fatigue life. Experimental measurements also highlight that fatigue cracks initiate close to the entry side [136], since it has the lowest residual tangential stress. As a solution, double cold expansion was suggested. It was shown that re-cold expanding the hole can increase the residual stress at entry site and make a more uniform residual stress distribution through the thickness [145].

In terms of modeling, there are only a few finite element models of the double cold expansion process. For the sake of simplicity, only the tapered pin or ball methods of cold expansion are simulated in the finite element models. To the best of the author’s knowledge, there is no finite element model for double split sleeve cold expansion, even though as mentioned, the split sleeve does have considerable effect on residual stress distribution [142]. In FEM models, it was shown that residual stress at the entry face is increased by doubling the cold expansion in the opposite direction, i.e., the entry face of the second pass is the exit face of the first pass, but in same direction, it may even generate tensile residual tangential stress [146][147].

2.2.3 Experimental works on the effect of cold expansion on fatigue life

The main goal of cold expansion is to increase the fatigue life of components. So far, the models used to predict the residual stress field due to cold expansion that causes this improvement, have been reviewed. Next the literature on the cold expansion process from an experimental point of view is summarized.

2.2.3.1 Experimental investigation of the effect of cold expansion on fatigue life- crack initiation and propagation

Fatigue life consists of two stages, crack initiation and propagation. Compressive residual stress improves of the fatigue life by both retarding crack initiation and decreasing the growth rate of crack propagation [148]. For all engineering metals, including steel [149], aluminum [150]–[152], and titanium [153][123], it was shown that this improvement factor is a function of the loading spectrum. Stress R-ratio, which is defined as the ratio of minimum applied stress to the maximum stress, seems to play an important role in fatigue life improvement due to residual stress. It was shown that under the same stress amplitude, for lower R (negative value for R) the improvement of fatigue life is greater [154][122]. Correspondingly, for a fixed value of the R ratio, the fatigue life improvement factor is increased by decreasing the stress amplitude [143][155]. These findings can be explained by the fact that, in both cases, for lower fatigue life improvement, the peak tensile stress is greater, which causes residual stress relaxation [149]. In a thorough study [156], it was demonstrated that higher tensile load can reduce the residual stress especially near the notch, mainly by growth of small fatigue cracks. Regarding the effect of cold expansion on crack initiation life, only limited data are available in the literature, some claiming that crack initiation life improvement is greater than crack propagation improvement [157] [158], while others claim that improvement in crack improvement in crack propagation life is more pronounced [148].

As mentioned in section 2.2.2.2, double cold expansion has been beneficial for fatigue life. Its experimental comparison have shown that double cold expansion in opposite direction can increase the fatigue life significantly more that single cold expansion does. A typical experimental result is shown in Figure 11.

Experimental residual stress measurements showed that increase in fatigue life is mostly due to increase in residual tangential hoop stress at the entry site, while residual stress at the exit face is less affected [159].

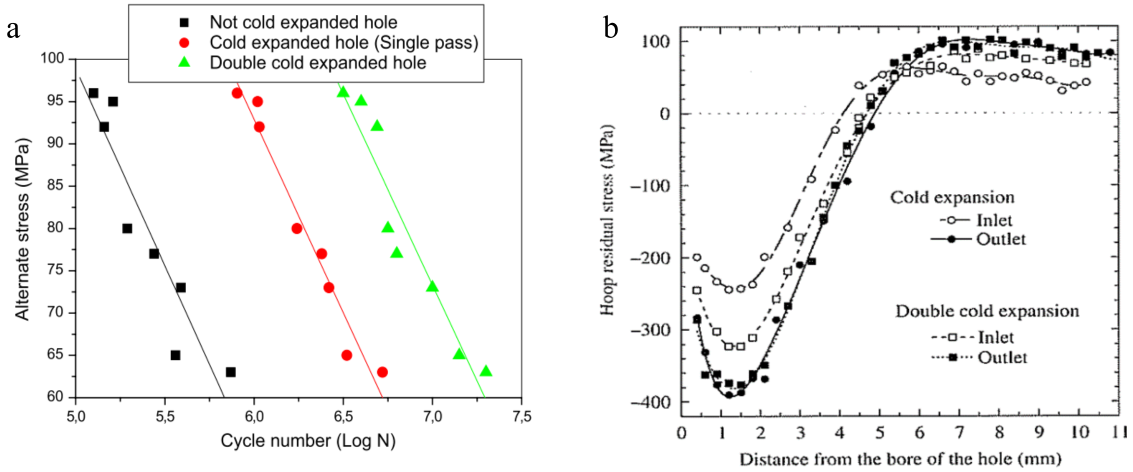

Figure 11. Typical effect of double cold expansion, a) fatigue life [158] , b) residual stress distribution [159]

2.2.3.2 Optimum degree of cold expansion

The degree of cold expansion, defined by equation (1), plays an important role in fatigue life improvement. In fact, the degree of cold expansion governs the residual stress distribution. Upon removal of the mandrel, unloading occurs in a cold-worked piece. The highest residual stress can be achieved by elastic unloading, but in reality, reverse yielding happens, especially for high levels of expansion [148], resulting in a lower residual stress at the edge of the notch. Therefore, a higher degree of expansion does not necessarily guarantee better fatigue life, since it may result in a lower residual tangential stress [160]. On the other hand, a higher degree of expansion results in a greater area of compressive residual stress. As can be seen in Figure 11 b, a typical hoop residual stress has a compressive zone close to the hole followed by a tensile zone; together the two satisfy the equilibrium equations. It was shown in [161] for the same value of residual hoop stress at notch, higher degree of cold expansion results in greater fatigue life, since a bigger area of compressive residual stress can both delay crack initiation and decrease the rate of crack growth, but mainly the latter. In contrast, more extensive zone for compressive residual stress results in higher tensile peak load (Figure 11 b), which can promote crack initiation at the hole edge [145]. Comparing the fatigue life enhancement gained by different degrees of cold expansion as in [136],[148],[151],[143] has revealed that increasing the degree of cold expansion up to a certain value increases the fatigue life improvement factor, but after that specific value, known as the optimum degree of cold expansion, fatigue life improvement decreases. The optimum degree of cold expansion was shown to be between 4-6 % depending on material properties [136][160][162][163]. With very high level of cold expansion, a paradoxical detrimental effect was reported, in that the fatigue life is less than that for and un-cold worked hole [162]. The reason for this phenomenon has not been explained. It seems that the cause was the damage induced to the specimen due to high levels of plastic strain during cold expansion. As a side note, it should be mentioned that maximum achievable degree of split cold expansion with standard tools is 6% [164].

2.3 Variable material properties

This section reviews the variable material property approach, as the main modeling approach of this study.

2.3.1 Variable material properties (VMP), mathematical concept, application

The idea of using an elastic solution as a basis for solving elastic-plastic material problem goes back to the 1950's. As an early example, Nadai [165] in the 1950s, used the elastic solution of a thick walled cylinder to generate the elastic-plastic solution. In 1997, Jahed and Dubey [36], [166] presented VMP as an axisymmetric method of elasto-plastic analysis, one based on the total deformation theory of plasticity and uses an elastic solution to generate the inelastic solution. After its initial presentation, the VMP approach has been used by many different researchers in solving many different practical elastic-plastic problems. A complete review of the model and its application in the past two decades is given by Faghih et al [167]. An overview of VMP approach is given first. Consider a body of volume Ω enclosed within surface Γ. In the absence of body forces, the equilibrium equations will be in the form of

$$\sigma_{ij,j} = 0|_{\Omega} \tag{4}$$

where σ_{ij} stands for the components of the stress tensor and the comma represents the partial differentiation. The boundary conditions over the surface Γ can be divided into two parts: prescribed traction (t_i^*) over surface Γ_1, which is shown by:

$$\sigma_{ij} n_j = t_i^*|_{\Gamma_1} \tag{5}$$

where n_j is the unit vector normal to the surface, and displacement (u_i^*) over surface Γ_2

$$u_i = u_i^*|_{\Gamma_2} \tag{6}$$

where

$$\Gamma_1 + \Gamma_2 = \Gamma \tag{7}$$

The total strain is assumed to be the sum of the elastic part plus the corresponding plastic part.

$$\varepsilon_{ij} = \varepsilon_{ij}^e + \varepsilon_{ij}^p \tag{8}$$

Elastic strain is given by Hook's law

$$\varepsilon_{ij}^e = \frac{1+\nu}{E}\sigma_{ij} - \frac{\nu}{E}\sigma_{kk}\delta_{ij} \tag{9}$$

where ν, E, δ_{ij} are the Poisson's ratio, Young's modulus and the Kronecker delta, respectively. According to Hencky's total deformation theory:

$$\varepsilon_{ij}^p = \phi S_{ij} \tag{10}$$

where S_{ij} is the deviatoric stress and ϕ is a scalar value.

$$S_{ij} = \sigma_{ij} - \frac{1}{3}\sigma_{kk}\delta_{ij} \tag{11}$$

$$\phi = \frac{3}{2}\frac{\varepsilon_{eq}^p}{\sigma_{eq}} \tag{12}$$

It is worth mentioning that while Hencky's total deformation plasticity results matches the incremental plasticity for proportional and near proportional loading problems Jahed et al. [168][169][170] have shown its extension to non-proportional loadings, extending its application to a wider range of problems.

The value of ϕ is obtained from a uniaxial stress-strain curve. Incorporating Equations (10),(11) and (12) into Equation (9) results in

$$\varepsilon_{ij} = \left(\frac{1+v}{E} + \phi\right)\sigma_{ij} - \left(\frac{v}{E} + \frac{\phi}{3}\right)\sigma_{kk}\delta_{ij} \tag{13}$$

which can be written in a similar form to elastic formulation

$$\varepsilon_{ij} = \frac{1+v_{eff}}{E_{eff}}\sigma_{ij} - \frac{v_{eff}}{E_{eff}}\sigma_{kk}\delta_{ij} \tag{14}$$

where v_{eff}, E_{eff} are the effective Poisson's ratio and effective Young's modulus, respectively. Comparing (14) with (13) defines these values as follows:

$$\begin{aligned} E_{eff} &= \frac{3E}{3+2E\phi} \\ v_{eff} &= \frac{3v+E\phi}{3+2E\phi} \end{aligned} \tag{15}$$

These effective values are field variables, and depend on the stress state at each point. For solving axisymmetric boundary value problems, one should know the spatial distribution of v_{eff}, E_{eff}, which depends on the stress distribution, so the solution is inherently an iterative procedure. The following procedure, which uses the aforementioned formulation, is proven to be capable of solving elastoplastic axisymmetric problems. First, by discretizing the body into small elements, a purely elastic solution is obtained. Elements with equivalent stress greater than the yield stress of the material are considered to be in the plastic region. For these elements, the value of E_{eff} is calculated using the projection method, which is based on the assumption that the total strain predicted by the elastic solution is always less than or equal to the real elastoplastic total strain. As an example, consider an infinite plate with a center hole subjected to tensile traction on the boundary, as shown in Figure 12. In the elastic solution, points closer to the hole such as “a”, have higher stress than other points such as “c”, due to stress concentration. If the equivalent stress for point a is less than the material’s yield strength, all points remain in the elastic regime and the elastic solution is applicable. If the equivalent stress of elements close to the notch exceeds the material’s yield limit, plastic deformation occurs and the elastic solution is no longer valid. For points with stress that exceeds the yield limit, the values of v_{eff}, E_{eff} need to be modified. To update v_{eff}, E_{eff} values of the small strip that contains point a , at the same level of strain, the corresponding stress must be obtained from the uniaxial stress-strain curve. Dividing this stress by the abovementioned, which technically is the secant modulus at point a', gives the new value of E_{eff}. By eliminating ϕ from Equation (15), v_{eff} is calculated using the new value for E_{eff}. It is assumed that at each strip with updated values of v_{eff}, E_{eff}, these parameters are constant over the strip, which in the case of small strips is a valid assumption. Therefore, the elements’ stiffness matrixes are updated using the effective parameters, and are assembled to generate the global stiffness matrix. Then, a new elastic solution can be obtained using the updated global stiffness matrix.

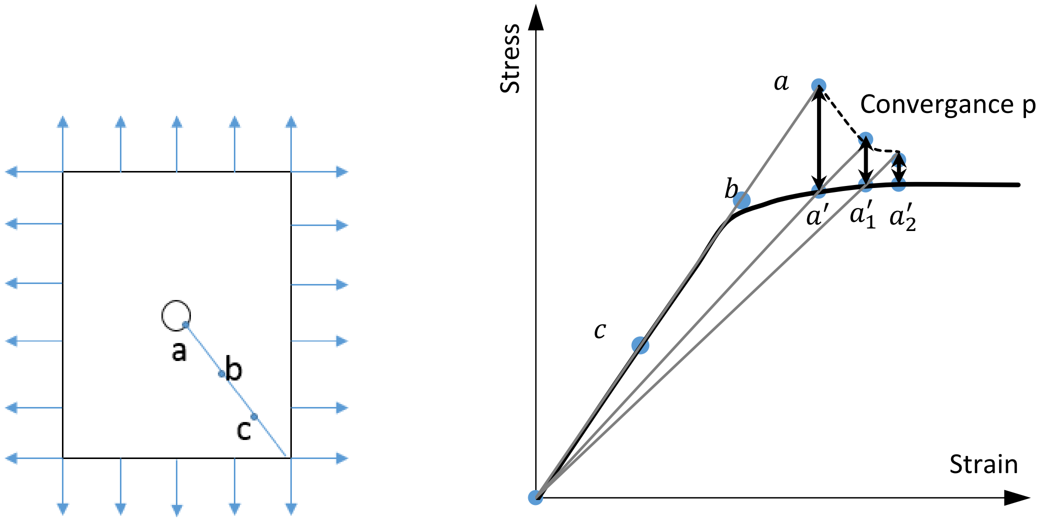

(a) **(b)**

Figure 12. Illustration of the VMP approach for an axisymmetric problem; (a) notched sample under biaxial loading, (b) projection method [36]

This process is repeated until the $\sigma_{eq} - \varepsilon \left(= \frac{\sigma_{eq}}{E_{eff}}\right)$ curve obtained from the calculation coincides with the experimentally obtained uniaxial stress-strain curve. The unloading procedure is similar to the loading one, except that now each strip has its own stress-strain curve, which is obtained by adopting a hardening rule such as the isotropic or kinematic hardening rule, or from the real unloading curve obtained from the experiment. After solving the unloading part, the residual stress field is obtained by:

$$\sigma_R = \sigma - \sigma_u \tag{16}$$

where $\sigma_R, \sigma, \sigma_u$ represent residual stress, stress at the end of loading, and stress at the end of unloading, respectively.

Due to its simplicity and capability of incorporating actual material behavior, VMP method is used widely in numerical analysis in different areas, such as for pressure vessels, including autofrettage [171]–[175], spherical vessels [176]–[179],compound tubes [180]–[182]. Additionally it is employed in simulations relating to rotating disks including thermomechanical stress analysis [183]–[185] and creep of disks [186], [187], as well as for functionally graded materials [188]–[190]. Recently, its use has been extended to finite element methods [191], [192] as a fast converging approach. A recent review of the model and its application in the past two decades is given by Faghih et al. [167].

2.3.2 Application of VMP in cold expansion

As mentioned in section 2.2.2.2, split sleeve cold expansion can be considered as an axisymmetric problem, since the effect of the split is localized. In 2000, Jahed et al. [193] successfully implemented the VMP method to predict elasto-plastic boundary and more importantly, residual stress field, both due to cold expansion. All numerical models mentioned in section 2.2.2.1 deal with approximation of loading-unloading behavior of the material, mostly Ramberg-Osgood and isotropic hardening, respectively. As shown in Figure 9. a) Loading-unloading behavior of Al2650, b) residual hoop stress after 4 % cold expansion [134], in most of the cases, the unloading behavior of materials cannot be characterized with conventional hardening rules. Jahed et al. [194] showed that actual material behavior significantly affects the residual stress distribution. Therefore, VMP, with its capability of considering actual material behavior in both loading and unloading steps, can be properly applied to cold expansion problems. To verify the capability of this method as a solution for such problems, it was shown that VMP can readily predict the elasto-plastic boundary, as depicted in Figure 13, while other aforementioned methods suffer from significant inaccuracy [194].

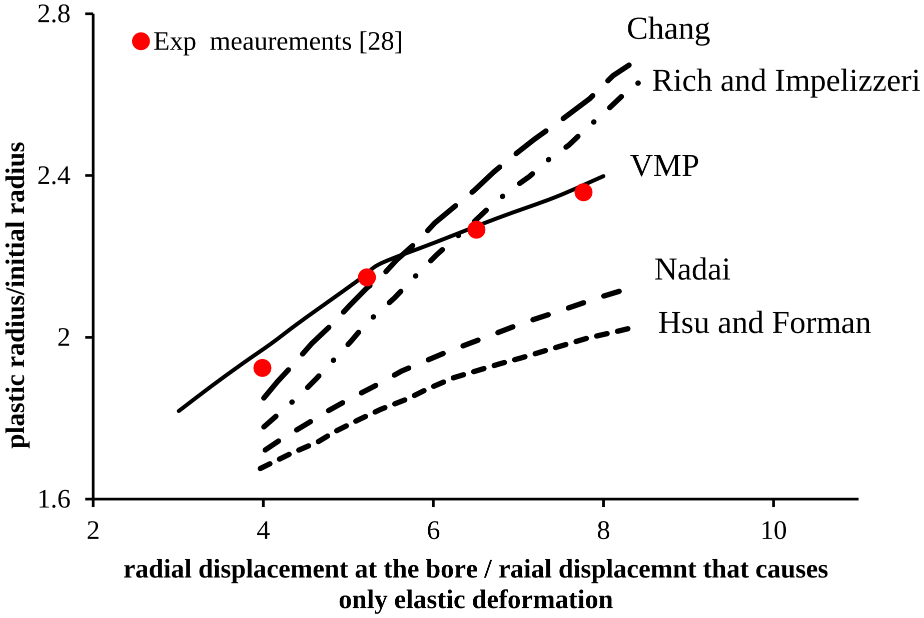

Figure 13. Elastoplastic boundary of a cold-worked hole; VMP vs. other analytical and experimental results

2.3.3 Application to asymmetric materials

The original VMP was proposed for isotropic-symmetric materials; however, because of its simplicity in relating the stress state of elements to the actual stress-strain curve of the material, VMP was also used for asymmetric materials.

2.2.3.1 Asymmetric rotating bending problems

In a rotary bending test, each element has a uniaxial stress state, meaning that below and above the neutral axis, the sign of stress is different. Thus, on the cross section some elements are in pure tension, others are in pure compression. As already stated, asymmetry is defined as difference in tension and compression behavior; therefore, in an asymmetric material under bending, the behaviors of different elements are not the same. VMP method was successfully implemented in rotary bending problems with specimens made of magnesium alloys [195], [196] [106]. In solution, for elements in tension and in compression, the experimentally obtained tensile curve and compression curve are used in the projection method, respectively. After updating values of v_{eff}, E_{eff}, the difference in material properties in the cross section was addressed by using the concept of composite beams.

2.2.3.2 Asymmetric pressurized cylinder

Recently, Khayamian et al. [24][197] proposed an extension of VMP for analyzing a thick-walled pressurized cylinder made of asymmetric material. In contrast to rotary bending, the stress state of all its elements is biaxial. To consider the effect of asymmetric behavior, a weighted average method was suggested. In this approach, the curve used for updating E_{eff} in the projection method, is the weighted average of tension and compression curve according to the stress state of the element. As an example, for an element with stress state described by $\begin{bmatrix} \sigma_1 & 0 & 0 \\ 0 & \sigma_2 & 0 \\ 0 & 0 & \sigma_3 \end{bmatrix}$, the coefficients for the compression and tension curve are defined as, respectively, $m_c = \frac{\sum_{j=1}^{3} |\sigma_j|}{\sum_{i=1}^{3} |\sigma_i|}\ if\ \sigma_j < 0$, $m_t = \frac{\sum_{j=1}^{3} \sigma_j}{\sum_{i=1}^{3} |\sigma_i|}\ if\ \sigma_j > 0$. Figure 14 [24] provides a schematic view of this interpolation method. In this figure, f_t and f_c stand for uniaxial tensile and compressive curve. The equivalent stress-strain curve for the aforementioned stress state is the weighted average of tension and compression according to: $m_t f_t + m_c f_c$.

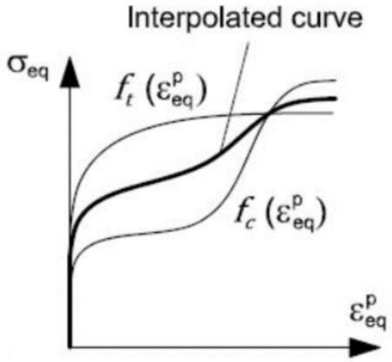

Figure 14. Schematic view of weighted interpolation method [24]

The other advantage of VMP method, which is its capability of adopting different yield criteria, shows its importance in this case. It was shown that for asymmetric materials [198], a von-Mises yield surface is unable to capture the material behavior. Accordingly, another yield surface (described later in this thesis) should be used for asymmetric materials. It is noteworthy that all the afore-mentioned numerical models are based on specific yield criteria (mostly Von-Mises) and in the current formulation, they cannot be used for other yield criteria, which results in the inability of these solutions to model asymmetric materials.

2.4 Summary

This chapter has provided a review on the literature pertaining this research. Firstly, applications of magnesium and its specific properties were reviewed. Next, a comprehensive account of the cold expansion, including its background, numerical-FE models of the process and experimental works was presented. Finally, the VMP method analytical concept and formulations as well as its applications in cold expansion and asymmetric material were reviewed. Regarding the cold expansion on magnesium alloy, there is a major gap in the literature. To the best of the author’s knowledge, there is no data available about the cold expansion on AZ31B magnesium alloy.

Chapter 3. Experimental work

This chapter introduces the experimental work in this research. The experimental work can be divided into three different parts: 1) pre-cold expansion (material characterization), 2) cold expansion testing including sample preparation and displacement measurements, and 3) post-cold expansion, including residual stress measurement, fatigue testing and texture evolution due to cold expansion.

3.1 Material characterization

The material used in this work is AZ31B-H24 provided by Magnesium Electron of North America (MENA), which is manufactured by rolling the direct chill cast ingots. The sheet was obtained in 4 mm and 3.18 mm thickness. Its chemical composition is presented in Table **1**.

In the VMP method, actual material loading and unloading behaviors are needed to model the cold expansion process. To obtain these behaviors, two sets of test were done. Sample geometry employed during these tests is displayed in Figure 15.

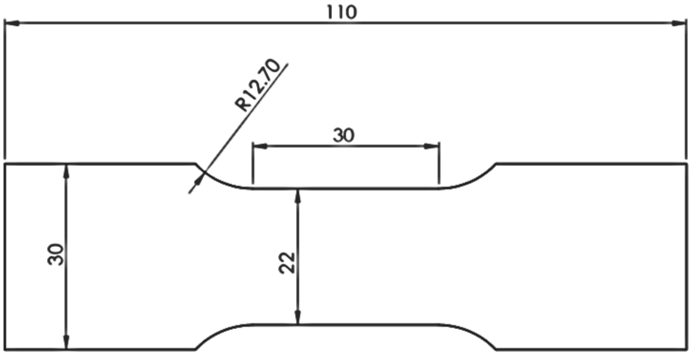

Figure 15. Sample geometry for monotonic and TC-CT tests (all dimensions are in mm)

3.1.1 Monotonic loading

Two monotonic tests, one in compression and one in tension were done on specimens with geometry shown in Figure 15, with the length along the RD direction. Tests were performed using a MTS 810 series servo-hydraulic load frame, with a maximum load capacity of 50kN, and a test displacement rate of $0.015\ \frac{mm}{sec}$, which was chosen according to ASTM standard [199]. Strain was captured by digital image correlation (DIC) technique, using Aramis 3D system with two high resolution CCD cameras. To facilitate DIC measurement, and black and white speckle pattern was applied along the side of the specimen (Figure 16b). the strain values showed here, is the average of strain over the straight section of the specimen, with gage length of 30 mm.

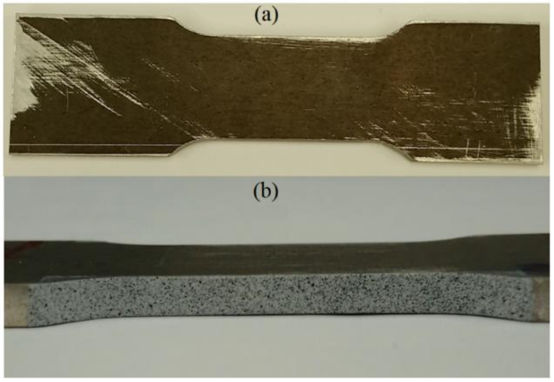

Figure 16. a) specimen for monotonic test, b) painted sample for DIC

The result of the monotonic tension test is shown in Figure 17.

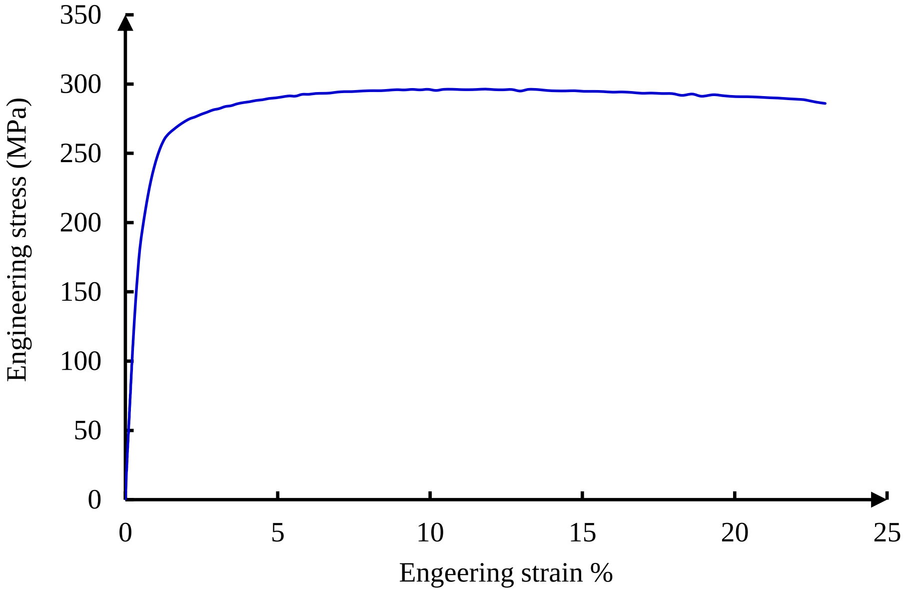

Figure 17. Monotonic tension behavior in rolling direction

For compression testing, an anti-buckling fixture was used to prevent buckling, since the high values of strain required, made the sample susceptible to buckling.

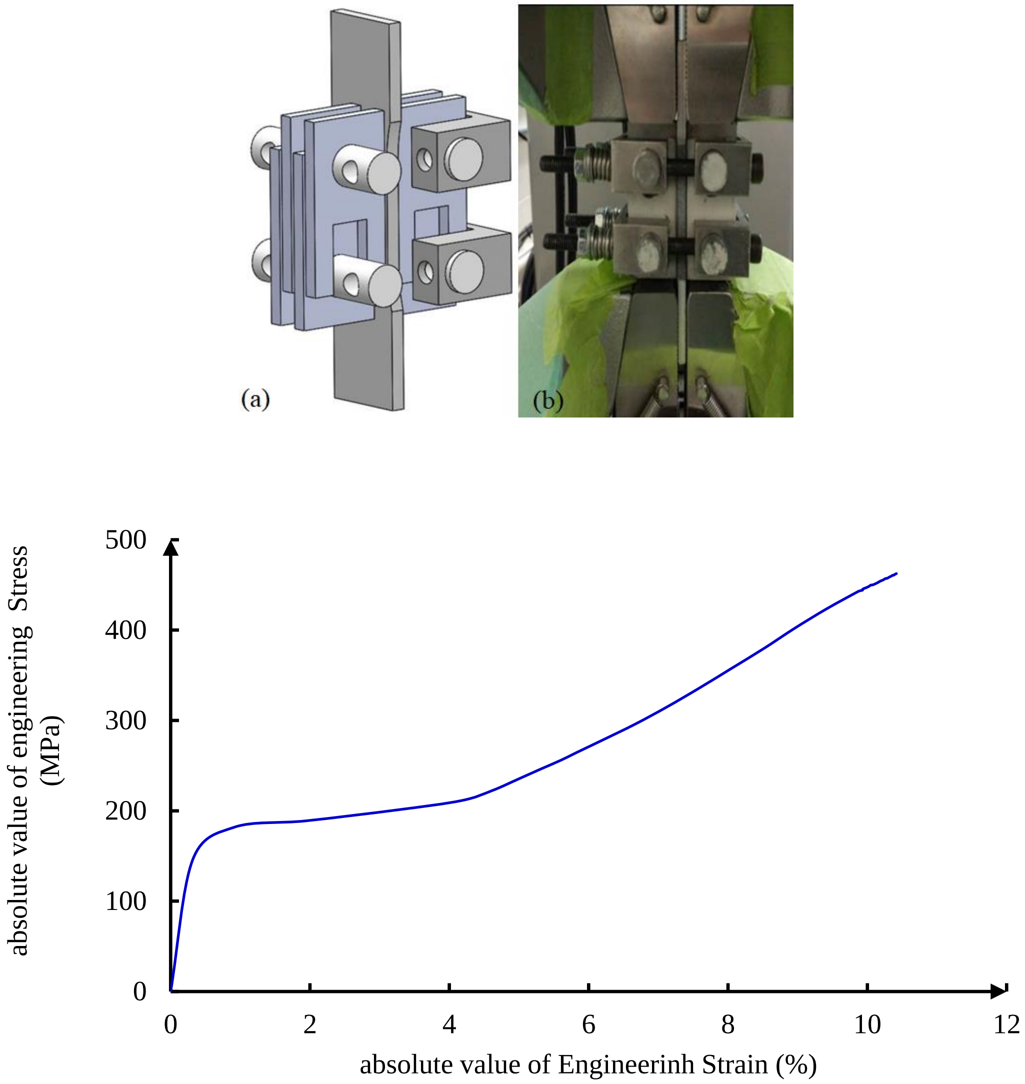

Figure 18. a) Anti-buckling fixture, b) mounted sample using anti-buckling, c) monotonic compression stress-strain curve

Table 2. Summary of monotonic behavior of AZ31B in RD direction

	0.2% yield stress (MPa)	UTS (MPa)	Fracture strain (%)
Tension	220	296	23
Compression	174	460	10.4

The values reported in this table are average of the measurements of the current work and measurements on the same material from literature[23] with standard deviation of 3.5 and 0.6 Mpa for yield and ultimate strength, respectively.

3.1.2 Compression-tension (CT) and tension-compression (TC) tests

To model the cold expansion process using VMP, mandrel insertion is simulate as the loading step and consequent removal of the mandrel the unloading step. Therefore, the unloading behavior of the material from different values of overstrain is needed as an input for the VMP simulation. To do so, five specimens with same geometry (Figure 15) were loaded up to specific strain values of 2%, 4%, 6%, 8%,10 % and then loaded in the opposite direction up to failure. The Following figures are the results of CT, TC tests, respectively.

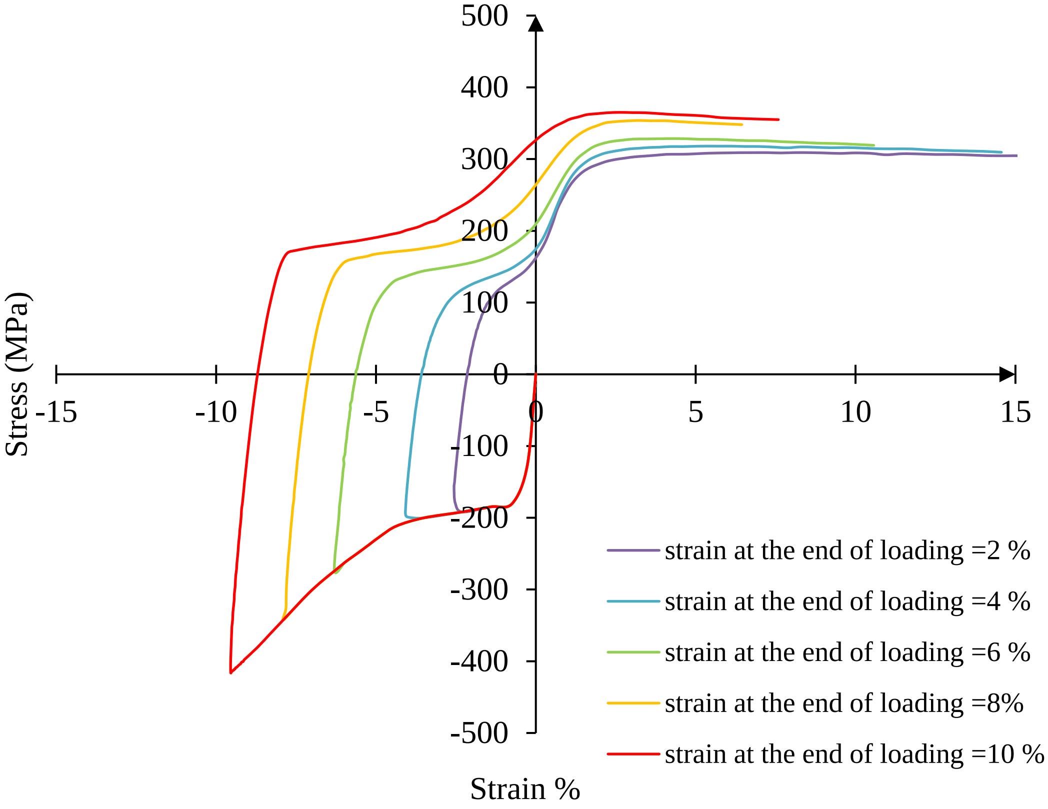

Figure 19. Compression-tension curves at different level of strain [200]

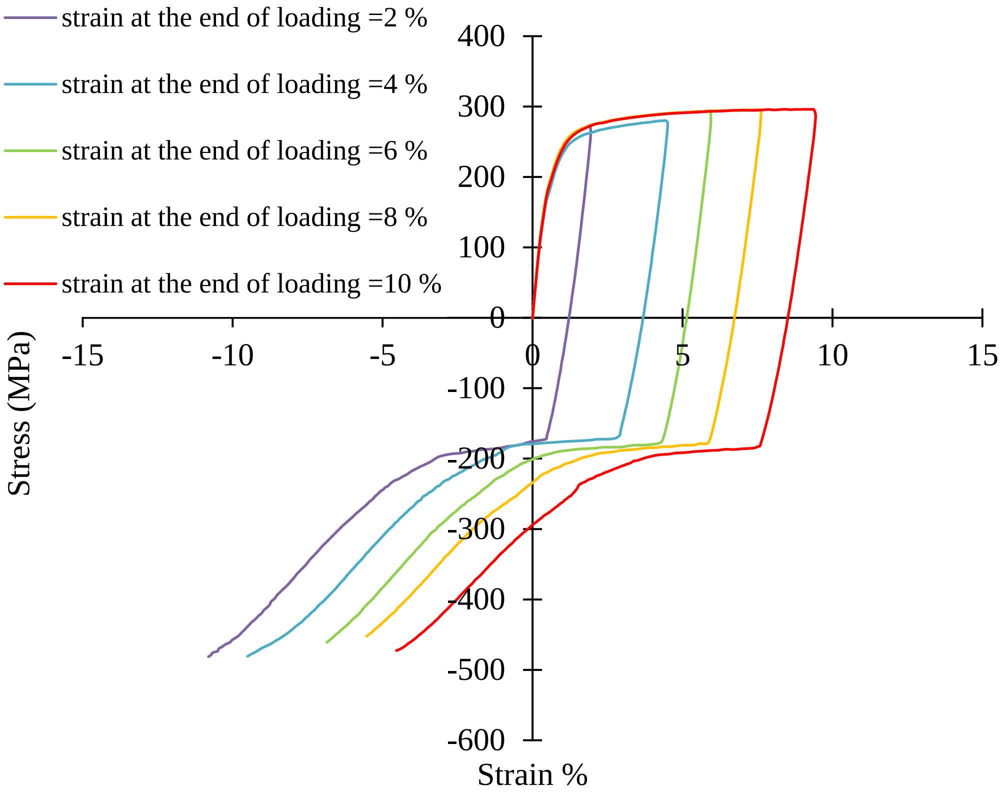

Figure 20. Tension-compression curve at different level of strain

3.2 Cold expansion

The cold expansion process consists of a tapered mandrel fitted with a fixed split sleeve being pulled through the notch. Due to individual conditions required for measurements during tests, a specific structure was designed to facilitate the test, instead of using commercial cold expansion kits.

3.2.1 Apparatus: mandrel-split sleeve

For this study, a nominal diameter of 6 mm was chosen as the dimension of the hole before cold expansion. Then a standard mandrel and split sleeve suitable for this diameter (Figure 21).

Figure 21. Mandrel and split sleeve

The maximum diameter of the mandrel is 5.84 mm and the thickness of the split sleeve is 0.20 mm. Thus, for the initial diameter of 6.0 mm, according to Equation (1):

$$\text{CE \%} = \frac{(D_{Mandrel} + 2t_{split\ sleeve}) - D_{hole}}{D_{hole}} \times 100 = \frac{(5.84 + 0.2 \times 2) - 6.00}{6.00} \times 100 = 4\ \%$$

The mandrel was manufactured from high strength steel, and the sleeve from stainless steel with a longitudinal split. The type of the split sleeve used in this research is flared, which means one of the edges is flanged (Figure 22). The length of the split sleeve is 26.70 mm. According to standard [201], the length should be at least 0.8 mm more than the thickness of work piece. In current study, as will be stated in more detail in next sections, the thickness of work piece is 4 mm, so the length of split sleeve satisfies this condition well. The split sleeve is also pre-lubricated to decrease the required driving force on the mandrel.

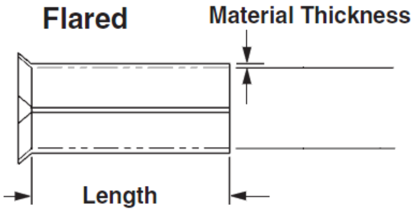

Figure 22. Flared split sleeve [201]

3.2.2 Design of the structure for cold expansion process

To make it possible to perform the cold expansion test with available facilities and in a way compatible to the displacement measuring technique (DIC), a specific fixture was designed so that MTS servo-hydraulic machine could be used as the puller unit for the mandrel. A schematic view of this fixture is shown in Figure 23.

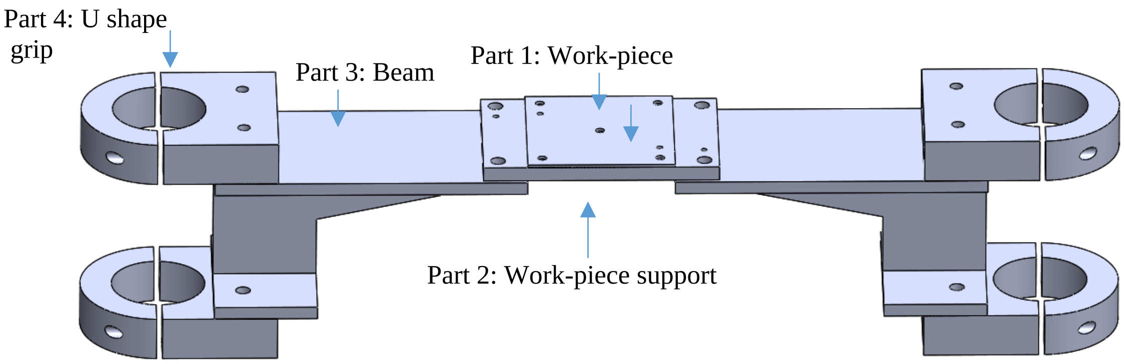

Figure 23. Schematic view of CE fixture

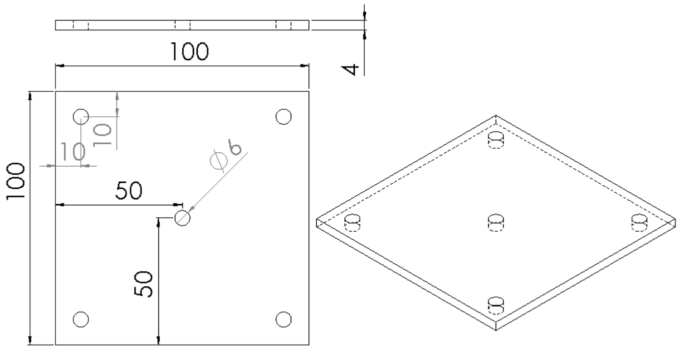

Figure 24. Geometry of the work piece (all dimensions are in mm)

The fixture is consist of:

1. For supporting the work-piece, two I-beams (part 3) were used. To reduce the total weight of the structure they were cut into the shape illustrated in Figure 24.
2. To hold the whole structure, four U-shape part were used to secure it to the column of the MTS machine.
3. Four bolts were used to attach the work-piece to the support; also, two dowel pins were utilized to align it perfectly in its designated place. As in the work piece, dowel pins were used to align the support of the workpiece. These dowel pins were positioned in an X pattern to prevent rotation of the part.

The main challenge in the design process of the structure was the support of the split sleeve. In the commercial cold expansion kit, a tapered nose cap holds the split sleeve in place during expansion. A similar component was used here, Consisting of a bolt with a center hole of a diameter slightly larger than the maximum diameter of the mandrel, with a tapered edge to support the flanged bottom of split sleeve (Figure 25).

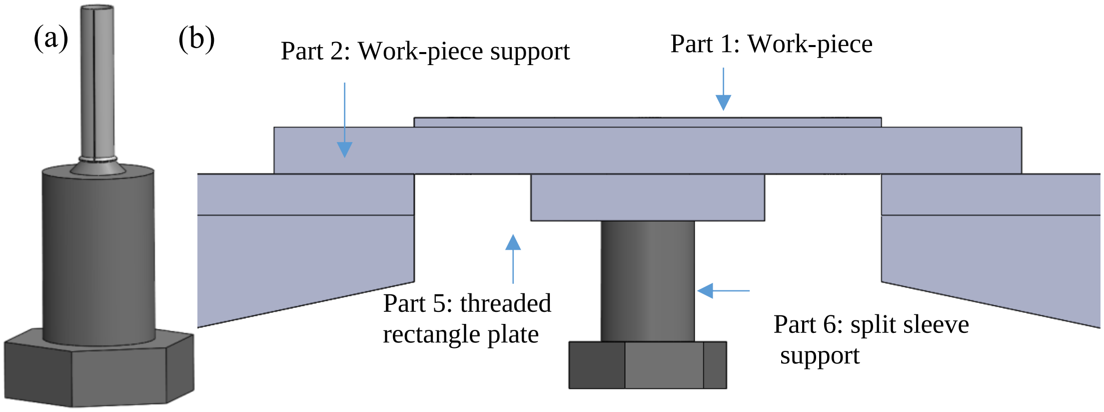

Figure 25. a) Split sleeve support, b) final assembly of split sleeve support

This bolt is attached to a threaded rectangular plate (part 5), which itself is attached to the structure by four bolts.

For the integrity of the cold expansion process, the alignment of the mandrel with respect to the hole plays an important role. Using a fixed position for the mandrel will not guarantee perfect alignment, because there would be no control over the relative position of the mandrel with respect to the hole on work piece. Therefore, a fixture capable of self-aligning was proposed as the solution. The idea relies on the fact that a floating mandrel will self-align itself since the oversized mandrel has to be concentric with respect to the hole when it is pulled through the notch. As shown in Figure 26, the threaded end of the mandrel (Figure 21) is attached to part 9, which is floating in the bigger cylinder (part 10). Because of the bigger inner radius of part 10, the mandrel can easily float inside. The rectangle-shaped end of part 10 is gripped by the MTS machine jaws. After assembling all parts, part 8, the lid of the fixture, applies the force on the mandrel. When the cross-head of the MTS machine descends, the mandrel is pulled down through the hole, while the split sleeve is already fixed by its support. Therefore as soon as the major diameter of the mandrel reaches the work piece, expansion occurs.

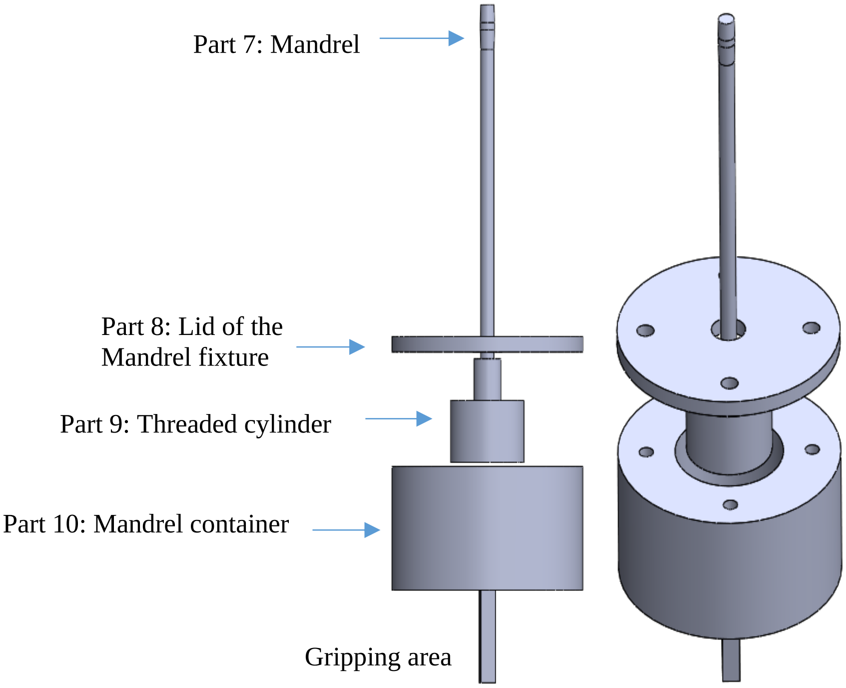

Figure 26. Schematic view of mandrel floating fixture

3.2.3 Cold expansion test and experimental measurements

3.2.3.1 Cold expansion test

Figure 27 shows the structure mounted on MTS machine.

Figure 27. Designed structure mounted on MTS, (left), detailed view of the work piece and mounted split sleeve (right)

In this study, the MTS cross-head was moved down at the speed of 10 mm/min.

3.2.3.2 Displacement measurements

To capture the displacement around the notch during expansion at the end of the loading step (i.e., when the notch is expanded to the maximum diameter), DIC technique was used. To do so, a small area around the notch was painted with contrasting speckles (Figure 28). To calculate the radial displacement, a virtual circle is fitted to the virgin condition of the specimen to locate the center of the hole (Figure 29). Various points are defined on the surface, in the radial direction of the sheets. Therefore, the difference between the coordinates of the points in the first image (virgin condition) and the corresponding image would be the radial displacement. Due to the resolution of the camera sensors and the focal length of the optics, the minimum distance between defined points is limited to 300 µm. The image that represents the circumstances of the end of loading would be the stage in which the maximum radial displacements of all points occurs. Figure 30a shows the displacement of the closest point to the notch.

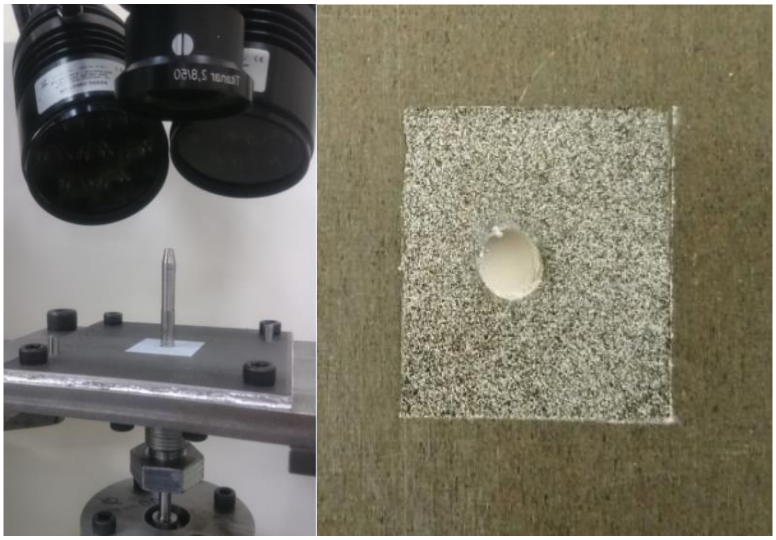

Figure 28. a) DIC set up, b) painted sample

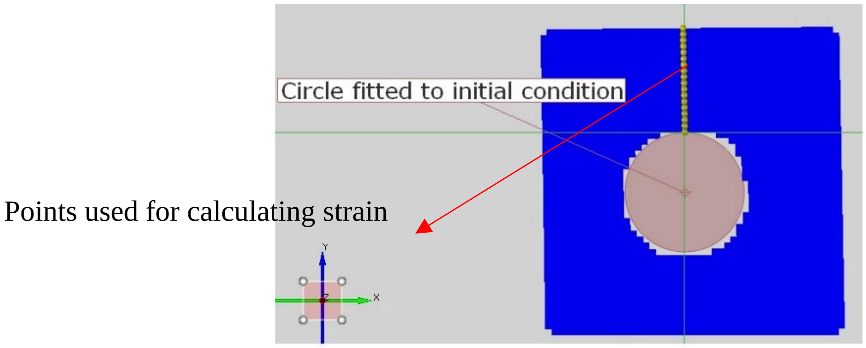

Figure 29. Fitted circle to the virgin condition of the notch

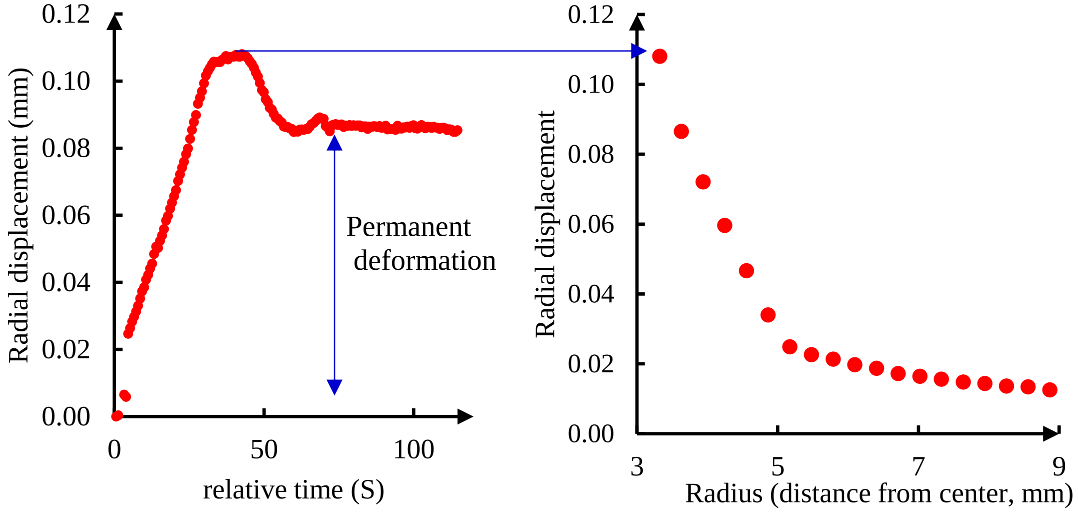

Figure 30. Radial displacement of a specific point during expansion (left), radial displacement around the notch as a function of radius (right)

As expected, the displacement starts to increase as the mandrel moves down, and reaches its maximum value (when the major diameter of the mandrel is in contact with the surface). It then decreases due to unloading, and eventually it reaches a constant value, which is the permanent change in diameter. This value (0.085 mm) is in perfect agreement with the measured diameter of cold expansion (6.17 mm). The results of the measured radial displacement around the notch is presented in Figure 30.

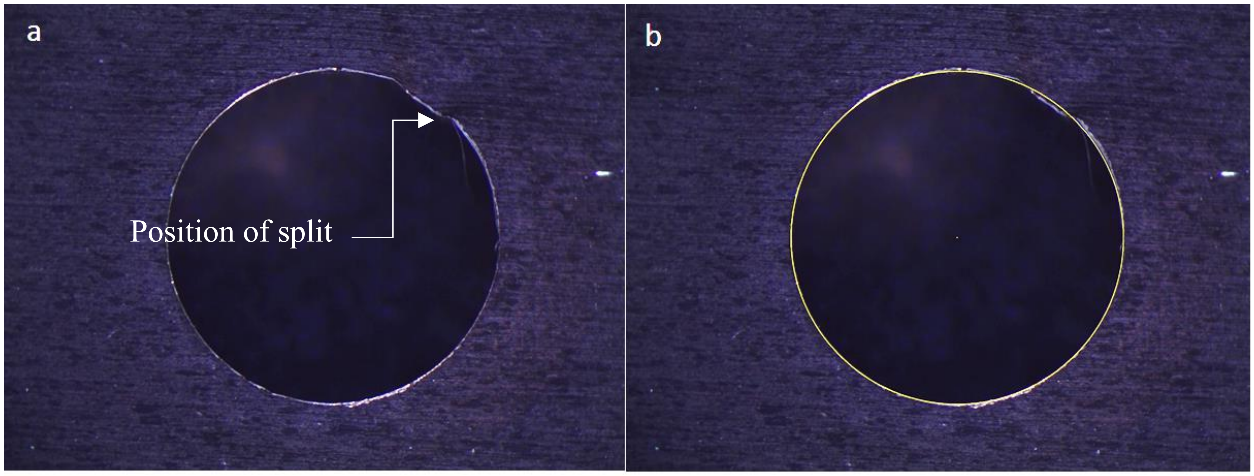

Figure 31. a) Effect of split, b) fitted circle to the hole after expansion

Figure 31 shows that the effect of a split is local, and the shape of the hole after cold expansion remains circular.

3.2.3.3 Residual stress measurements

In order to measure the induced residual stress around the notch due to cold expansion, X-ray diffraction (XRD), (one of the most practical ways of measuring residual stress), was used in this study. The concept of using X-ray is based on the fundamentals of Bragg's law. As depicted by Figure 32, in a strain free sample with a lattice space of d_0, the X-rays are diffracted at angle of θ_0. The wavelength of the X-ray is given by:

$$\lambda = 2d_0 \sin(\theta_0) \tag{17}$$

In a deformed sample, the lattice space of the crystals is changed, but according to Bragg's law, the wavelength remain constant:

$$\lambda = 2d \sin(\theta) \tag{18}$$

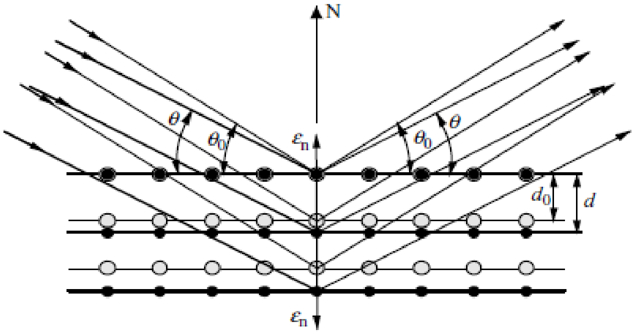

Figure 32. X-ray diffraction according to Bragg's law [202]

This difference in the diffraction angle of the X-ray beams, gives the strain field in the sample. Assuming the residual stress is in the elastic regime, these strain fields are converted to residual stress easily. As one of the most important advantages of XRD method, it should be mentioned that this process is non-destructive.

In this study, a Brucker D8-Discover diffractometer (Figure 33) was used with an x-ray collimator diameter of 0.3 mm and a X-ray chromium tube. Considering edge effects and collimator diameter, the closest distance from the cold-expanded hole was chosen to be 0.2 mm. To make sure the results of the XRD are repeatable, measurements were done on three lines (Figure 34) far from the position of the split. As mentioned, the effect of the split is local and far from it, the process should remain axisymmetric.

The results of residual stress measurements for a 5% cold expanded sample (initial dimeter of 5.95) are presented in the following graphs and tables.

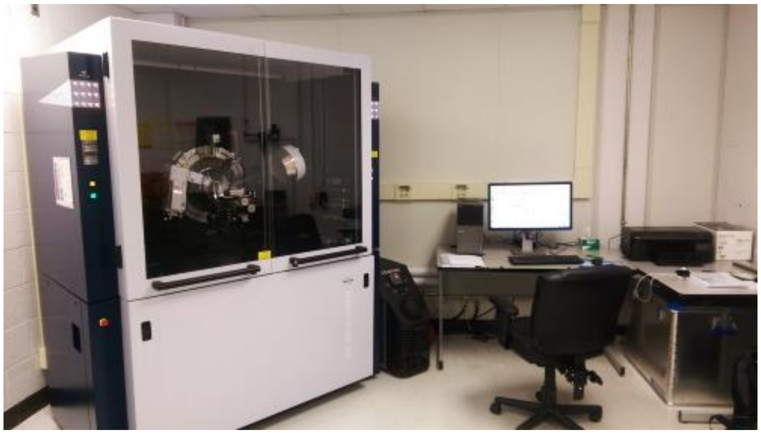

Figure 33. Brucker XRD machine

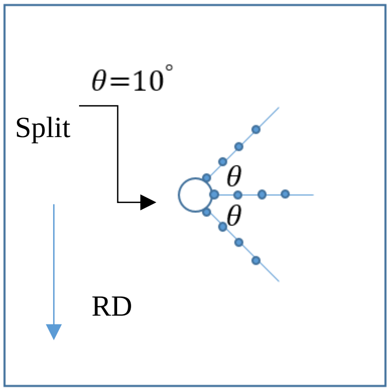

Figure 34. Position of the points for XRD measurements

Table 3. XRD measurements of residual Hoop stress (mandrel entrance side)

	Hoop stress (MPa)					
R (mm)	Line 1	Error	Line 2	Error	Line 3	Error
0.2	-14.4	3.1	-19.4	4.4	-10.9	3.2
0.5	-6.4	2	-7.3	2.2	-8.5	2
0.8	-2	1.9	-2.3	2	-3.3	1.8
1.1	1	1.9	-1.9	1.9	3.2	1.8

Table 4.XRD measurements of residual radial stress (mandrel entrance side)

	Radial stress (MPa)					
R (mm)	Line 1	Error	Line 2	Error	Line 3	Error
0.2	24.2	3.1	23.3	4.2	19.3	3
0.5	31.9	2	31.5	2.2	30.7	2
0.8	33.3	1.9	31.4	2	29.3	1.8
1.1	23.6	1.9	25.7	1.9	24.3	1.8

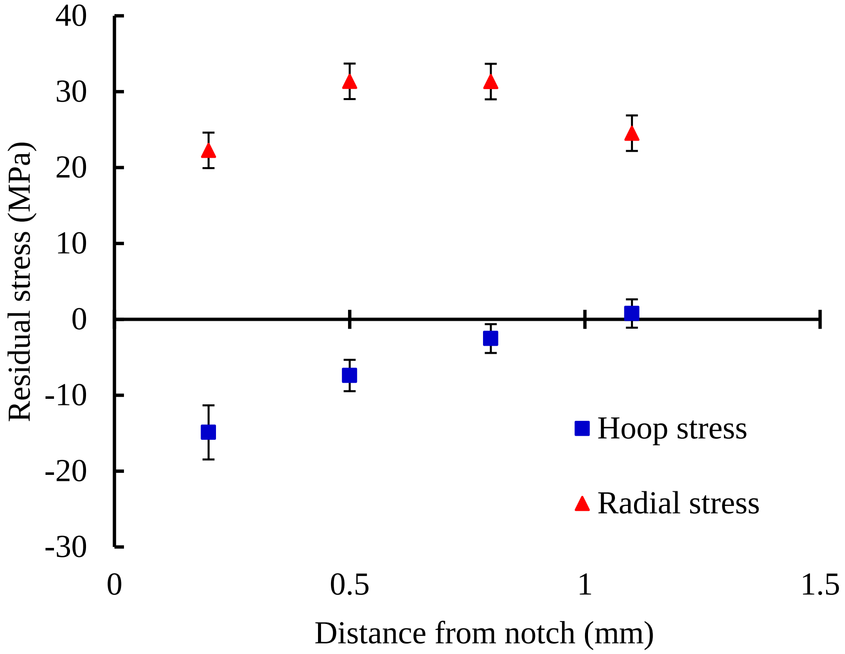

Figure 35. Residual stress distribution on the entry side of 5 % cold expanded sample

Table 5. XRD measurements of residual hoop stress (mandrel exit side)

	Hoop stress (MPa)					
R (mm)	Line 1	Error	Line 2	Error	Line 3	Error
0.2	-49.6	3.4	-43.6	4.3	-53.8	3.4
0.5	-53.8	2.1	-53.8	2.2	-53.9	2.1
0.8	-50.7	1.9	-48.2	1.9	-47.5	1.8
1.1	-44.1	1.9	-48.6	1.8	-45.6	2

Table 6. XRD measurements of residual radial stress (mandrel exit side)

	Radial stress (MPa)					
R (mm)	Line 1	Error	Line 2	Error	Line 3	Error
0.2	23.5	3.1	20	4	23.4	3
0.5	30.9	2.1	27.1	2.2	26.8	2.1
0.8	22.8	1.9	19.9	1.9	23.4	1.8
1.1	12.4	1.8	11.5	1.8	11.5	2

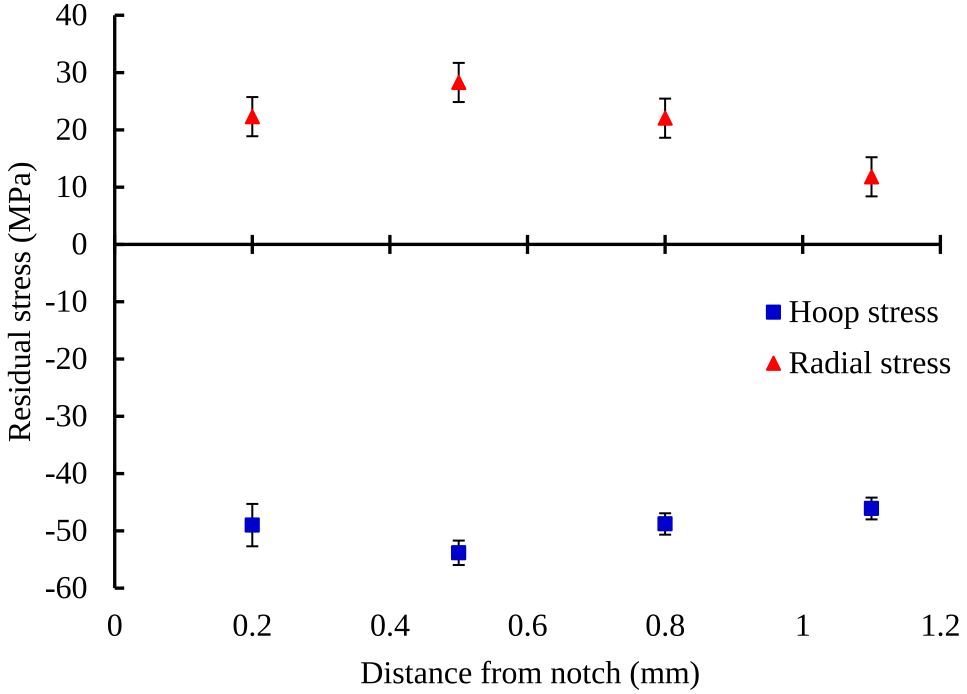

Figure 36. Residual stress distribution on the exit side of 5 % cold expanded sample

To make sure that the reported residual stress is created by the cold expansion process, XRD measurements were performed on an as-received sample (before cold expansion). The results are presented in Table 7. Residual stress measurement on as received sample Side one and side two are two different side of the sheet. The average of these values is very close to zero, so they were not considered in the reported residual stress in this study.

Table 7. Residual stress measurement on as received sample

	Side 1		**Side 2**		**Average**	
R	Radial	Hoop	Radial	Hoop	Radial	Hoop
0.2	1.1	0.4	-12.2	-4.8	-5.55	-2.2
0.5	-3.2	-2.2	-10.6	-7.8	-6.9	-5
1	-3.4	2.1	-2.9	1.3	-3.15	1.7
1.5	8.2	4.8	5.9	5.8	7.05	5.3

To investigate the effect of different percentages, measurements on the 4% cold expanded sample were done on both entry and exit faces, as shown in Figure 37.

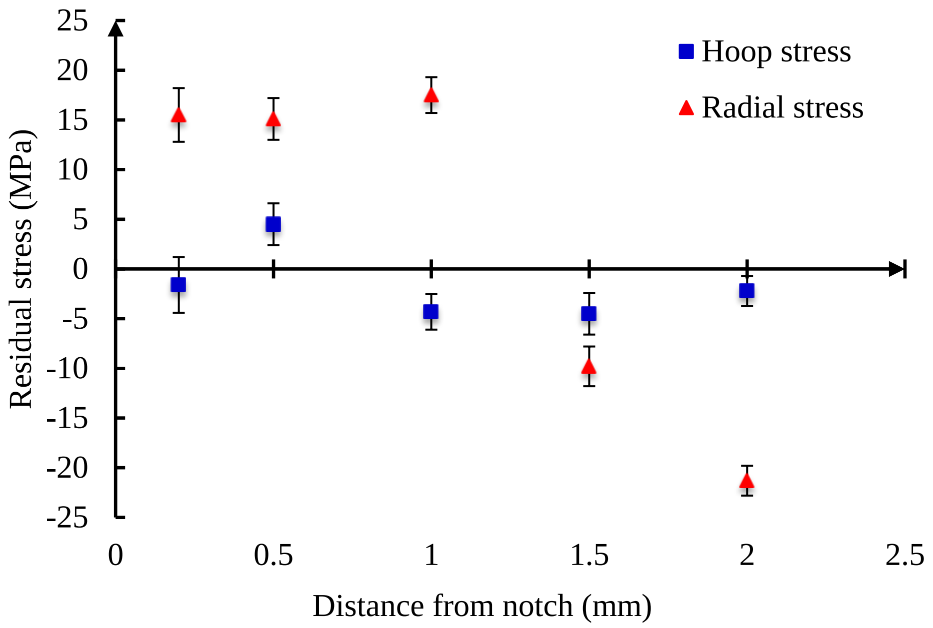
Entry face

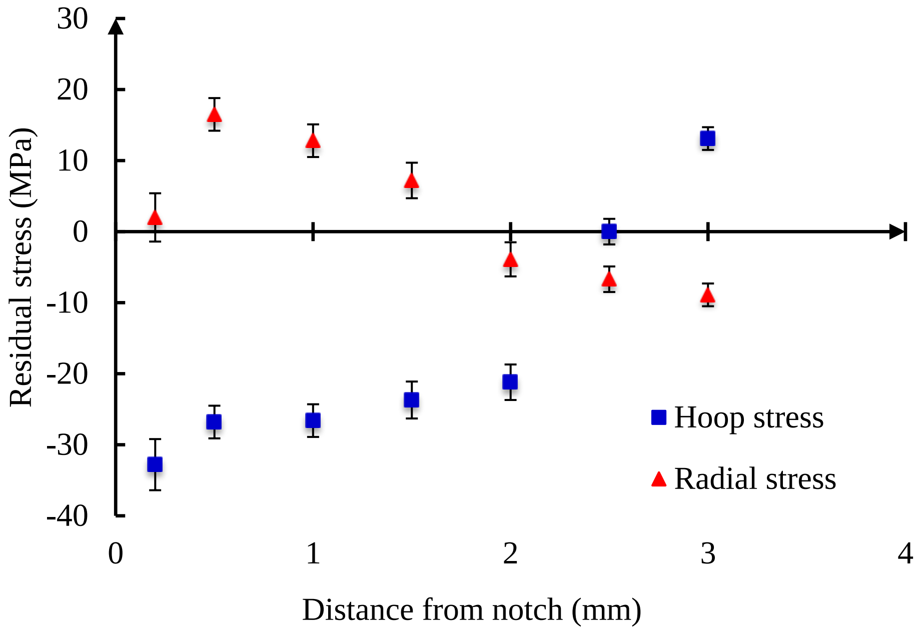
Exit face

Figure 37. Residual stress distribution on the entry and exit side of 4 % cold expanded sample

As expected, the hoop residual stress has a higher value at the exit side of the mandrel for both 5% and 4% single cold expansion. Despite the fact that the specimen undergoes a fair amount of plasticity during loading, hoop residual stress is roughly zero for the 4% cold expanded sample on the entry site. On the other hand, while unloading in the both entry and exit side of the 4% cold expansion and entry side of the 5% seems to be elastic, on the exit side of the 5% reverse yielding occurs. The other noteworthy characteristic of residual stress distribution on the exit side is the area that has compressive residual stress on the exit side, which is considerable compared to the entry face. As mentioned in Chapter two, the compressive residual stress zone can very well affect the crack propagation behavior of the specimens. The other specific aspect of the created residual stress field is the sign of the residual stress in the radial direction. While in materials such as steel and aluminum, residual radial stress has a negative value [203][139], measurements show that for AZ31B-sheet radial residual stress has a positive value for both sides near the notch and then goes to a negative value (Figure 37). This feature can be attributed to the unique behavior of the magnesium sheet. The biaxial stress state of each element dictates that one of the stress components is in a direction that has different behavior than that of the other. For example, in Figure 34, for the elements on the line in the center, radial stress is in the RD direction while tangential stress is in TD direction, which shows slightly different behavior [23]. Secondly, as can be seen in Figure 19-Figure 20, while the unloading from the tension curve is similar for all level of pre-strain, the unloading form compression intensively depends on the amount of pre-strain.

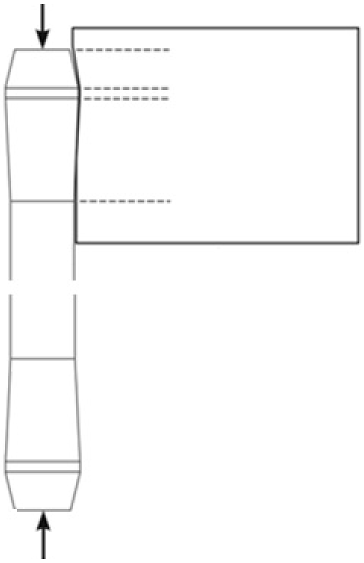

Figure 38. Schematic view of opposite direction double cold expansion

3.2.3.4 Double cold expansion

As shown in section 3.2.3.3, single cold expansion creates non-uniform residual stress distribution through the thickness of the work piece. As a solution, double cold expansion was proposed. There are two possible ways of doing the second expansion, one with the same configuration as the first pass (i.e. the entry face of the first and the second expansion are the same), known as same direction double expansion (SDDE). The other one, known as opposite direction double expansion (ODDE), consist of two pass cold expansion, in such a way that the exit face of the first pass is the entry face of the second expansion. It was shown that ODDE results in more uniform residual stress distribution [147]. To examine the effect of double cold expansion, ODDE was chosen as our method. To do so, the specimen was flipped after the first pass of the mandrel. Other parameters, such as mandrel speed remained the same. Comparison of the measured residual stress field on the entry side (of first pass) for 5% (initial diameter of 5.95) is presented in Figure 39.

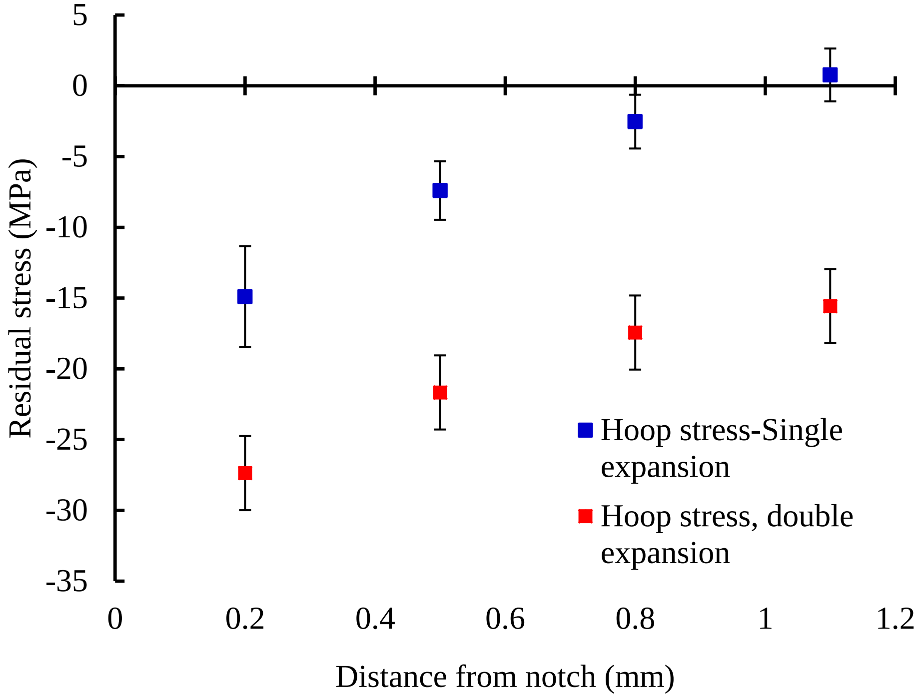

Figure 39. Hoop residual stress after single and double cold expansion on the entry side of 5% cold expansion

Measurements clearly show that double cold expansion significantly increases the magnitude of the residual hoop stress at the entry side (of the first pass). It seems that the unloading phase for the entry side remains elastic. I

To verify the residual stress measurements by XRD technique, another method of measuring residual stress called hole drilling was utilized. The concept behind the hole drilling method (proposed in 1966 [204]) is similar to XRD, in which measured residual strain is converted to residual stress. To determine the residual strain at a specific point, a rosette of strain gauges attached to the specimen, measures the released deformation after making a precise hole at that point (center of strain gauges) [205]. In this study, measurements were made on the entry face of 4% ODDE. The properties of the strain gauges are shown in Table 8.

Table 8. Properties of the strain gauges

Name	**Configuration**	**Gage width (mm)**	**Gage length (mm)**	**Gage factor**	**Resistance (ohms)**
K-RY61-1.5/120R-B	Counter clockwise	1.5	0.77	1.93	120

It should be mentioned that calculating the residual stress by hole drilling requires the yield strength of the material. Since during cold expansion compressive stress is dominant, the value of compressive yield of the material is implemented in hole drilling calculations. Two limitation of this method in the case of current study are listed as follows:

- Hole drilling is a semi-destructive method, since small holes of up to 2mm are drilled.
- Due to the size of strain gauges and the hole created on the specimen, this method cannot be used to measure residual stress at points very close to notch.
- Compared with XRD, it needs more time to set up the test equipment.

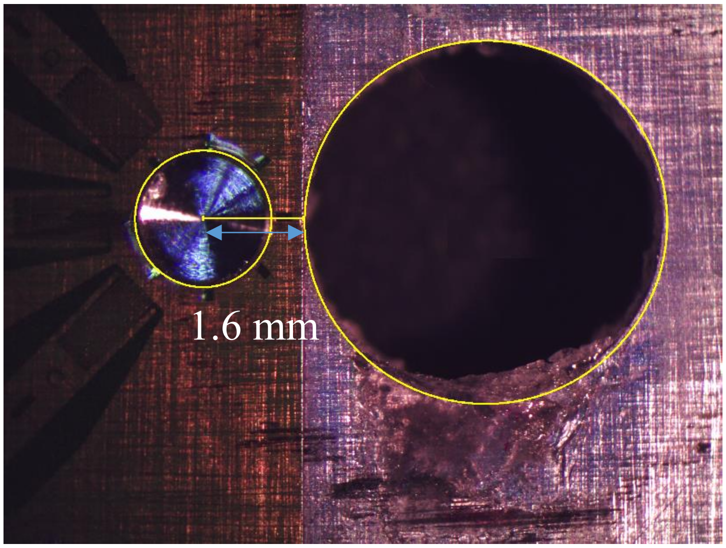

Figure 40. Attached strain gage to the 4% DCE sample

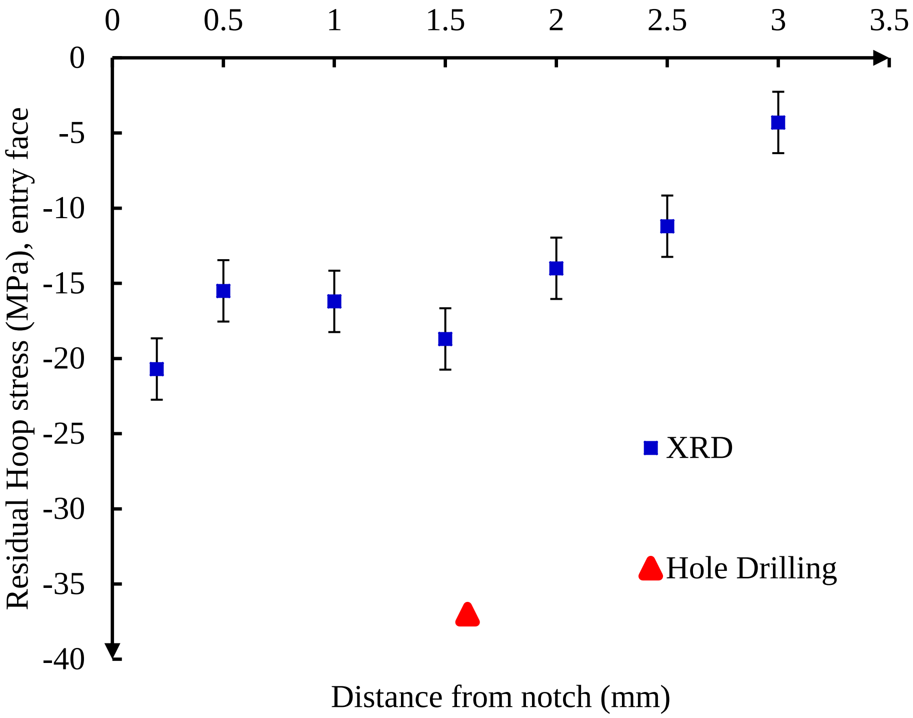

Figure 41. Comparing residual stress by XRD and hole drilling for 4% DCE

It should be mentioned that hole drilling measures residual stress through thickness (in this case 1mm from surface). The value reported in the above figure is the average of the residual stress from entry surface to 1mm below it. Since the residual stress increases going from the entry face to the exit face, the residual stress reported by hole drilling is expected to have a higher value from XRD, since based on the method proposed in [206] the value reported by XRD is the average from surface to approximately 32 μm below.

3.2.4 Optimum cold expansion percentage

As described in Chapter 2, the idea behind the cold expansion is to create compressive residual stress by imposing plastic deformation in order to increase the fatigue life of the work piece. Section 2.2.3.2 has provided a brief review of the definition of optimum cold expansion percentage. Next, in this study, the optimum configuration is based on the maximum fatigue life after cold expansion.

3.2.4.1 Effect of different cold expansion percentages on fatigue life.

The value of the degree of expansion has a range between zero (un-cold expanded) and a maximum value of 6% for standard tools, in the case of split sleeve cold expansion [164]. In this study, four different values (listed below) for cold expansion percentage were used.

Table 9. Different cold expansion percentage used to find the optimum

Initial diameter (mm)	Cold expansion percentage %	Nominal Value of CE%
6.1	2.4	2
6	4	4
5.95	4.87	5
5.9	5.76	6

To find to the optimum value of the cold expansion percentage, a series of fatigue tests were done on the samples with above-mentioned values of CE%. Since the value of imposed residual stress at the entry face of single cold expansion is very small, fatigue tests were done on double cold expanded samples to have a better contrast against the fatigue life of the as-received sample. As mentioned in Chapter 2, the effect of residual stress is very small in low cycle fatigue. Therefore, the fatigue tests were done on the load level that resulted in around 10^5 cycles.

To calculate the stress at the notch root, Roark's formula [207] was used. For a central circular hole (in un cold expanded sample) in a plate with axial load in the elastic regime:

$$k_t = 3.00 - 3.13\left(\frac{d}{D}\right) + 3.66\left(\frac{d}{D}\right)^2 - 1.53\left(\frac{d}{D}\right)^3 \tag{19}$$

in which D is the width of the sheet and d is the diameter of the notch. to calculate stress intensity factor, nominal diameter of 6mm was used. The geometry of the specimen is shown below.

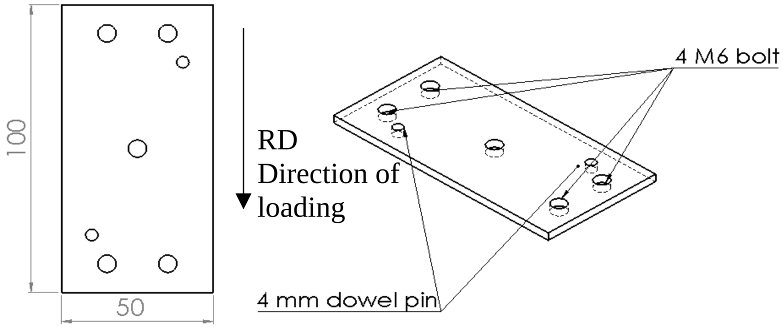

Figure 42. Geometry of the specimen for fatigue test

The stress at the notch root was found to be equal to 170 MPa, for a fatigue life of around 10^5 cycles in un-cold expanded sample. The fatigue life shown in the following graph is the final fracture life. Tests were done with a frequency of 10 Hz. The position of the split was at the notch crown for all specimen.

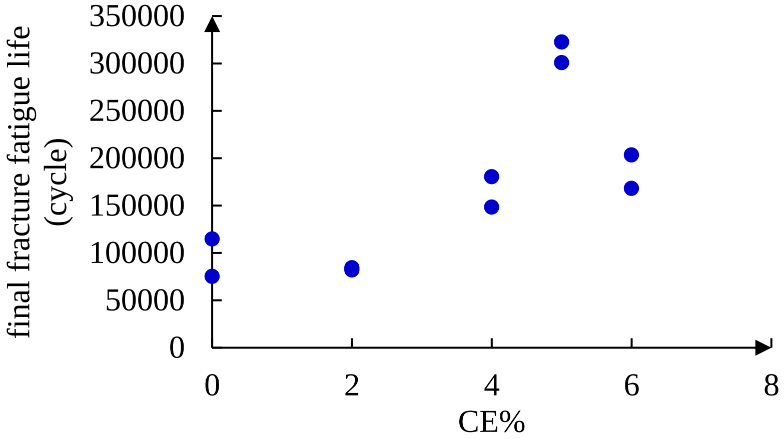

Figure 43. Final fracture fatigue life at different CE%

Figure 43 clearly shows that the value of cold expansion is 5% (with 5.95 mm initial diameter). To explain this phenomenon, two factors should be considered. First is the value of residual hoop stress at notch root. Greater values of residual stress will result in lower effective stress at the notch root, leading to higher fatigue life. As discussed thoroughly in section 2.2.3.2, up to a specific value, a higher level of plastic deformation during expansion creates greater residual stress. For even higher level of expansion, reverse yielding occurs, which results in lower residual stress at the notch root. On the other hand, severe deformation can cause cracks in the work piece, which will have detrimental effects on fatigue life. Due to the low formability of magnesium at room temperature, macro-cracks seemed to be possible after double cold expansion. Thus, as the first step to justify the observed fatigue behavior of the double cold expanded sample, the well-known dye-penetration technique was used to detect any macro-cracks on the surface of the notch, where the split sleeve is in contact with the work piece and the plastic strain has the highest value. Figure 44 shows the main steps of the dye-penetration procedure. The concept of the dye penetration procedure is to use a very low-viscosity liquid which can easily penetrate very small cracks. The process includes four main steps: a) cleaning the surface, b) applying the penetrant, c) removing the penetrant and d) applying the developer (Figure 44). As the first step, the surface should be cleaned. Then, the penetrant (usually a dark red liquid) is applied on the surface (step b). After cleaning the surface (step c), if there is any damage, penetrant will remain inside the crack. Therefore, applying the developer (usually white) will highlight that area (step d).

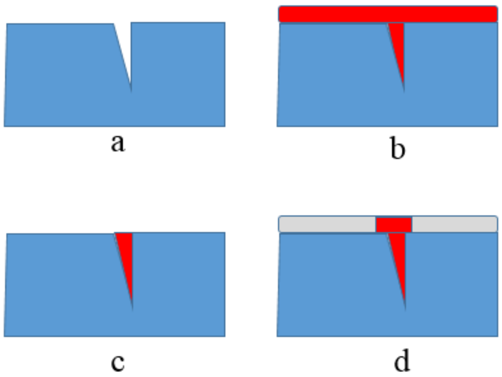

Figure 44. Dye penetration steps

For the case of this study, a spot check dye penetration kit was used. Surprisingly, none of the samples showed macro-cracks, even at the position of the split, which is the most probable location for cracks due to the cold expansion process [120], since the deformation is more pronounced.

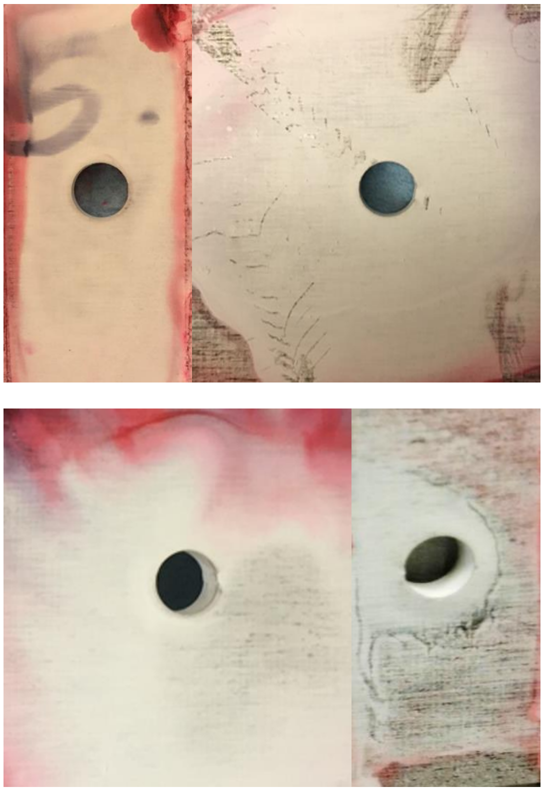

Figure 45. Dye penetrated DCE sample, from left to right: 2,4,5,6 % DCE

The result from the dye penetration test is in agreement with the fatigue test results, since in the presence of macro-cracks, the residual stress will be released. Therefore, the fatigue life of the cracked specimen cannot be more than that of the un-cold expanded sample. Because no macro-cracks exist in the double cold expanded samples, for the second step, the residual stress distributions were compared. Because the fatigue life improvement of the 6% cold expanded sample is lower than that of the 5% sample, this comparison in only made for these two conditions. It should be mentioned that since the critical location is the entry side, where the residual stress has a lower value, measurements were done on the entry side.

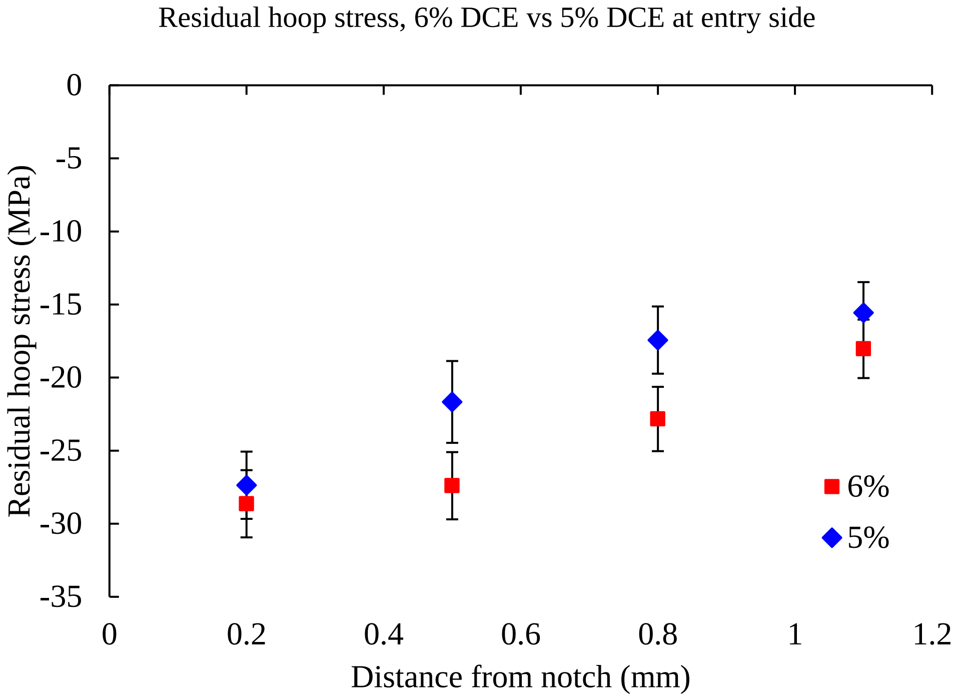

Figure 46. Comparison of the hoop residual stress after double cold expansion for 5 & 6 %

The created residual hoop stress in 5% and 6% DCE are close to each other, especially near the notch. Accordingly, the significant difference observed in the fatigue life improvement can not be attributed to the residual stress.

The next possible reason are the micro-cracks created in the work piece because of severe plastic deformation. To detect micro-cracks, a scanning electron microscope (SEM) was used. For a better contrast during imaging, the samples were etched.

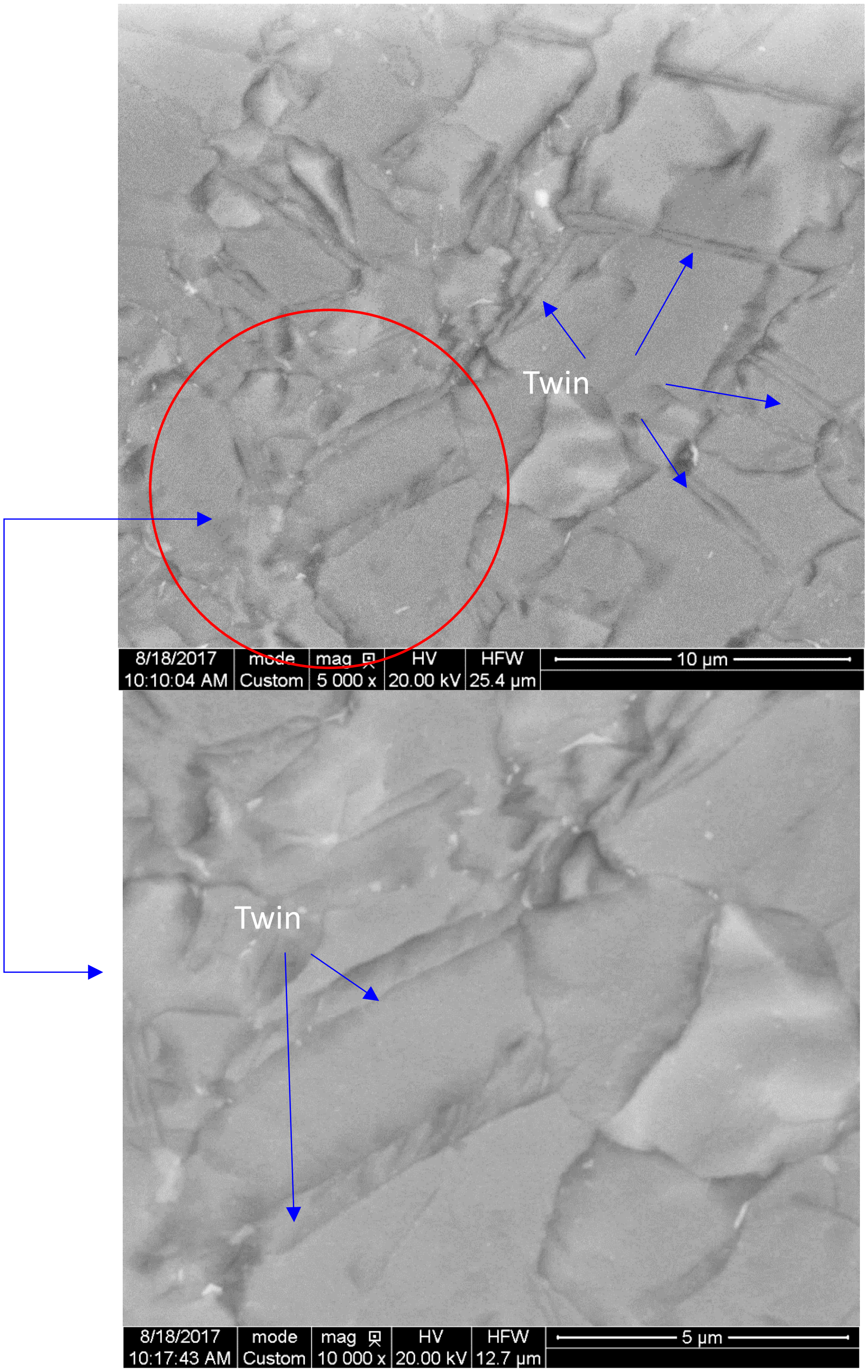

Figure 47. SEM picture of the cross section of 5% DCE sample low (top) and high (bottom) magnification

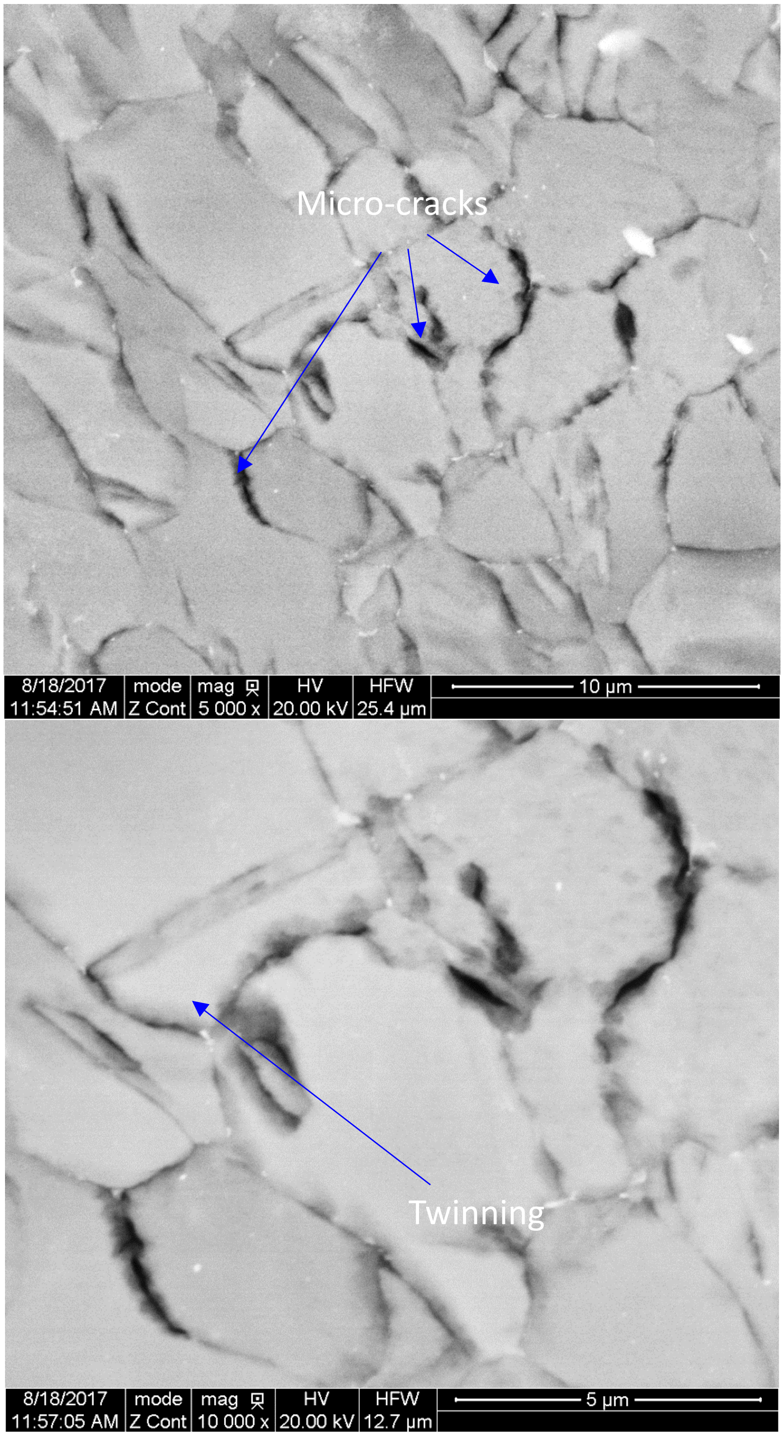

Figure 48. SEM picture of the cross section of 6% DCE sample low (top) and high (bottom) magnification

The Figure 47Figure 48 clearly shows some micro-cracks in the 6% double cold expanded sample. Although the length of these cracks is very small (3-5μm), during fatigue tests they can be a reason for faster crack initiation, which eventually results in lower fatigue life.

It should be noted that most of these micro-cracks are generated at grain boundaries and is mainly due to Grain boundary sliding (GBS). GBS leads to the formation of cracks at grain boundary irregularities or at the triple joint of neighbouring grains [208] due to stress concentration. It has also been shown that [209] GBS can occur at room temperature in AZ31B magnesium alloy. In fatigue tests, cracks usually initiate at early stages from slip bands, but they are trapped when they reach grain boundaries [210]. The presence of cracks at a grain boundary accelerates the propagation of the above-mentioned cracks. It was shown that in strain control fatigue test on AZ31B at high strain amplitude, with the first reversal going from virgin condition to compression, which is similar to the loading step of the cold expansion process, some cracks developed at the grain boundaries and triple points [211].

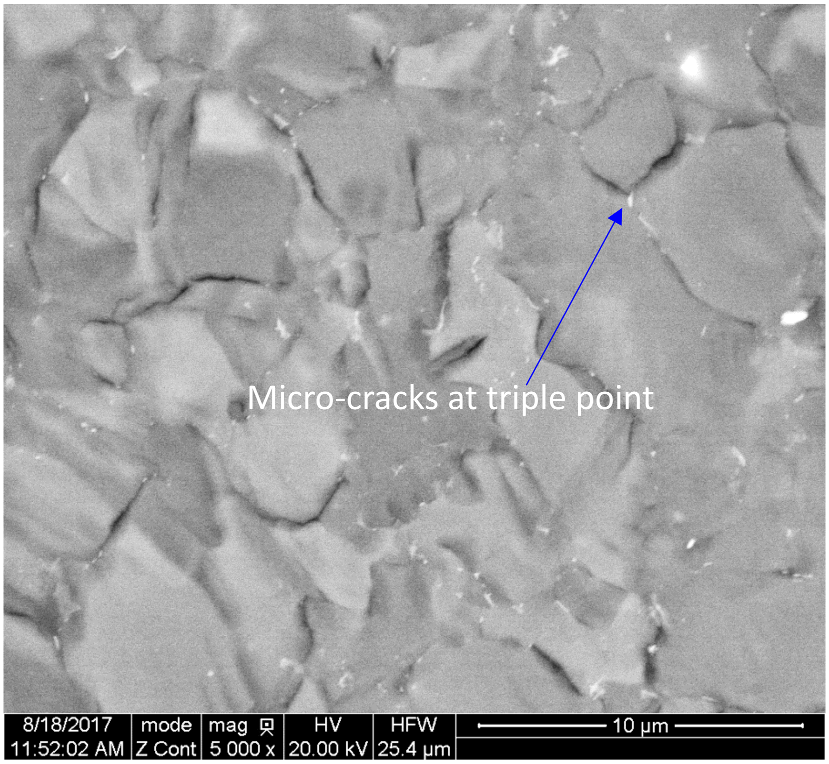

Figure 49. Micro-cracks developed at triple points

To summarize, the optimum percentage of cold expansion in this case is 5%. At 6% DCE, some micro-cracks were observed and seem to be responsible for the comparatively lower fatigue of 6% DCE.

3.2.4.2 Effect of different cold expansion percentages on material properties

During cold expansion, radial displacement is applied to the notch in such a way that the work piece is plastically deformed locally around the notch. As one of the most important representatives of mechanical properties, hardness, which measures the resistance of the material to plastic deformation caused by indentation, were done on double cold expanded sample with 2,4,5,6 (nominal) percentages. To do so, hardness was assessed using "Vickers hardness tester - Wilson hardness 402 MDV" machine with the indentation load of 50 gr. Results are shown in Figure 50.

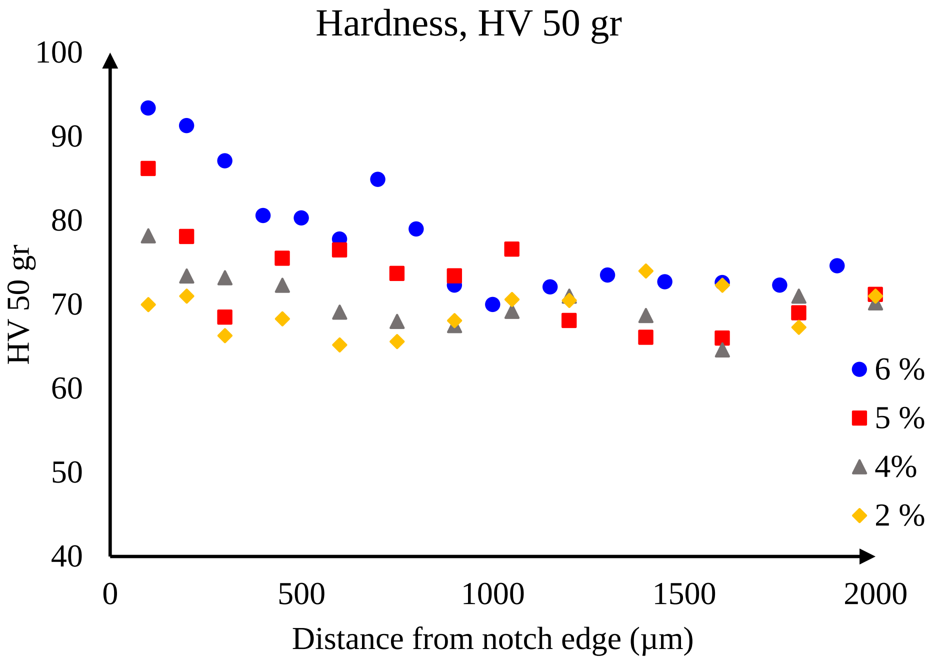

Figure 50. 50 gr Vickers hardness of double cold expanded sample

Figure 51 shows the plastic zone around the notch after 6% double cold expansion, which is the cause of the observed increase in hardness. It also shows the bulging around the notch.

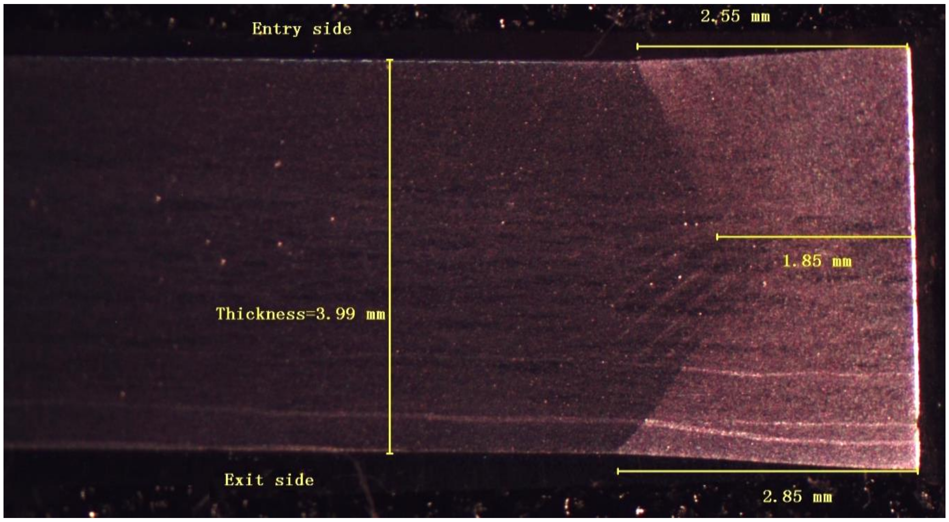

Figure 51. Plastic zone of 6% DCE

Figure 50 shows that hardness is significantly greater around the notch than the base metal (i.e., the un-affected zone). As expected, this difference increases for higher degrees of expansion. Hardness is a function of grain size and dislocation density and it has been shown that the hardness of magnesium alloys follow the well-known Hall-Petch relation between grain size and hardness [212]. Additonally, severe plastic deformation can move and pile up dislocations around grain boundary, causing dislocation tangles which impede further plastic deformation and increase hardness. Also, in the case of this study, the applied plastic deformation was causing profound twinning (Figure 47-48), which can be the other reason for increased hardness, providng adittional twin boundaries for dislocations to interact with [213]. The area that is higher harder than bare material is bigger for 6% DCE, while for 2% there is no meaningful increase in hardness. Despite the fact that the cold expansion process is done at room temperature, grain refinement may occur due to severe plastic deformation [214].

As shown in Figure 47, there is profuse amount of twinning in the cold expanded sample. As already stated in Figure 4, twinning results in reorientation of the crystals, meaning that the C-axis of twinned crystals are twisted. Therefore, the texture of the cold expanded sample should be different from that of virgin material. To examine the effect of cold expansion on texture, comparative texture measurements are done using XRD. The results are shown in the following image (Figure 52).

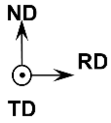

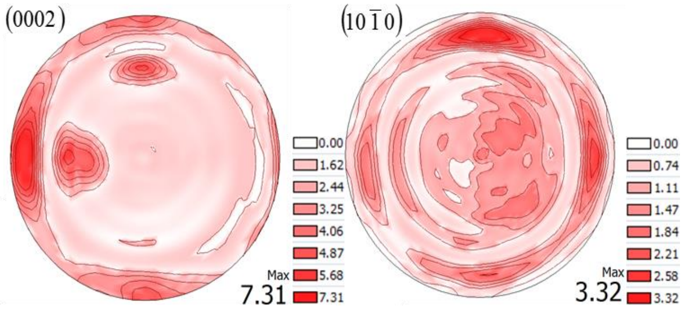

0.2 mm from notch

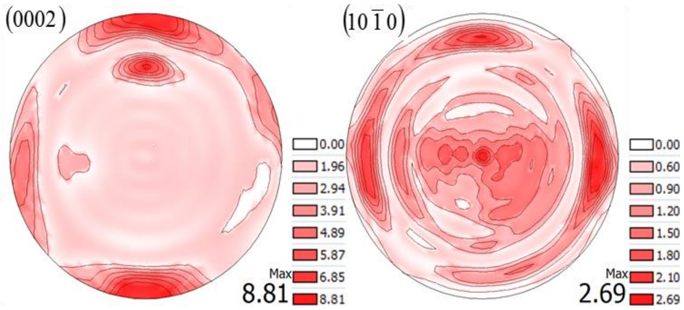

0.5 mm from notch

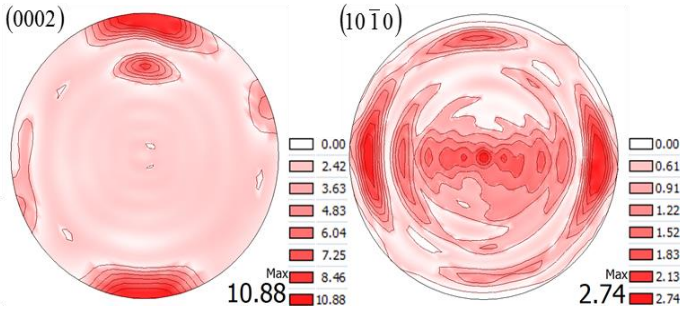

1.0 mm from notch

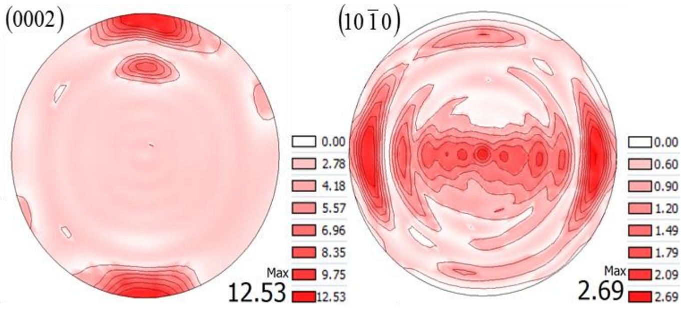

1.5 mm from notch

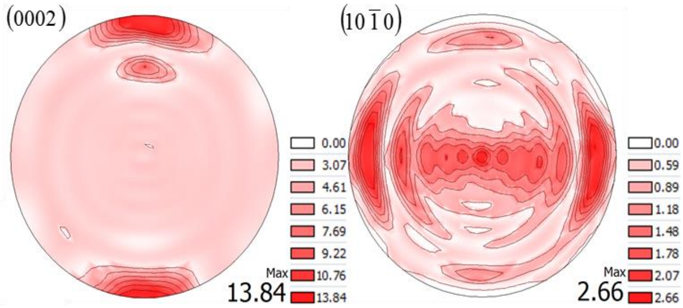

2.5 mm from notch

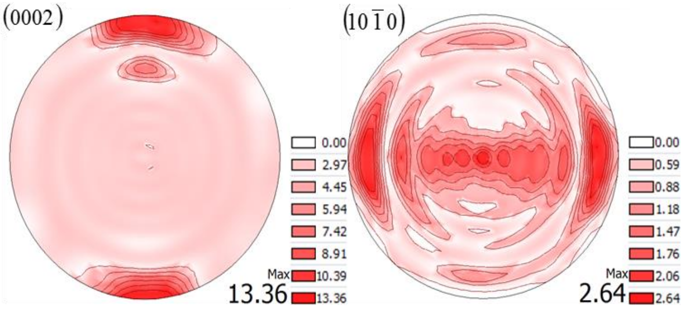

10 mm from notch

Figure 52. Texture of the 6% DCE sample at different locations

Far from notch, as expected, C-axis of the crystals are along the ND direction (i.e. typical rolling texture). Due to double cold expansion, many of the grains experience re-orientation, in such a way that the c-axis rotates towards the direction of the applied load. Therefore, close to notch, texture shows that many grains are rotated toward the RD. Getting far from notch, the intensity of rotated grain in RD decreases, which means lower number of grains are rotated. Far from notch, there is no change in texture of the specimen.

3.2.4.2 Effect of the optimum degree of cold expansion on fatigue life

To investigate the effect of cold expansion on fatigue life, three different configurations are tested: un-cold expanded (UCE), single cold expanded (SCE) and double cold expanded (DCE).

Test were done on a 3.18 mm sheet of AZ31B-H24. In order to find the optimum percentage for this material, similar procedures were followed. Four different cold expansion percentages were tested at same level of load. The stress at the notch root was chosen to be 170 MPa. The results presented henceforth are for 3.18 mm sheet.

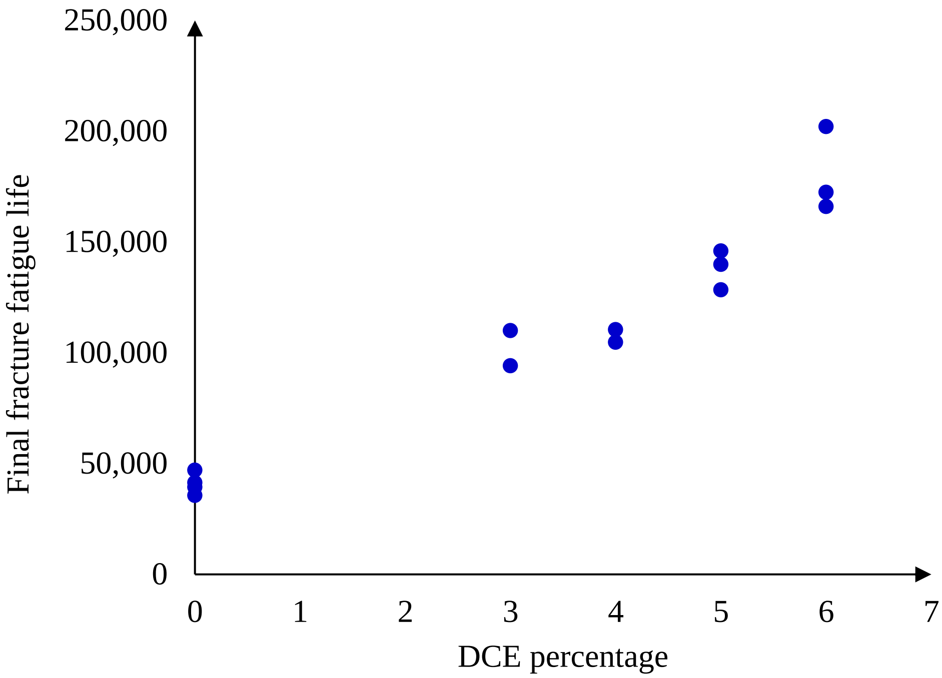

Figure 53. Fatigue life at different DCE%

Clearly increasing the percentage of cold expansion correspondingly improves fatigue life. According to the previous optimum percentage study, 2% cold expansion does not lead to any fatigue life improvement (Figure 43); therefore, in this new study of the optimum percentage, the minimum value of cold expansion was chosen to be 3%. Because 6% is the highest possible cold expansion percentage for split sleeve configuration [17] and higher percentage is not feasible, 6% is chosen as the optimum cold expansion of this sheet. Residual stress measurement by XRD are shown in following tables (Table *10*Table *11*). Measurements are done on three lines, as shown in Figure 34. Position of the points for XRD measurements, to make sure they are repeatable.

Table 10. Residual hoop stress on 6% DCE, entry side of first pass

	Hoop stress (MPa)					
R (mm)	Line 1	Error	Line 2	Error	Line 3	Error
0.2	-33.3	6.1	-29	6.1	-26.2	7.6
0.5	-40.7	6.4	-40	2.4	-38.6	3.3

2	-40.5	2.7	-37	1.7	-37.4	1.8
3	-38	1.8	-16	1.3	-15.7	1.4
4.5	-14.7	1.3	0.1	1.3	0.4	1.3

Table 11. Residual hoop stress on 6% DCE, exit side of the first pass

	Hoop stress (MPa)					
R (mm)	Line 1	Error	Line 2	Error	Line 3	Error
0.2	-43.5	4	-40.7	3.3	-47.6	3.9
0.5	-45.8	2	-39.9	2.1	-49.4	2.1
2	-52.9	1.7	-49.4	1.7	-50.2	1.8
3	-23.2	1.4	-27.9	1.4	-30	1.4
4.5	-6.7	1.2	-10.7	1.2	-6.6	1.2

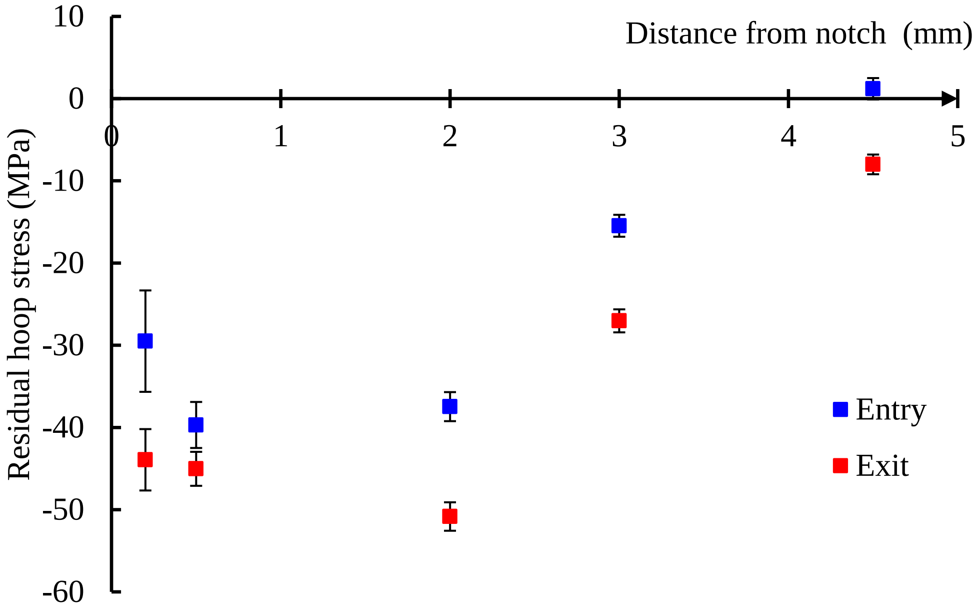

Figure 54. Residual Hoop stress, 6% DCE

As mentioned in section 2.2.3, one of the most important aspects of cold expansion is postponing the crack initiation and reducing the crack growth rate. To determining the crack initiation life, optical imaging was employed. The area around the notch was painted white to provide better contrast between the specimen surface and the developed fatigue crack. To make sure that the pictures were taken at maximum tensile load so the crack is fully open, a specific script in the DIC software was used, in which by taking the force feedback from the MTS controller as reference, pictures are taken at specified time stamp and force value. To measure the crack growth rate, the flat area around notch is painted with black speckles; therefore, the crack distance between crack tips can be mapped to the speckled area, where the software can calculate the (Figure 55. Measuring crack length using DIC software

All fatigue tests were fully reversed (R ratio of -1), and the frequency of tests was 10 Hz, except for the highest stress level, in which test were done by 2 Hz, because of the higher value of the applied load. The stress values in the S-N curve below is based on elastic formulation for stress concentration (19). In compression, higher stress levels cause the material to pass the yield limit. However, to avoid the significant complexity of calculating the true stress at notch root for the asymmetric alloy, the curve is shown for elastic stress at notch root.

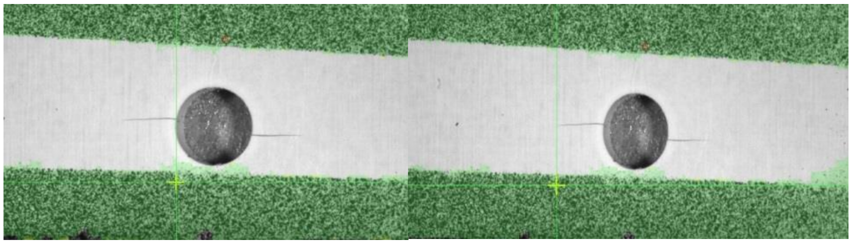

Figure 55. Measuring crack length using DIC software

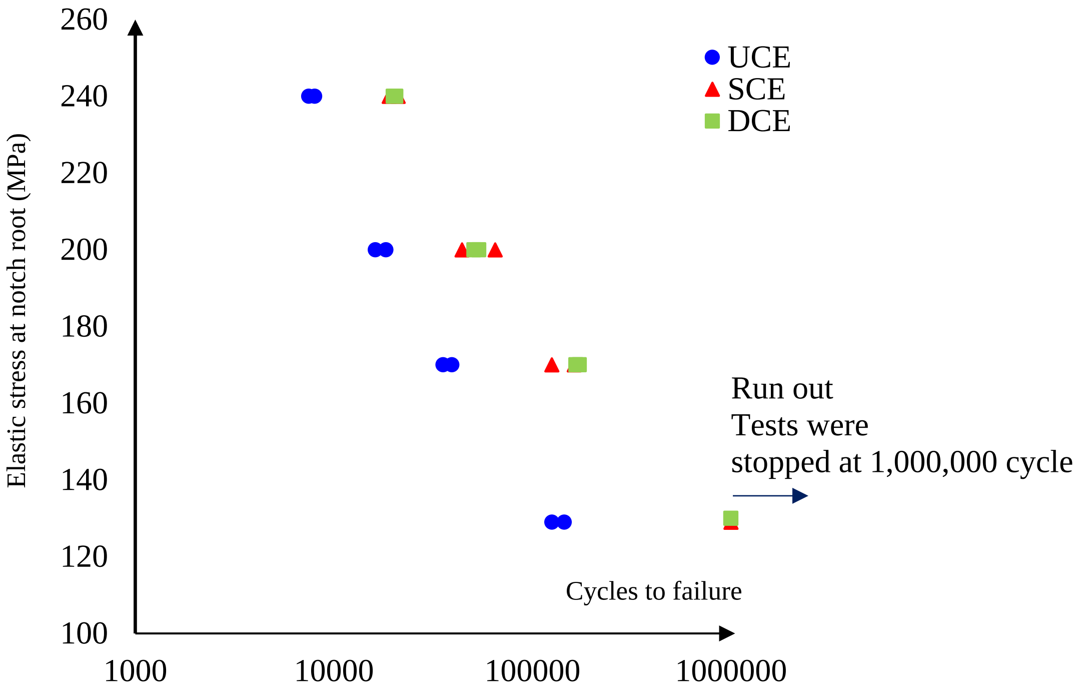

Figure 56. Stress-life curve, UCE vs SCE vs DCE

Cold expansion clearly improves the fatigue life. This improvement is more significant in the high cycle regime (i.e. lower stress amp), which can be related to residual stress relaxation phenomenon. It is worth mentioning that the test at 130 MPa stress level on SCE and DCE specimen were stopped after one million cycle, which is considered as the run-out limit for this study. No cracks were initiated in these samples.

In this research, the term crack initiation is defined as the cycle during which crack reaches the surface and propagates to a reasonably small length, e.g., 160 μm. According to images taken by DIC, in all cold expanded samples, the crack becomes visible at the entry site. Table 12 shows that both crack initiation and propagation life are increased by cold expansion. As expected, improvement in both initiation and propagation is amplified in the high cycle regime.

Comparing the crack initiation life of SCE and DCE gives an estimate of the order of magnitude of residual stress due to cold expansion. For example, the initiation life of the DCE sample at 240 MPa is close to the life of the UCE sample at 200 MPa, which suggests that the order of magnitude of the hoop residual stress should be close to 40 MPa, which is in agreement with the experimental measurements by XRD (Figure 54). In low cycle fatigue, single and double cold expansion yield similar results. The difference between these two conditions is magnified in the high cycle regime (Figure 56).

Table 12. Crack initiation/propagation life, UCE vs SCE, vs DCE

Stress (MPa)	**Condition**	**Crack initiation**	**Crack propagation life**	**total life**
240	UCE	3000	4488	7488
240	SCE	7600	11423	19023
240	DCE	9000	11553	20553
200	UCE	9200	9116	18316
200	SCE	37400	27602	65002
200	DCE	30800	20065	50865
170	UCE	30000	11357	41357
170	SCE	80000	45363	125363
170	DCE	126000	46390	172390
130	UCE	111000	33992	144992
130	SCE	No crack	NA	Run out

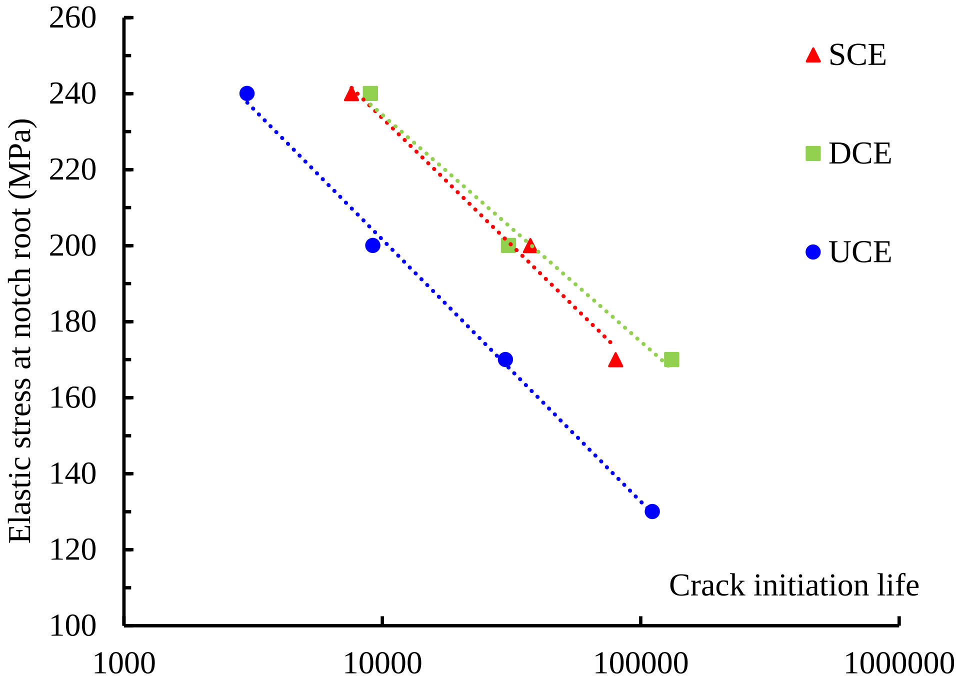

Figure 57. Crack initiation life of UCE vs SCE (6%) vs DCE (6% initial)

The fact that crack propagation life has increased means the crack growth rate should differ between cold expanded samples and un-cold expanded. Crack length were measured using the technique described above (Figure 55. Measuring crack length using DIC software). Since at stress level of 200 MPa and 240 MPa, the fatigue life of DCE and SCE samples are close, in the crack growth curves below, the comparison is made only for DCE sample versus UCE.

Here the term “crack length” refers to the average length of a crack at the right and left hand side of the notch on the entry side. At the beginning of crack initiation, the rate of crack propagation is meaningfully lower in double cold expanded samples than in un-cold expanded. Once reaching to the end of the compressive residual stress zone, the crack propagates at the same rate in both un-cold expanded and double cold expanded.

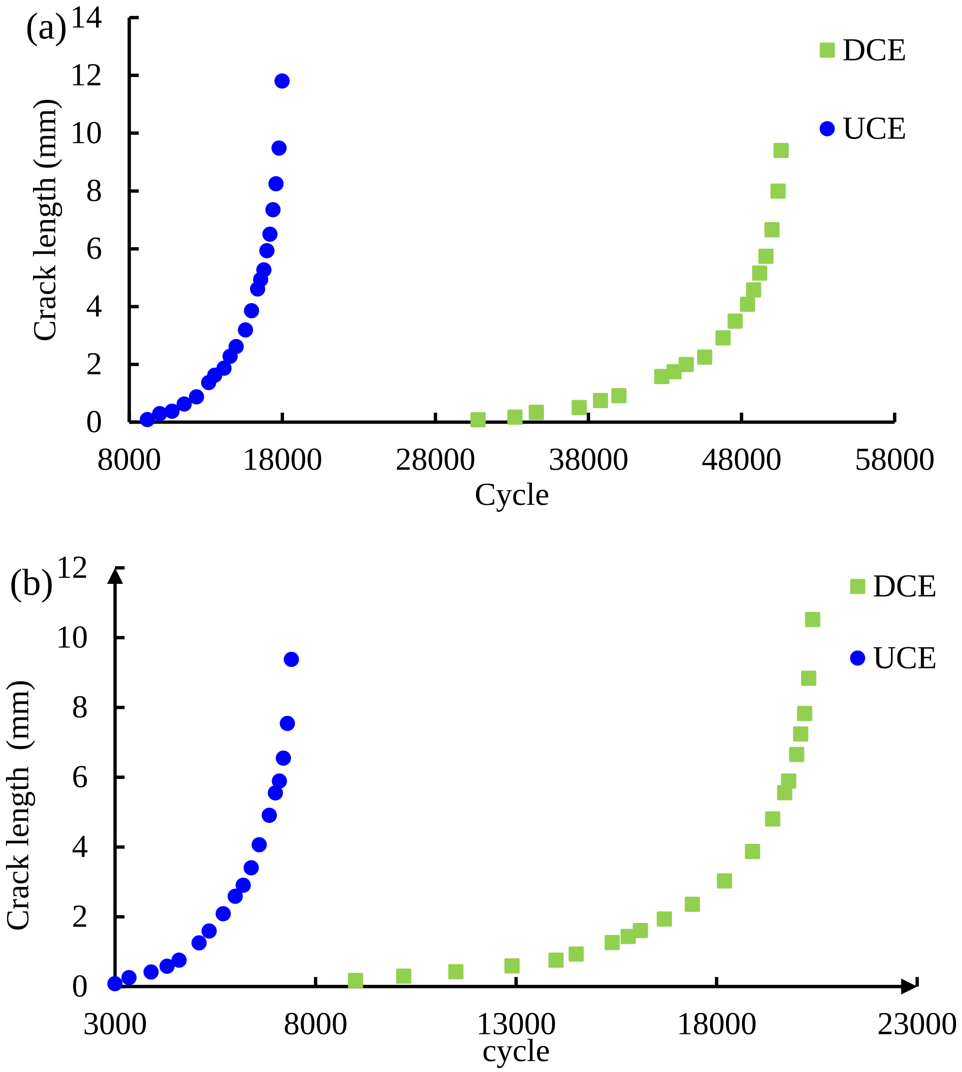

Figure 58. Crack length vs cycle, for samples tested at, a) 200 MPa at notch root, b) 240 MPa at notch root

The graph shows that not only crack initiation is postponed, the early crack growth rate is also decreased.

To have a better comparison, crack growth rate (mm/cycle) for these two condition is shown below.

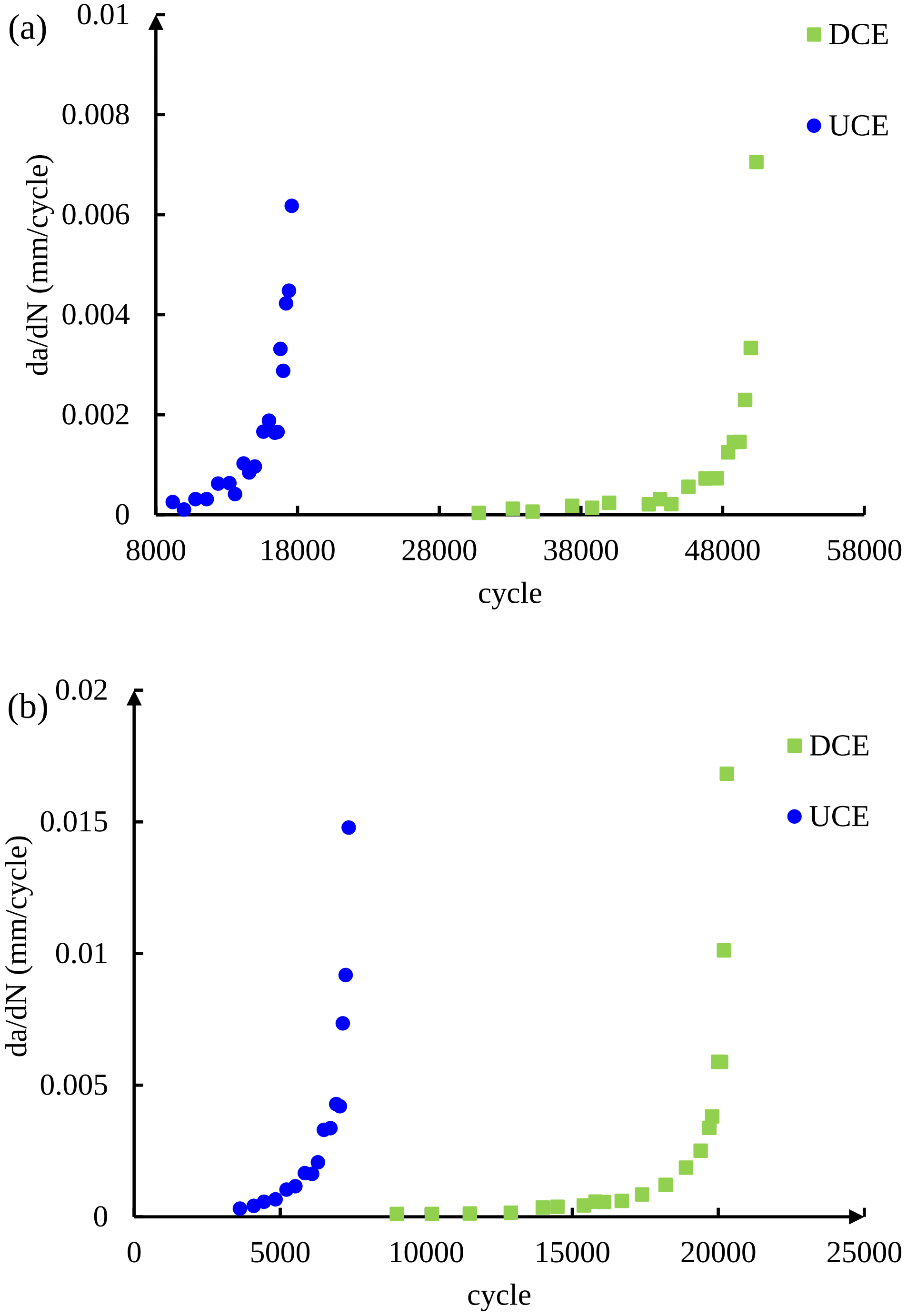

Figure 59. Crack growth rate vs cycle, for samples tested at, a) 200 MPa at notch root, b) 240 MPa at notch root

According to the Paris law equation [215], crack growth is also a function of crack length. In fact, the crack growth rate is function of the stress intensity factor.

$$\frac{da}{dN} = \mathrm{c}\Delta k^{m} \tag{20}$$

in which, a, k, c, m are crack length, stress intensity factor, and material constants, respectively. In a more general form, k is a function of square root of crack length.

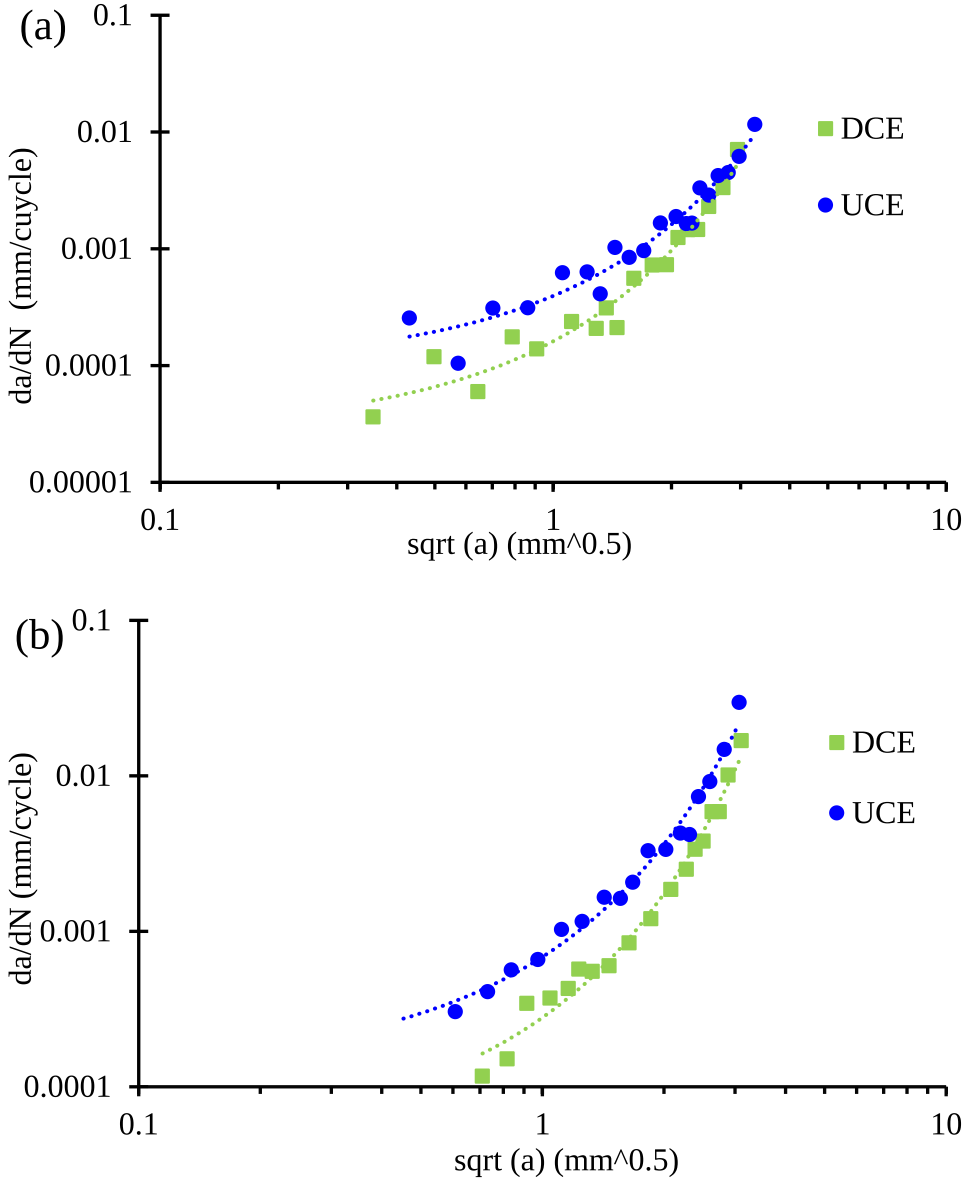

Figure 60. Crack growth rate vs square root of crack length, for samples tested at, a) 200 MPa at notch root, b) 240 MPa at notch root

As mentioned, the DIC cameras monitor the surface of the specimen during the test, therefore the reported crack is the length of crack on the surface (entry surface for cold expanded samples). To study the difference in crack growth rate near the notch, the fatigue crack striation patterns of the un-cold expanded and single cold expanded samples tested at 240 MPa sample were compared. Since both the fatigue life and fracture surfaces of single and double cold expanded samples shows little difference, the double cold expanded sample can be expected to have similar crack striation patterns. Therefore only the single cold expanded sample was investigated here.

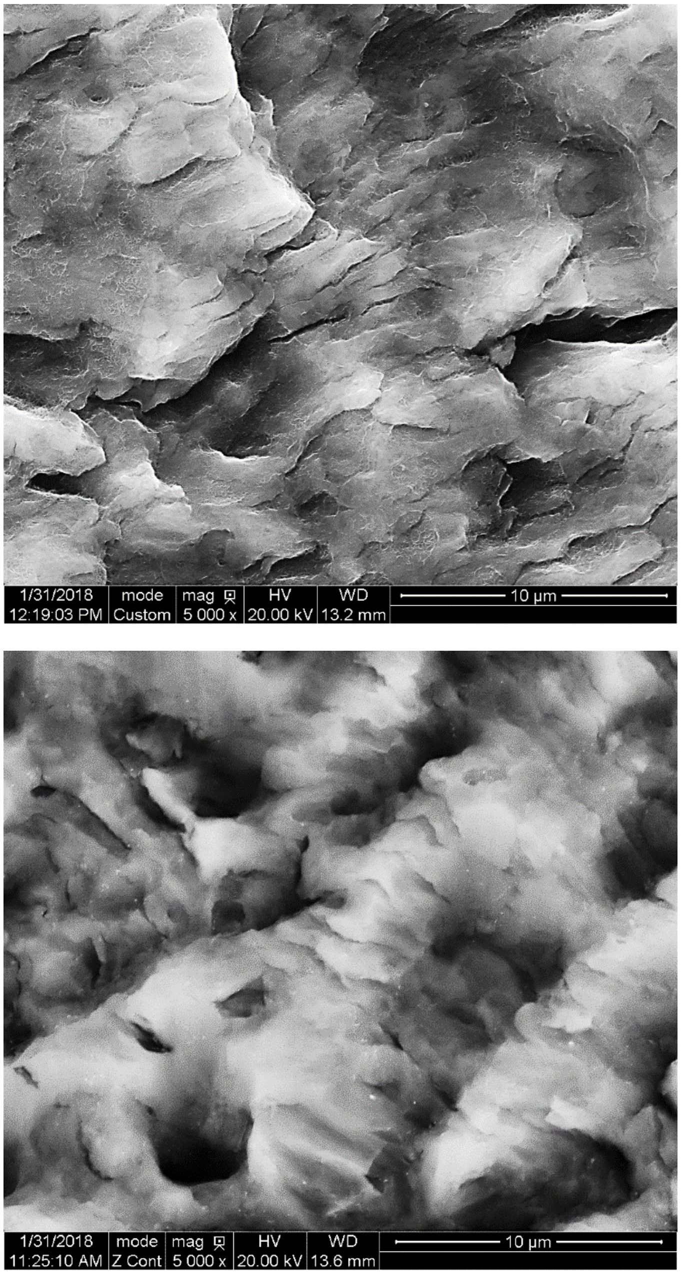

Figure 61. Fatigue crack striation pattern of SCE sample (top) and UCE (bottom)

The average space between striations in the single cold expanded sample is $\sim 0.88\ \mu m$, while in the as-received notch this value is $\sim 1.30\ \mu m$. Taking into account standard deviation, they are statistically different (95% CI).

3.2.4.4 Fracture surface of fatigue tested sample

The final fracture surfaces of the fatigue-tested specimens were observed using a scanning electron microscope. The fracture surface of the specimen tested at 170 MPa (at the notch root) is shown below.

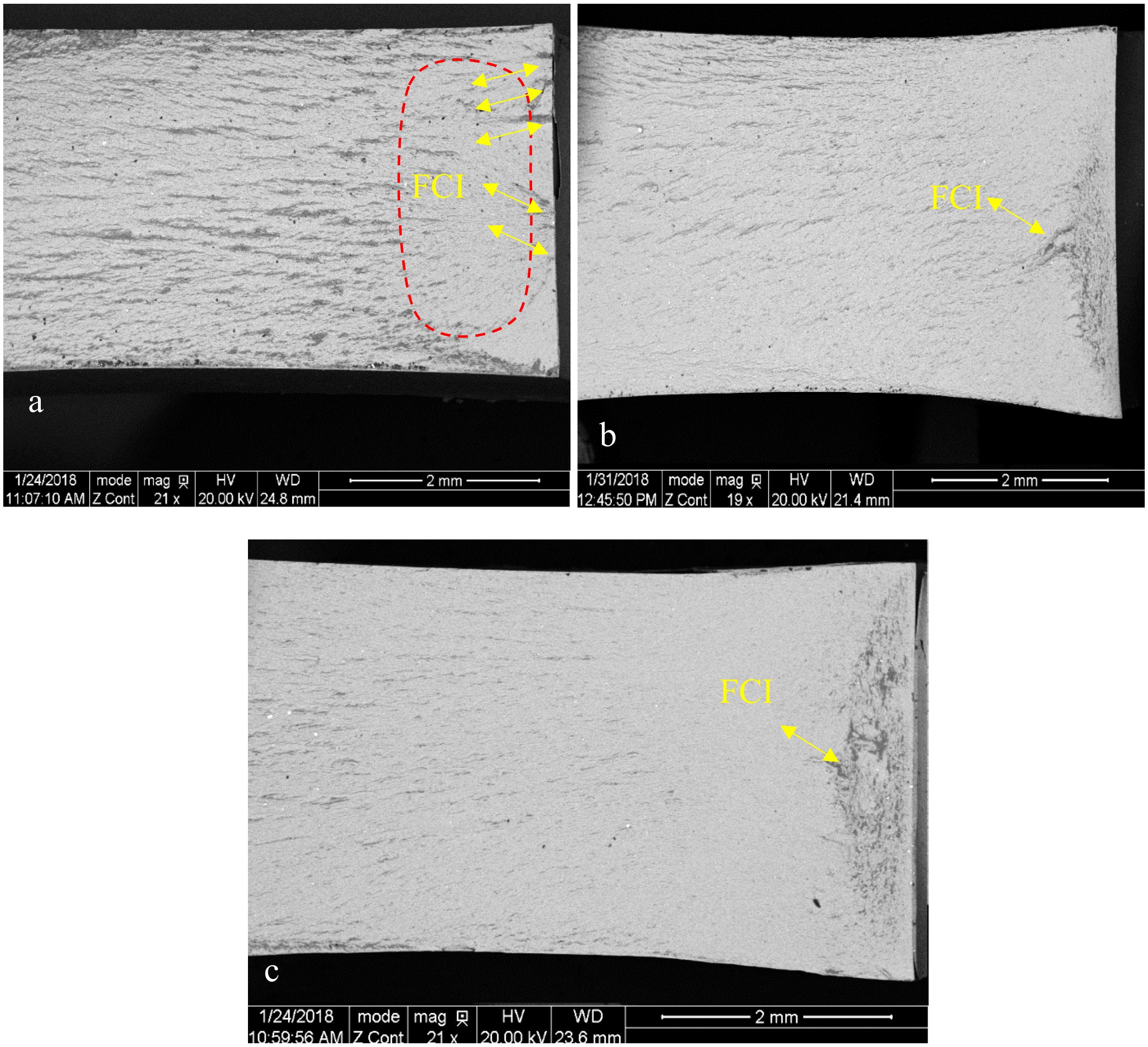

Figure 62. Fracture surface of 170 MPa fatigue tested sample, a) UCE, b) SCE, c) DCE

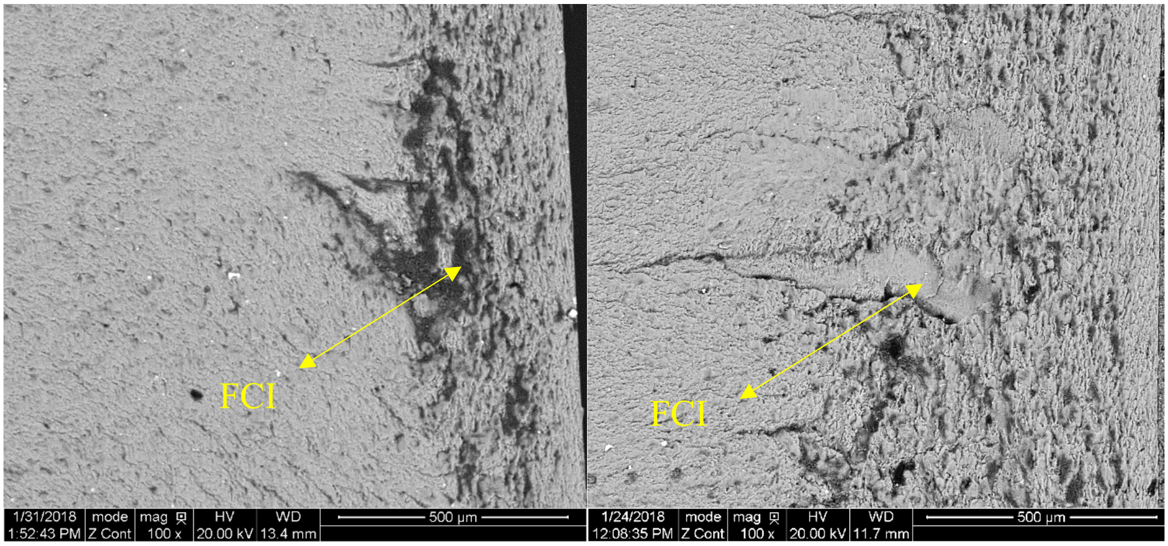

Figure 63. Crack initiation position on 170 MPa fracture surface, SCE (left) vs DCE (right)

As expected, in the as-received sample, the primary crack initiation position is right at n the notch edge. In addition, multiple crack initiation sites are visible, which can be attributed to the high stress level. On the other hand, in the cold expanded samples, crack initiates in the sub-surface. The red zone in Figure 62 shows the region in which crack growth rate is slow and as a result, the crack growth zone has a smooth surface. This area on SCE and DCE samples are not very clear, but the crack growth zone in SCE and DCE compared with UCE sample emphasize that this zone in in SCE and DCE has a smoother surface and means the crack growth rate is lower in SCE and DCE.

Using the scale bar in the SEM pictures, the fatigue crack initiation (FCI) position on the DCE sample is roughly 500 μm away from the notch, while for the SCE sample, the crack initiates at ~300 μm from notch, a difference that can be explained by the difference of the zone affected by plastic deformation. Comparing the distance of the FCI on DCE sample from notch with the hardness measurements (Figure 50), gives an idea of the possible reason. Up to 500μm, the hardness is greater in 6% DCE, which means up to this distance, dislocation density is changed. In other words, it seems due to radial plastic deformation during cold expansion process, existing dislocations around notch are pushed and piled up at certain point. This point is the perfect location for a crack to initiate [216]. Although far from notch effective stress is lower, but this dislocations can help the crack to initiate there. Residual hoop stress leads to change of the effective stress around the notch. Between these two competing factors, seems the dislocations has a stronger effect, and causes the crack to initiate far from notch. The position of the crack initiation on the cold expanded sample with respect to the thickness of the sample is in agreement with the plastic deformation zone after cold expansion (Figure 51). This hypothesis needs a more comprehensive look at the effect of plastic deformation on the dislocation density as well as residual stress distribution.

In the DCE sample, close to the notch edge, the morphology of grains is evidently different from that in the as-received notch. Close to the notch in the cold expanded sample, grains look closer to each other and seem to be rotated toward the direction of mandrel movement.

For better understanding of the variation in the crack initiation behavior at different cold expansion percentages, the fracture surface of 3% DCE tested at 170 MPa is shown below.

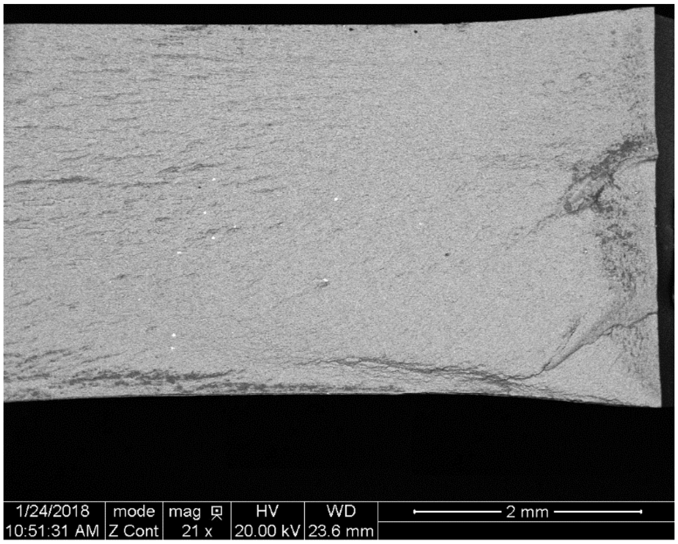

Figure 64. Fracture surface of 3% DCE specimen tested at 170 MPa

Comparing Figure 64 with Figure 62 reveals the following points. First, in the 3% DCE sample, unlike the 6% DCE, the crack initiates at the notch edge, as in the as-received sample. It seems in 3% DCE sample, the applied plastic deformation was not enough to change the dislocation density of the material, therefore the aforementioned hypothesis about the effect of piled up dislocations cannot be incorporated here. On the other hand, the created residual stress reduces the effective stress at notch root. Therefore, in the as-received sample there are multiple crack initiations, in 3% DCE, there are only two initiation sites.

All the above SEM photos were for samples tested at 170 MPa. In order to compare crack initiation modes in low cycle and high cycle fatigue, the fracture surfaces of samples tested at 240 MPa are presented below.

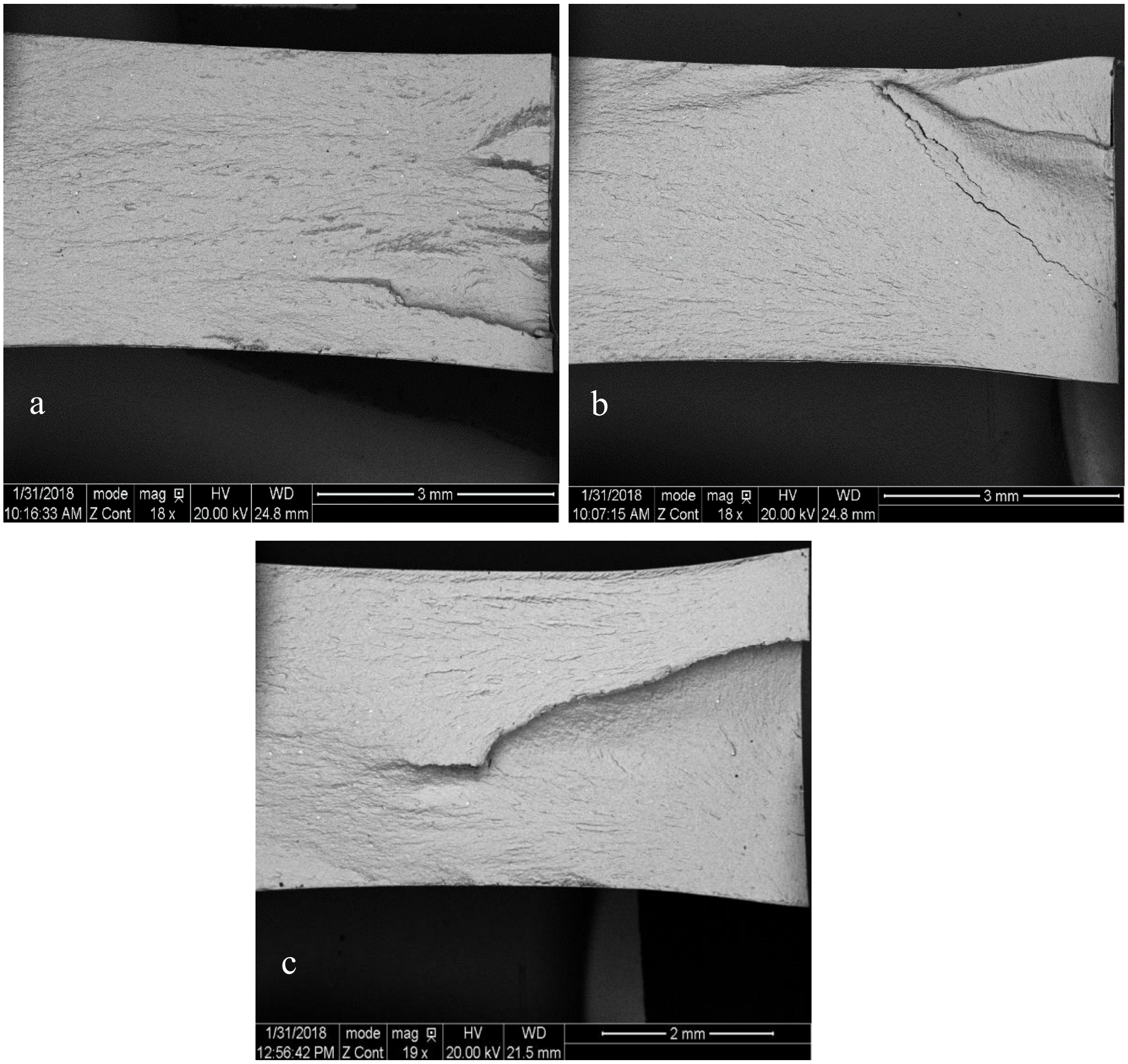

Figure 65. Fracture surface of 240 MPa fatigue tested sample, from top to bottom: UCE, SCE, DCE

The fracture surfaces of samples tested at high load level of 240 MPa, exhibit no significant difference between SCE and DCE, which is in perfect agreement with the fatigue test results. By comparing the fracture surface of as-received samples at 170 MPa and 240 MPa, it can be seen that there are more crack initiation sites at 240 MPa. Further, as expected, the stable crack growth zone (red region in Figure 62) is larger for the sample tested at 170MPa

3.3 Summary

This chapter has introduced the experimental work of this research, including the cold expansion process and corresponding radial displacement, residual stress, texture, hardness measurements, as well as the effect of cold expansion on fatigue life and crack initiation and propagation. It was shown that cold expansion on AZ31B magnesium alloy, results in significant fatigue life improvement factor, by both retarding crack initiation and decreasing the crack growth rate. Due to the plastic deformation, texture of the material close to notch changes in such a way that c-axis of grains are rotated toward the direction of loading.

Chapter 4. Modeling

To model the cold expansion process on a magnesium sheet, two methods were utilized here, VMP and finite element (ABAQUS).

4.1 VMP

4.1.1 Basic equations and assumptions

For modeling the process using VMP, the basic relations are the same as those presented in section 2.3.1 . In the original VMP formulation, natural boundary conditions, inside and outside pressure, were employed for the elastic-plastic solution of a cylinder. However, for cold expansion a mixed essential and natural is in place. The boundary conditions are the known radial displacement at the inner radius and zero pressure at the outer radius. In other words, after discretizing the problem into small circular annuli surrounding the hole, and assembling the stiffness matrix $\{k\}$; in the load-displacement equation $\{k\}\{u\} = \{p\}$ one of the knowns is in the $\{p\}$ (load matrix) and the other one is in the $\{u\}$(displacement matrix). This is a nonhomogeneous boundary condition. To solve a nonhomogeneous boundary value problem, the method described by Hutton [217], in which the known rows in the $\{u\}$ are eliminated by converting them to the known value added to $\{p\}$ is implemented here. The cold expansion problem is modeled as plane stress problem since the top and bottom surfaces of the sheet are traction free.

In a thick-walled cylinder subjected to pressure, in the case of plane stress, according to the well-known Lame's solution:

$$\begin{bmatrix} c_{11} & c_{12} \\ c_{21} & c_{22} \end{bmatrix}^{-1} \begin{bmatrix} u_1 \\ u_2 \end{bmatrix} = \begin{bmatrix} p_1 \\ p_2 \end{bmatrix} \tag{21}$$

The stiffness matrix is the inverse of the following compliance (c matrix).

$$
\begin{aligned}
c_{11} &= \frac{1+v_{eff}}{E_{eff}} \frac{r_1^3}{r_2^2 - r_1^2}_j \left(\frac{1-v_{eff}}{1+v_{eff}} + \frac{r_2^2}{r_1^2} \right) \\
c_{12} &= \frac{-2}{E_{eff}} \frac{r_1 r_2^2}{r_2^2 - r_1^2}_j \\
c_{21} &= \frac{2}{E_{eff}} \frac{r_1 r_2^2}{r_2^2 - r_1^2}_j \\
c_{22} &= -\frac{1+v_{eff}}{E_{eff}} \frac{r_2^3}{r_2^2 - r_1^2}_j \left(\frac{1-v_{eff}}{1+v_{eff}} + \frac{r_1^2}{r_2^2} \right)
\end{aligned}
\tag{22}
$$

For each element, radial and tangential stress can be obtained by:

$$
\begin{aligned}
\sigma_\theta &= \frac{p_1 r_1^2 - p_2 r_2^2}{r_2^2 - r_1^2} + \frac{(p_1 - p_2) r_2^2 r_1^2}{(r_2^2 - r_1^2) r^2} \\
\sigma_r &= \frac{p_1 r_1^2 - p_2 r_2^2}{r_2^2 - r_1^2} - \frac{(p_1 - p_2) r_2^2 r_1^2}{(r_2^2 - r_1^2) r^2}
\end{aligned}
\tag{23}
$$

In which p_1, p_2, r_1, r_2, r are,respectively, inner pressure, outer pressure, inner radius, outer radius, and radius of the point of interest.

The solution procedure can be summarized as follows:

- Discretize the sheet into co-centric circular strips surrounding the hole.
- Form elemental stiffness matrix using equations (22).
- Assemble the stiffness matrix assuming all strips are in the elastic regime and generate the system of linear equations:$\{K\}\{U\} = \{P\}$.
- Apply the mixed boundary condition based on the level of cold expansion
- Solve for $\{U\}$ to obtain the distribution of displacement around the hole
- Calculate p_1, p_2 for each strip using equation (22).

- Calculate radial and hoop stresses using equation (23) and calculate equivalent stress using Cazacu-Barlat yield criteria [218].
- Determine how many strips have passed the elastic limit by comparing equivalent stress to the yield strength of the material.
- Using the projection method by employing to Update values of E_{eff}, v_{eff} for strips that have passed the yield stress by using experimentally obtained stress-strain curve and equivalent stress.
- Repeat above steps until equivalent stress and strains provided by solution converges to the uniaxial stress-strain curve.

4.1.2 Loading

To model the cold expansion process in AZ31B magnesium alloy, two major difference should be considered. First, the von Mises yield surface and therefore the equivalent stress can not address of asymmetric behavior. Secondly, there are two different experimental curves, one for uniaxial tension and another for compression, therefore for the projection method this characteristic should also be considered.

The Cazacu-Barlat asymmetric yield criteria [198] is capable of considering asymmetric behavior. The equivalent stress defined by this criteria is as follows:

$$\sigma_{eq} = A\left(J_2^{\frac{3}{2}} - cJ_3 \right)^{\frac{1}{3}} \tag{24}$$

J_2, J_3 are the second and third invariants of deviatoric stress tensor.

$$c = \frac{3\sqrt{3}}{2}\left(\frac{\sigma_{yt}^3 - \sigma_{yc}^3}{\sigma_{yt}^3 + \sigma_{yc}^3}\right)$$

$$A = 3\left(3^{\frac{3}{2}} - 2c\right)^{\frac{-1}{3}} \tag{25}$$

where σ_{yt}, σ_{yc} are tensile and compressive yield strengths respectively. In the case of symmetric material (i.e., $\sigma_{yt}^3 = \sigma_{yc}^3$) the Cazacu-Barlat yield criteria is the same as von Mises. Figure 66 shows the yield surface for different ratios of tensile and compressive yield stress.

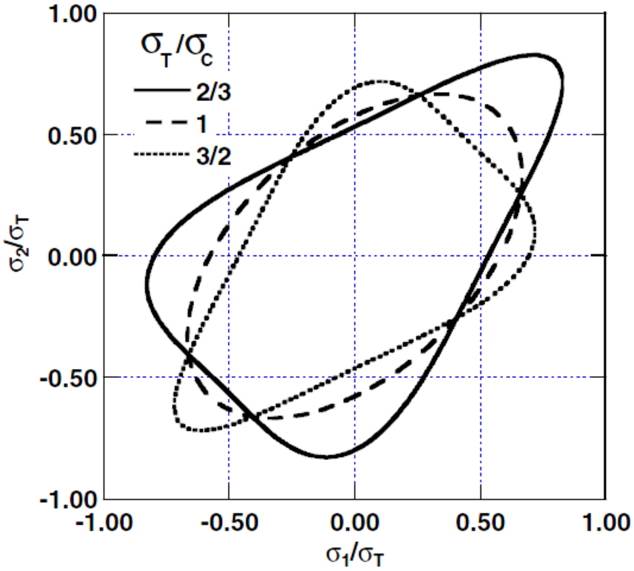

Figure 66. Comparison of Cazacu-Barlat yield surface for different ratio of tensile to compression yield [218]

For the post yield and evolution of yield surface, there are two possible way of considering the effect of asymmetry. First, the shape of yield surface assumed to be the same (constant value of c). In this case, the uniaxial compression curve obtained from experiment should be converted to equivalent stress and equivalent plastic strain according to:

$$\sigma_{eq} = -\left(\frac{3\sqrt{3}+2c}{3\sqrt{3}-2c}\right)^{\frac{1}{3}} \sigma_{11}$$

$$\varepsilon_{eq}^{p} = -\left(\frac{3\sqrt{3}+2c}{3\sqrt{3}-2c}\right)^{\frac{-1}{3}} \varepsilon_{1}^{p} \tag{26}$$

In fact, by this assumption, the equivalent initial yield strength for tension and compression will be the same. Whereas the equivalent plastic strain and equivalent stress for tension are the same as stress and plastic strain in a uniaxial tensile test, the equivalent stress and plastic strain for the compression curve are not the same as those for the uniaxial compression curve. The curve used in the projection method for updating the values of the Young's modulus and Poisson's ratio is the weighted average of tension and compression curve, according to the stress state of the element. (section 2.2.3.2) (Figure 67). In other words, each element has to follow a specific stress-strain curve according to its stress state, and this state and the consequent curve change for each iteration in the VMP process. This method was successfully implemented by Khayamian et al. [24].

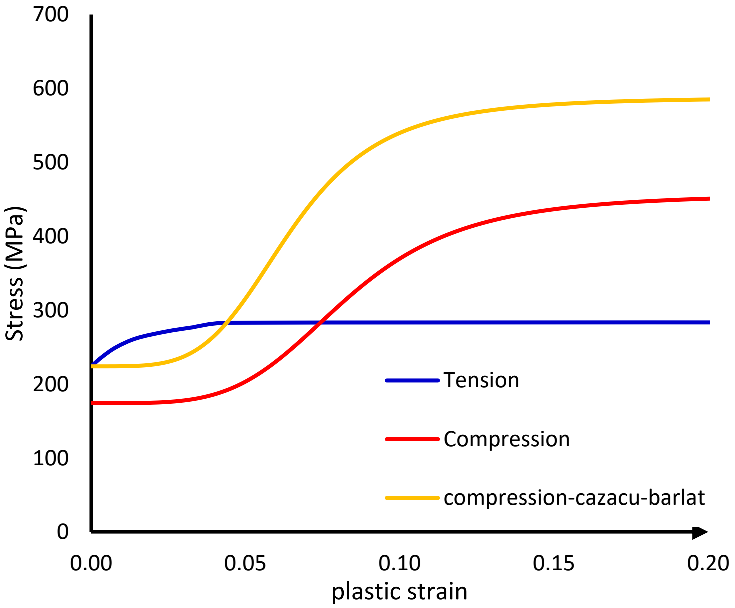

Figure 67. Tension-compression curves used in VMP

The other way of considering tension-compression asymmetry is to assume that the shape of the yield surface changes as the stress state of the element passes the yield limit and it goes into plastic regime, as shown in Figure 68. Evolution of Cazacu-Barlat yield surface for different values of plastic strain.

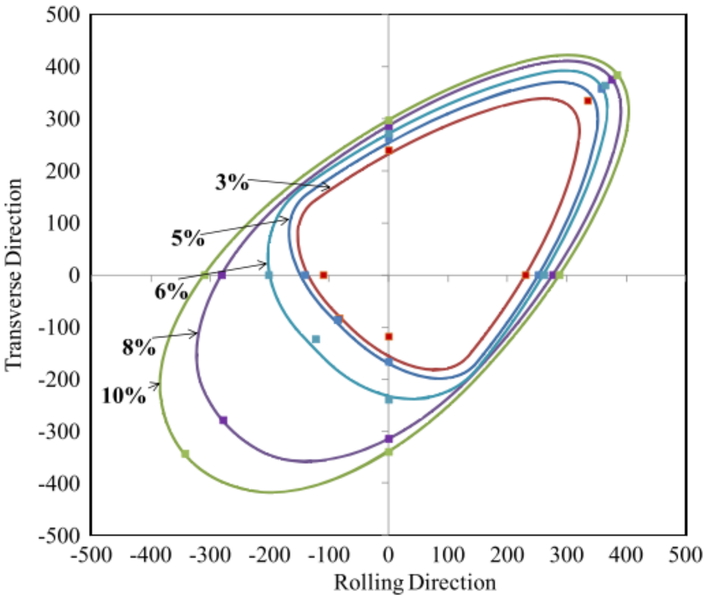

Figure 68. Evolution of Cazacu-Barlat yield surface for different values of plastic strain [219]

In this case, the equivalent stress curve is identical to that in tensile test. All elements follow the same stress-strain curve (the experimentally obtained tensile curve), which remains the same for all iterations. On the other hand, the shape of the yield surface (i.e., the formula used in calculating equivalent stress) changes for each element according to the plastic strain of the element in the previous iteration to take into account the effect of the compression curve.

Since the VMP is an iterative procedure, a convergence criterion is needed for finding the final solution. In fact, starting from the elastic solution, the VMP process updates the material properties in such a way that the final solution (i.e., the equivalent stress and strain of each element) is on the equivalent curve. Therefore, for the last iteration, the difference between values of equivalent stress found in that iteration and the aimed stress-strain curve was considered as a proper representative of the convergence criterion. Indeed, this difference is stored as a matrix with the number of rows equal to the number of elements the body was discretized into. Ideally, all elements of this matrix should be zero. Thus, the standard deviation of of the differences for all elements, which has the same unit of stress, divided by the yield strength (to make it unitless) was chosen as the convergence parameter. The iteration process was continued until this number reached a value of less than 10^{-4}.

4.1.3 Unloading

The unloading solution is similar to loading, but in this step each element has a specific behavior according to its plastic strain at the end of loading step. For the unloading step, a pressure with the same value as the pressure at the end of loading with opposite sign is applied to the hole. Negative pressure simulates the removal of mandrel.

For the unloading solution, since in the VMP solution tensile and compressive curves need to be determined, the tension-compression curve is considered as a tensile curve, and compression-tension is considered as the compression curve. Because the TC and CT curves are obtained for specific values of strain (Figure 19Figure 20), for the unloading portion, interpolation between the given strain levels was done. For example, if at the end of loading; one of the elements had a strain value of 7%, interpolation between the curves for 6% and 8 % was considered as the behavior for 7%.

A MATLAB code was developed to implemented the VMP procedure outlined above. The parameters used in this code are listed in Table 13.

The unloading solution is only presented here with the assumption of different shapes of yield function, method described earlier. To determine the reverse yields, tension-compression and compression-tension are moved to the origin, and 0.2% offset is used to calculate the yield.

Table 13. Parameters used in VMP code

Internal diameter (mm)	**External diameter (mm)**	**Number of elements**	**Young's modulus (MPa)**	**Poisons ratio**
6	50	200	45000	0.35

4.2 ABAQUS

The ABAQUS finite element software was used in this study to model the process with more detail.

Since, the VMP is able to model the process only in 2D, a 3D finite element model was implemented to gain a better understanding of the process.

4.2.1 Overview

In the finite element simulation, a mandrel goes down through the hole of the work piece and comes into contact with the split sleeve. The movement of the workpiece is limited by a support, which is in contact with the bottom of the work piece.

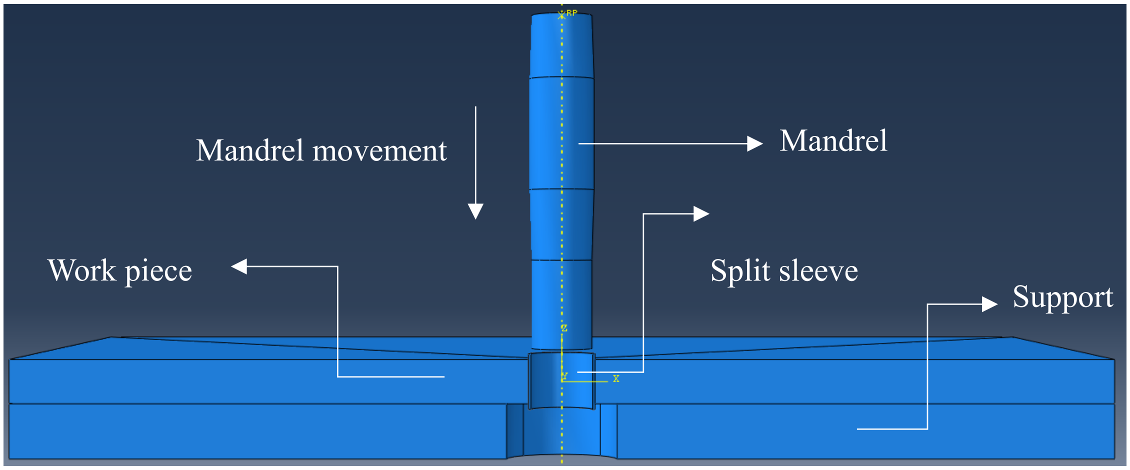

Figure 69. Overview of the finite element model

4.2.2 Parts

For the mandrel, a 3D rigid part was used to create the geometry. The maximum diameter was set to be 5.84, and the minimum diameter of the straight section of the mandrel was 5.46 mm, which was measured on the actual mandrel used in this study. The details of the geometry are presented in Figure 70. Geometry of the mandrel used in ABAQUS In all the following images, dimensions are in mm.

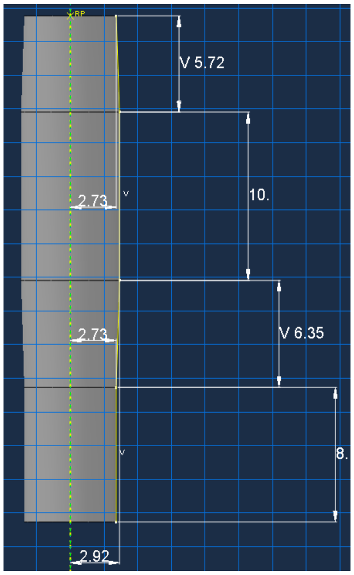

Figure 70. Geometry of the mandrel used in ABAQUS

Since the assembly is symmetrical, to reduce the computation time, only half of the work piece was modeled. To make it identical to the real conditions, a square with 100 mm side with a center hole of diameter 6 mm was modeled in the ABAQUS as the work piece. The thickness was set to be 4 mm.

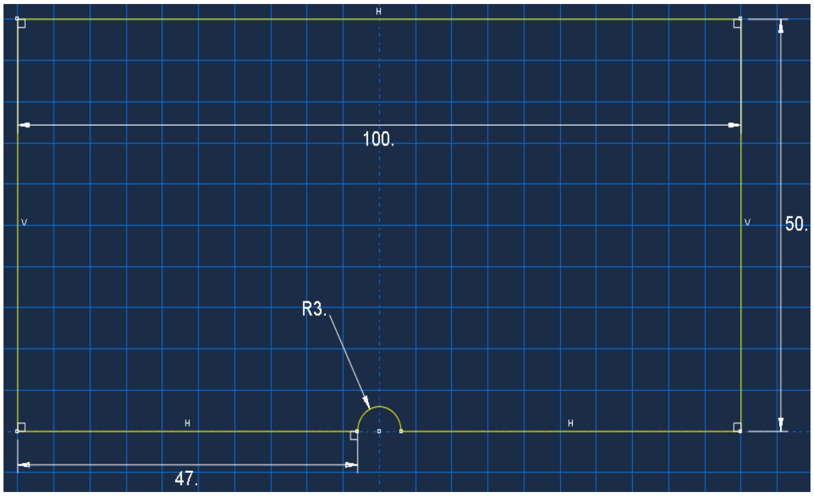

Figure 71. Geometry of the work piece in FEM

The split sleeve was modeled as a cylinder with thickness of 0.2 mm, with external diameter of 6 mm, to match the initial dimeter of the work piece. For the split, a fillet with 0.2 mm radius was used as a representation of the discontinuity of the split sleeve that allows expansion.

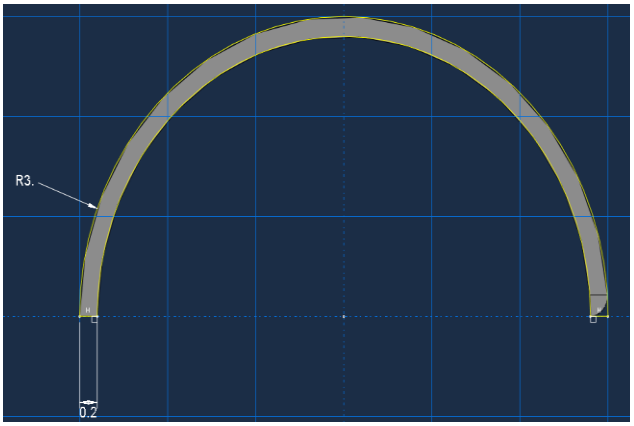

Figure 72. Geometry of the split sleeve in FEM

The only requirement for the sleeve length that was it should be more than the thickness of the workpiece. Therefore, in this FEM, the length of the split sleeve was adopted to be 5 mm.

The work piece support has the similar geometry as the work piece (Figure 71), with the only differences being that the diameter of its center hole was 10 mm and the thickness was 5mm.

4.2.3 Material properties of different parts

The mandrel, as mentioned, was considered to be rigid. For the split sleeve elastic behavior with the properties of steel was used. likewise, the support of the work piece will remain in the elastic regime, thus it was also considered to behave elastically like the split sleeve.

The Young’s modulus and Poison’s ratio were 200,000 MPa and 0.3, respectively.

As will be discussed later, according to the VMP solution, for the loading step, the dominant component of the stress is the radial stress, which is compressive. Since ABAQUS is capable of dealing with only one behavior, monotonic compression behavior of AZ31B (Figure 67) was used in ABAQUS. For simulating the unloading, since the given behavior for the loading is not bilinear, ABAQUS can only adopt isotropic hardening. ABAQUS needs the behavior to be true stress vs true strain, while the data obtained from experimental monotonic compression testing is engineering stress vs engineering strain. To convert those to true values, the following equations are used:

$$\sigma_{true} = \sigma_{engineering}(1 + \varepsilon_{engineering})$$

$$\varepsilon_{true} = ln(1 + \varepsilon_{engineering}) \tag{27}$$

$$\varepsilon_{plastic\ true} = \varepsilon_{true} - \frac{\sigma_{true}}{E}$$

Values of Young's modulus and Poison's ratio for the magnesium part are the same as the ones in Table 13.

4.2.4 Steps

Since there were two contacts (section 4.2.5) in the model, which were supposed to be active from the beginning of the solution, a contact step was added to the model, in which there was no external force or displacement. This step allows the finite element model to stablish the contact between parts, which makes it easier for the model to solve the contact problem in the main step, where the load is applied.

Due to the great amount of strain that the work piece undergoes during loading, nonlinear geometry was considered in the steps. Hence, there are a total of three steps in this model: initial (ABAQUS default), contact and load.

4.2.5 Contacts

As depicted in Figure 69, there are three different contacts in the current proposed model, Contact between the mandrel and the inner surface of the split sleeve, contact between the outer surface of the split sleeve and the workpiece and between the workpiece and the steel support. The first one was established at the load step, when the mandrel goes down and touches split sleeve, while two other contacts were established in the contact step.

To make the results of finite element model comparable with those of VMP, all these contacts are considered frictionless. Later in the case study section of the thesis, the effect of friction on residual stress distribution will be considered in the model. All contacts are surface to surface contact (standard model of ABAQUS).

4.2.6 Load-boundary condition

In the ABAQUS simulation, the main external stimulant was the mandrel movement. Since the mandrel is a rigid part, to apply the boundary condition, a reference point was created on it.

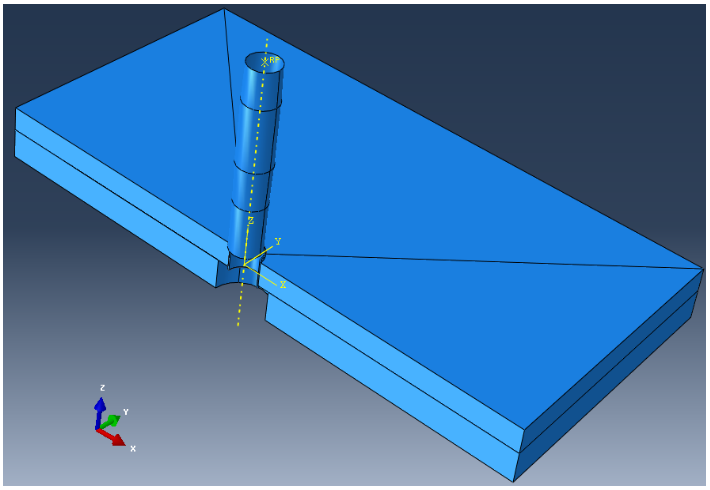

Figure 73. Assembly of the finite element model and the coordinate system

The possible movement of the mandrel in the x and y directions (Figure 73) and also the rotation in all three direction is restricted. In the loading step, the mandrel was set to move 40 mm in the negative direction of the z axis. A value of 40 mm was chosen so that the mandrel passed completely through the work piece so the unloading process was fully completed.

Only half of the work piece was modeled in half; therefore, a symmetric boundary condition (Y sym) is applied on this part, As in Figure 74a. To prevent the work piece from moving when the mandrel comes in contact with split sleeve and causing a lateral force on the work piece, the outer surfaces of the work piece were restricted from moving in the $x andy$ directions.

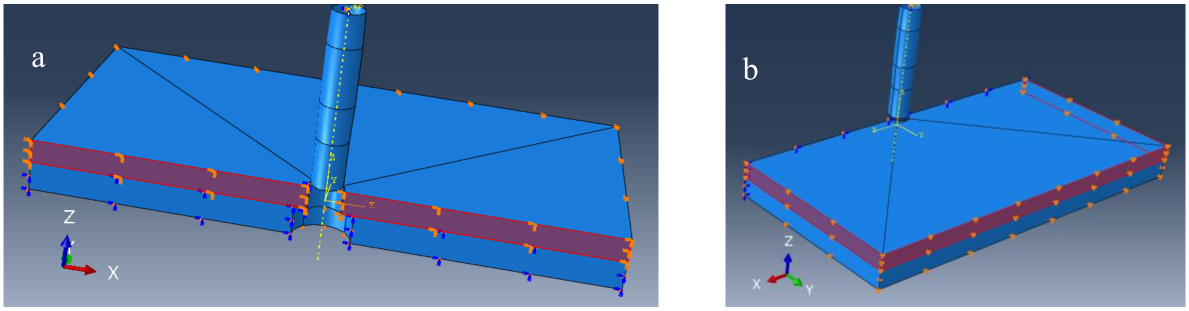

Figure 74. Boundary condition of work piece

In the real world, the split sleeve is held in place by a nose cap, which prevents it from moving in the direction of mandrel movement. Thus, in the FE model, the displacement of bottom surface of split sleeve is restrained. As in the work piece, owing to symmetry, only half of the split sleeve is modeled; therefore, the symmetry boundary condition was also applied on the split sleeve (Figure 75b).

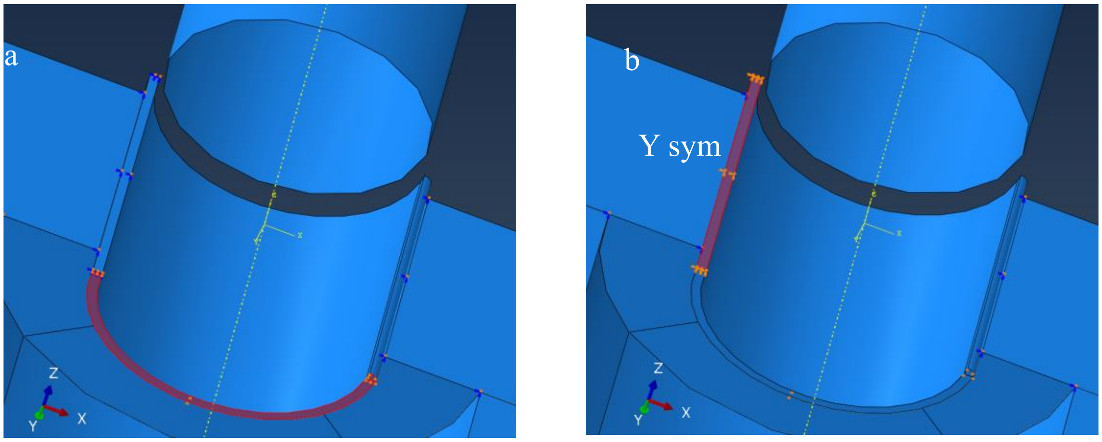

Figure 75. Boundary condition for split sleeve

For the steel support below the work piece, boundary conditions are similar to those for the work piece, but with additional condition, which is the prevention of the steel support moving in the z direction.

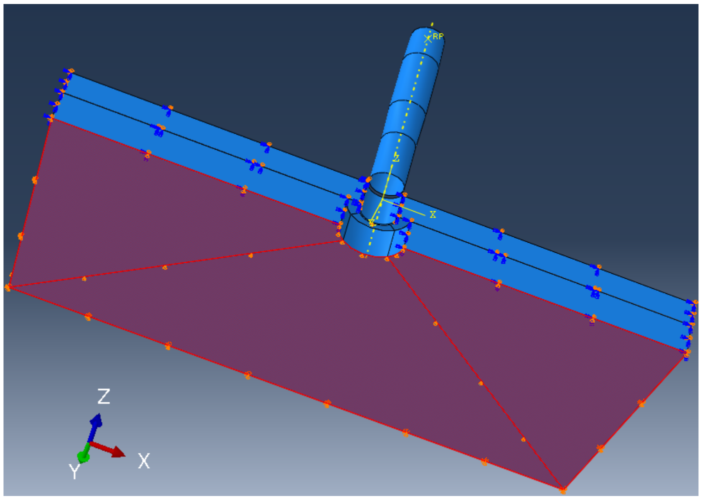

Figure 76. Boundary condition for steel support

4.2.7 Mesh

This study used hexahedral elements, C3D8R, linear brick element with 8 nodes and one integration point (located in the middle). Obviously, the most important region of the work piece is the area close to the notch; therefore, the work piece was divided into three parts using a partition and the mesh was biased in such a way that close to the notch, the mesh was small and far from the notch, it was larger. Similar method is used for steel support, since its geometry is very similar to that of the work piece. For the split sleeve, the fillet area is partitioned to make it easier for the software to generate the mesh. For checking the mesh quality, two criteria were examined:

- Aspect ratio: the ratio of longest to shortest length of each element
- Geometric deviation factor: measurement of the deviation of element edges from the original shape

To do so, the mesh verify tool was used, with default threshold values for the aspect ratio and geometric deviation factor (an aspect ratio greater than 10 and geometric deviation greater than 0.2 is considered unacceptable).

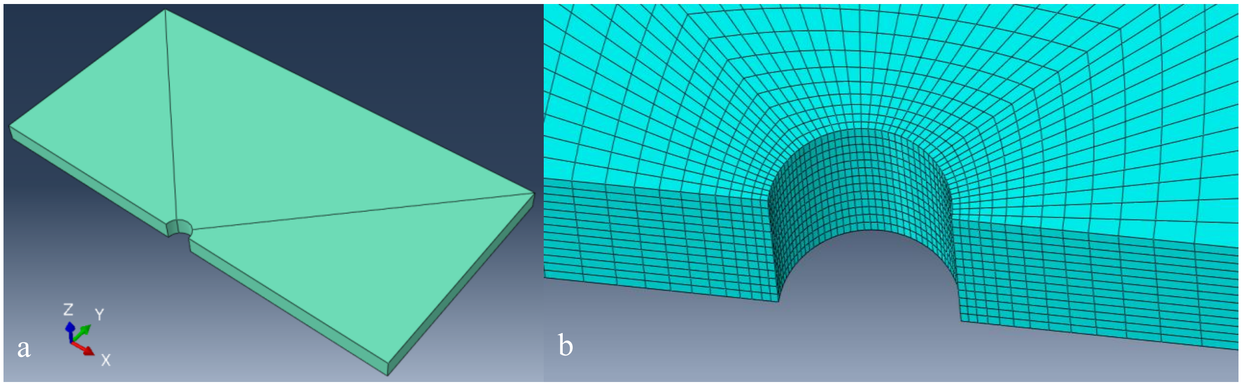

Figure 77. a) partition on the work piece, b) mesh close to notch

For the elements close to the notch, all criteria are satisfied, but for the elements near the edge of the work piece, which have the biggest size (to reduce computation time), the aspect ratio is higher than the recommended value. Since the stress and strain far from notch are very small and are in the elastic regime, the results are reliable. In order to optimize to computation time of the FE models, a mesh convergence study was done. Since the hoop residual stress at the entry site is the most important component of the stress, it was chosen as the reference for convergence study.

Table 14. Convergence study

Number of elements on work piece	Residual hoop stress at notch edge on the entry site (MPa)
8568	-118.889
14053	-99.94
31584	-99.8016

Therefore, the configuration with 14053 element on work piece was chosen as the optimum condition.

4.3 Results and discussion

4.3.1 Radial displacement at the end of loading

Figure 78 shows the radial displacement around the notch during 4% cold expansion. The first assumption in VMP (using the same shape for yield surface and linearly interpolating between tension and compression curves) leads to results very similar to the predictions by ABAQUS. This result can be explained by the fact that in the first assumption, since the dominant stress component in the plastic regime is compressive (Figure 79), the weighted interpolation between tension and compression curve (section 2.2.3.2), is very close to the compression curve. In the elastic regime, the behavior of tension and compression is the same, so considering only compression curve in ABAQUS gets the same results as VMP with the assumption of interpolating between curves.

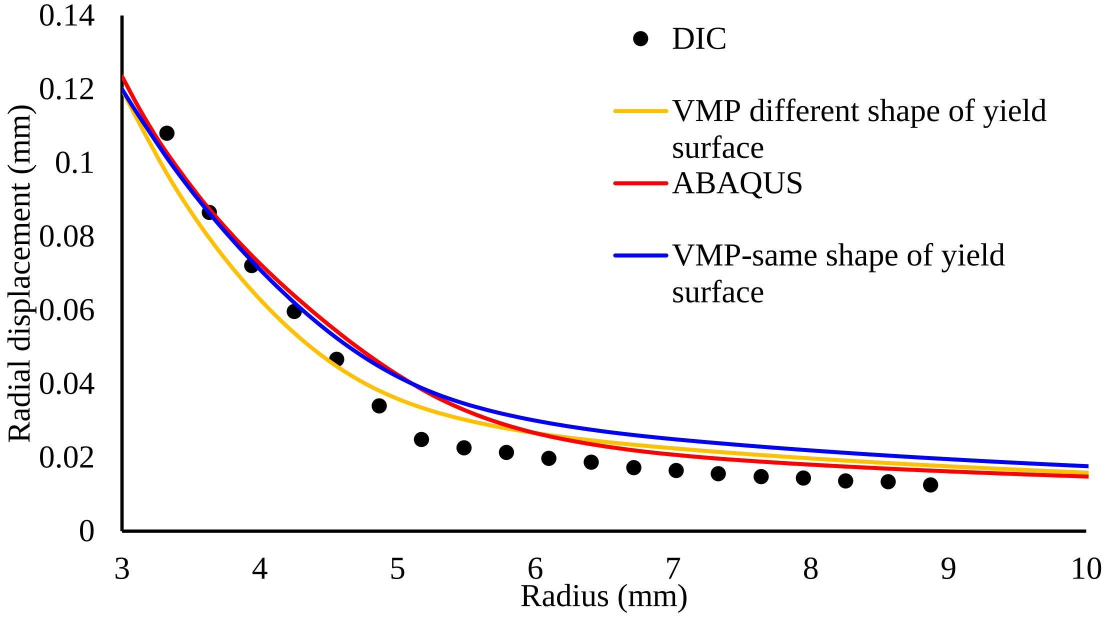

Figure 78. Radial displacement at the end of loading during 4% cold expansion

Updating the shape of the yield surface for each plastic strain predicts the radial displacement more accurately, especially in the plastic regime. So hereafter, the VMP results shown are based on this assumption. It should be noted that in this assumption, the curve used in the projection method is the tensile curve. In the elastic regime (Figure 79), the results by VMP and ABAQUS are close to each other.

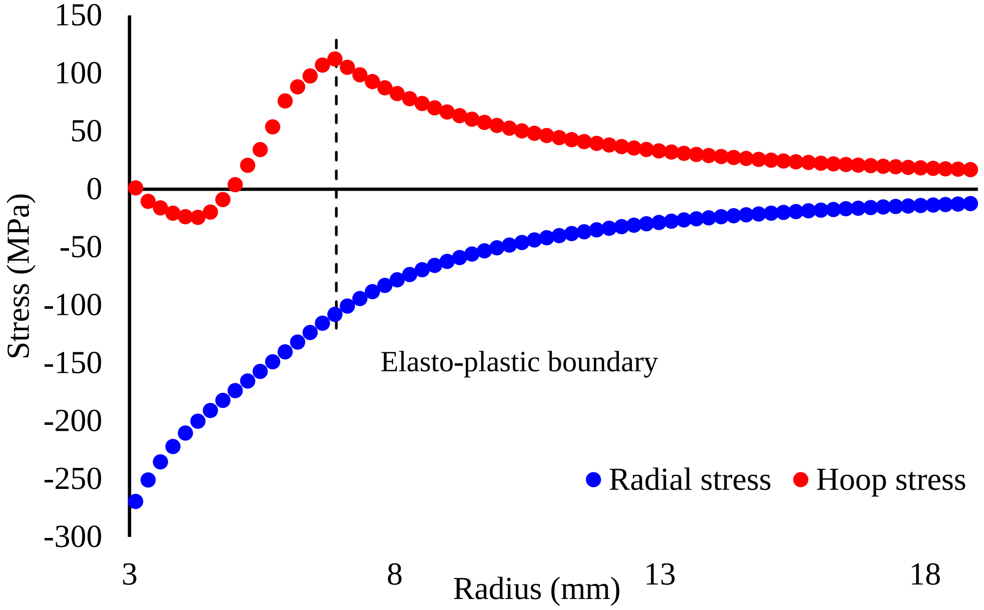

Figure 79. Radial and hoop stress at the end of loading for 4% cold expansion by VMP

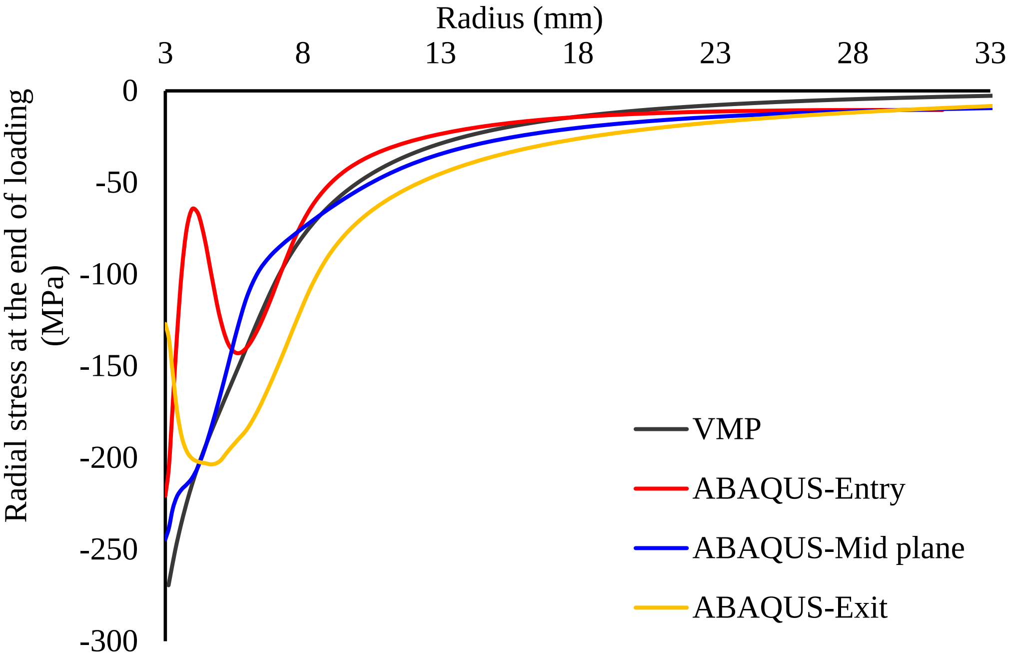

Figure 80. Radial stress distribution at the end of loading

As shown in Figure 80, radial stress at the end of the loading step is very close to the prediction by ABAQUS in the mid plane. In contrast, the radial stress at the entry and exit sites differ significantly, which can be explained by the effect of support, stress in the z direction and contact between the split sleeve and work piece, which the VMP method does not take into account. Figure 81 shows the hoop stress distribution at the end of loading. Same as radial stress, hoop stress predicted by VMP is close to the mid-plane. A little further away from the notch, VMP and mid plane get closer to each other. The difference is due to consideration of asymmetry in VMP. Because in large plastic strain, asymmetric behavior is more pronounced, close to the notch the difference in prediction by VMP and ABAQUS is greater than the difference in the region with smaller plastic or elastic region of the material. The other particular aspect of stress distribution is the existence of a peaks and a valleys in the hoop stress distribution. The first one (around 7 mm) is the elasto-plastic boundary, as can be seen in Figure 82. The other one is due to the sigmoidal behavior of the material (Figure 67), which means material hardens substantially at greater strains. Secant modulus (E_{eff} in VMP), defined as the ratio of stress to the strain as the representative of material behavior in plastic regime, explains this behavior.

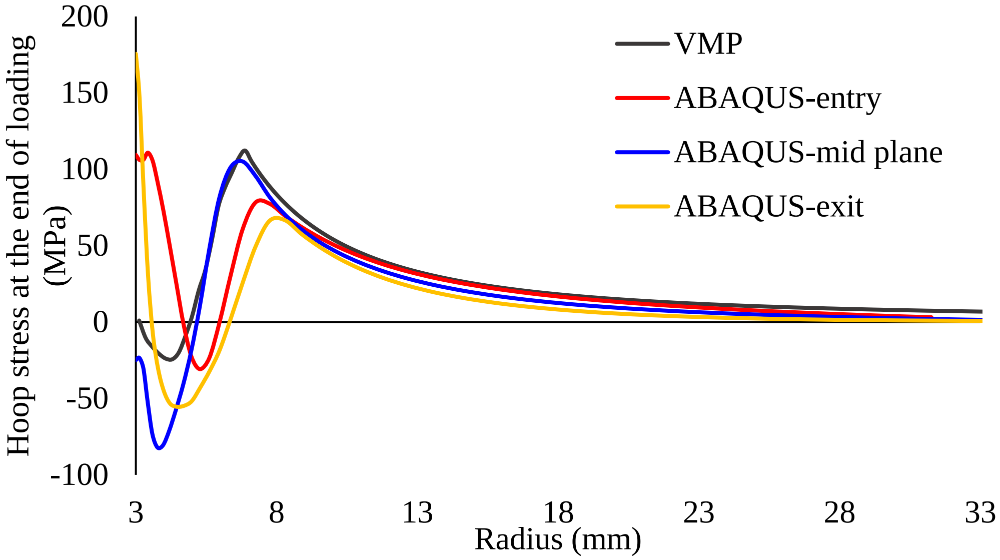

Figure 81. Hoop stress distribution at the end of loading

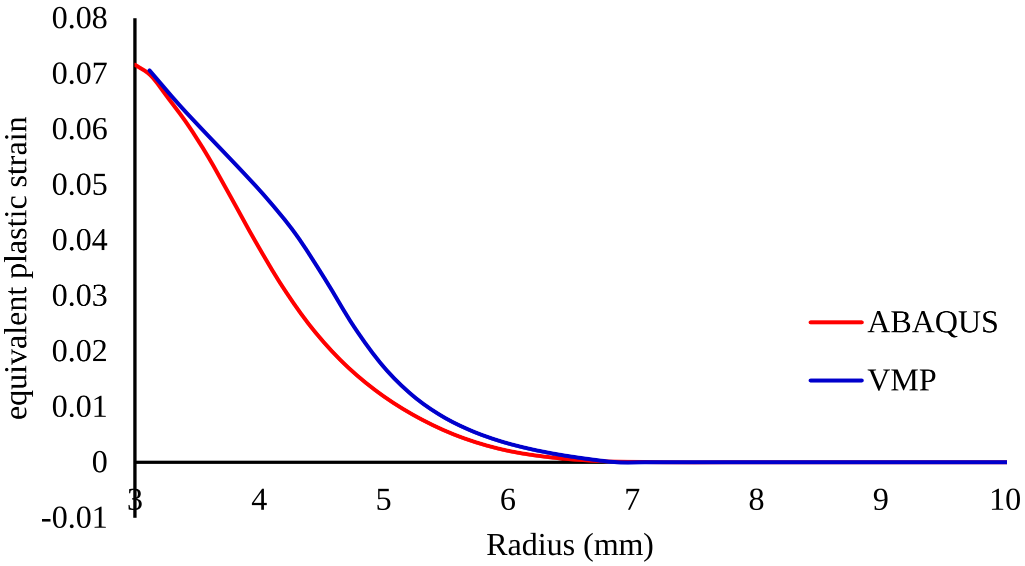

Figure 82. Equivalent plastic strain distribution at the end of loading

The other is a change in the slope of the hoop stress curve, is due to the sigmoidal behavior of the material (Figure 67) which means that material hardens substantially at greater strains. This behavior is explained by secant modulus (E_{eff} in VMP), defined as the ratio of stress to the strain as the representative of material behavior in plastic regime.

In perfectly plastic materials or materials with a low hardening rate, going further into the plastic regime results in a decreased secant modulus, since in the ratio of stress over strain, strain is increasing, but stress is constant or stress increases at a lower rate.

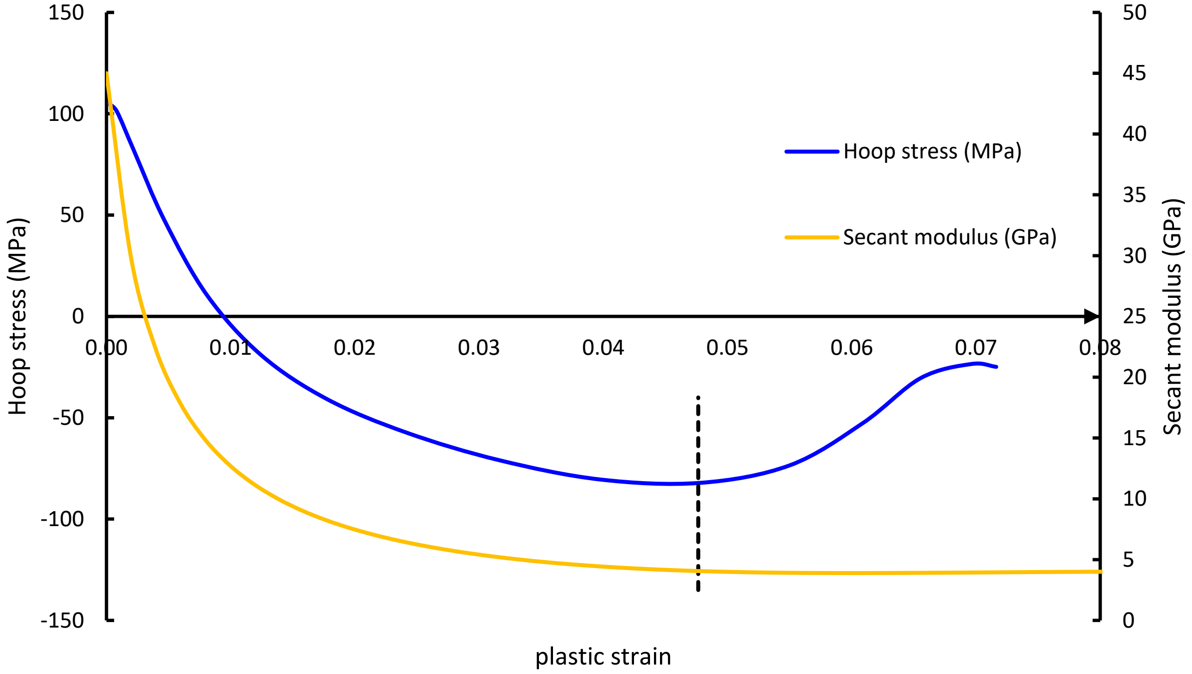

Figure 83. Secant modulus and hoop stress vs plastic strain

In this case, due to the sigmoidal shape of the stress-strain curve, at high strain, the secant modulus reaches a roughly constant value. As shown in Figure 83, the minimum amount of hoop stress occurs where the secant modulus reaches a constant value.

4.3.2 Residual stress distribution

To obtain the residual stress from ABAQUS, same as before, three different radial path far from the position of split were used. It should be mentioned that in the ABAQUS, the unloading behavior of the material was assumed isotropic, while VMP considers actual unloading curves.

Figure 84-Figure 85 show residual radial and hoop stress, respectively.

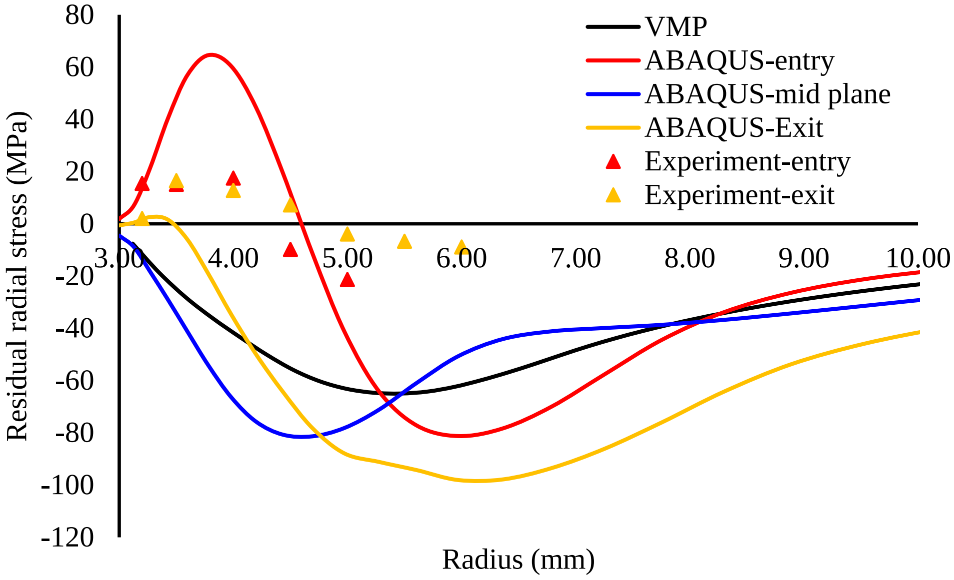

Figure 84. Residual radial stress after 4% cold expansion, experiment vs models

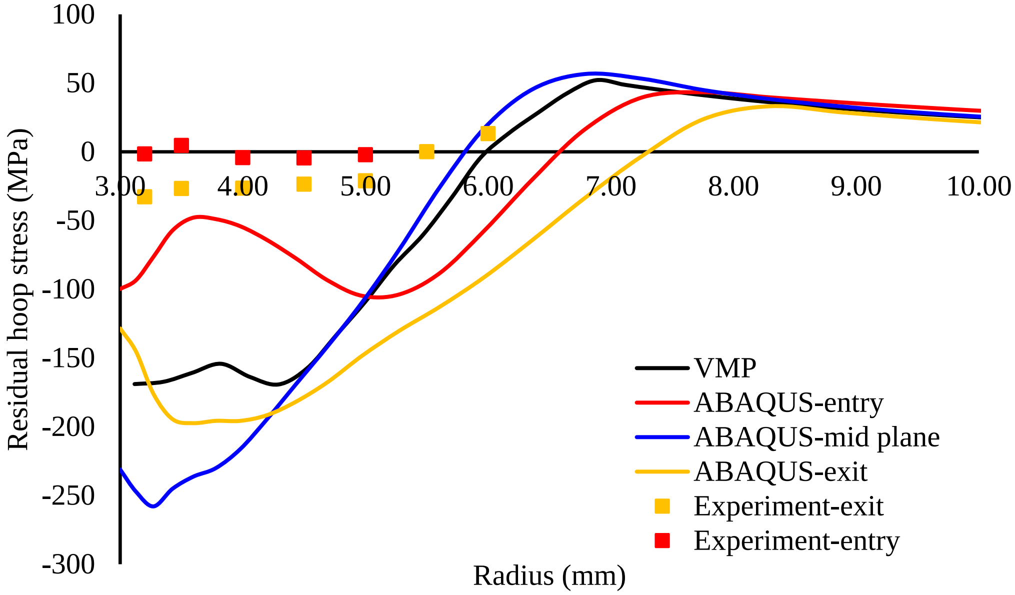

Figure 85. Residual hoop stress after 4% cold expansion, experiment vs models

Above figures, clearly show the experimental measurements are not in good agreement with the models. The disagreement is mainly due to the unloading analysis and the fact that due to texture evolution, material property during unloading is different from what was considered in the model. The simulation process consists of two parts: loading and unloading. The radial displacement measurements shows that the loading solution by VMP and ABAQUS are in good agreement with the experimental values. Therefore, the unloading solution should be reason of the difference between model and experiment. The curve used in VMP for the unloading solution (Figure 19Figure 20); are obtained from the uniaxial curve. Since during cold expansion stress state of each elements is multiaxial, it appears that the actual unloading curve of the material is different from the curves constructed from the uniaxial unloading curves.

On the other hand, small values of experimental residual stress suggests that during unloading, reverse yielding should occur sooner. However, the curves of Figure 19-20 shows the unloading curves have a fair amount of elastic behavior before reverse yield occurs. Consequently, considering the effect of unloading form a biaxial stress state as well as the asymmetric behavior, needs more considerations.

4.4 Parametric study

In this section, firstly, the effect of different BCs on current FE models are reviewed. In most of available FE models of cold expansion process, the presence of the support of work piece is ignored; therefore, a parametric study on the effect of work piece on residual stress distribution is necessary. Results of ABAQUS presented so far are based on the assumption that there is no friction in contacts, to make it comparable with VMP results. Thus, the effect of friction on residual stress distribution is investigated in this section. Subsequently, a model for double cold expansion is presented.

4.4.1 Boundary conditions

In many of the current models presented in literature ([138], [139], [142], [144]), the boundary conditions for the work piece is constraining the movement of the edge of the work piece in direction of the displacement of the mandrel. Here a comparison between this boundary condition and using a support to prevent the work piece from moving (the FE model used in this study) is made.

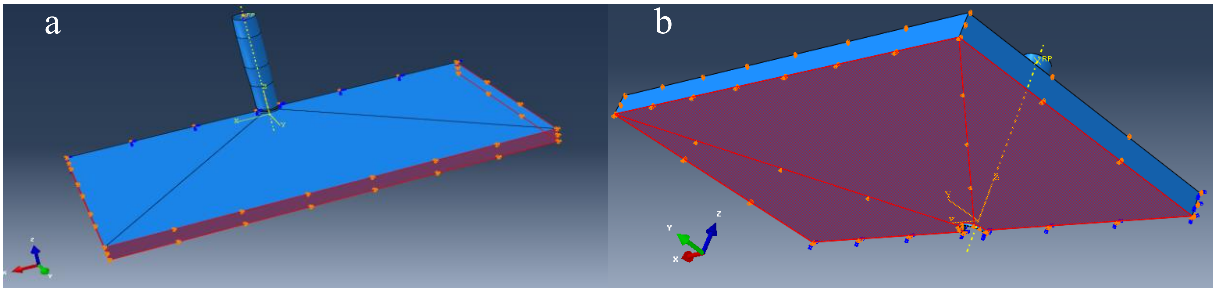

Figure 86. Two different boundary condition for work piece a) edge, b) the bottom surface are constrained from moving in the z direction

The results of these two different boundary conditions in the FE model (shown in Figure 86) are compared with the results of a more complex and more realistic FE model, the one with constraining the steel plate as a support for the work piece (Figure 76). In the following figures, the “edge” and “bottom surface” refer to boundary conditions in Figure 86 a and b, respectively, whereas “support” refers to BC shown in Figure 76. Other parameters are similar to the main model, except the friction. For this comparison, the friction coefficient between mandrel and inner surface of split sleeve and outer surface of split sleeve and magnesium work piece was considered to be 0.2, to have a better contrast of the difference between results.

Figures below shows the comparison between residual radial and hoop stress fields at the entry face, mid-plane and exit side of the work piece, for 4% cold expansion.

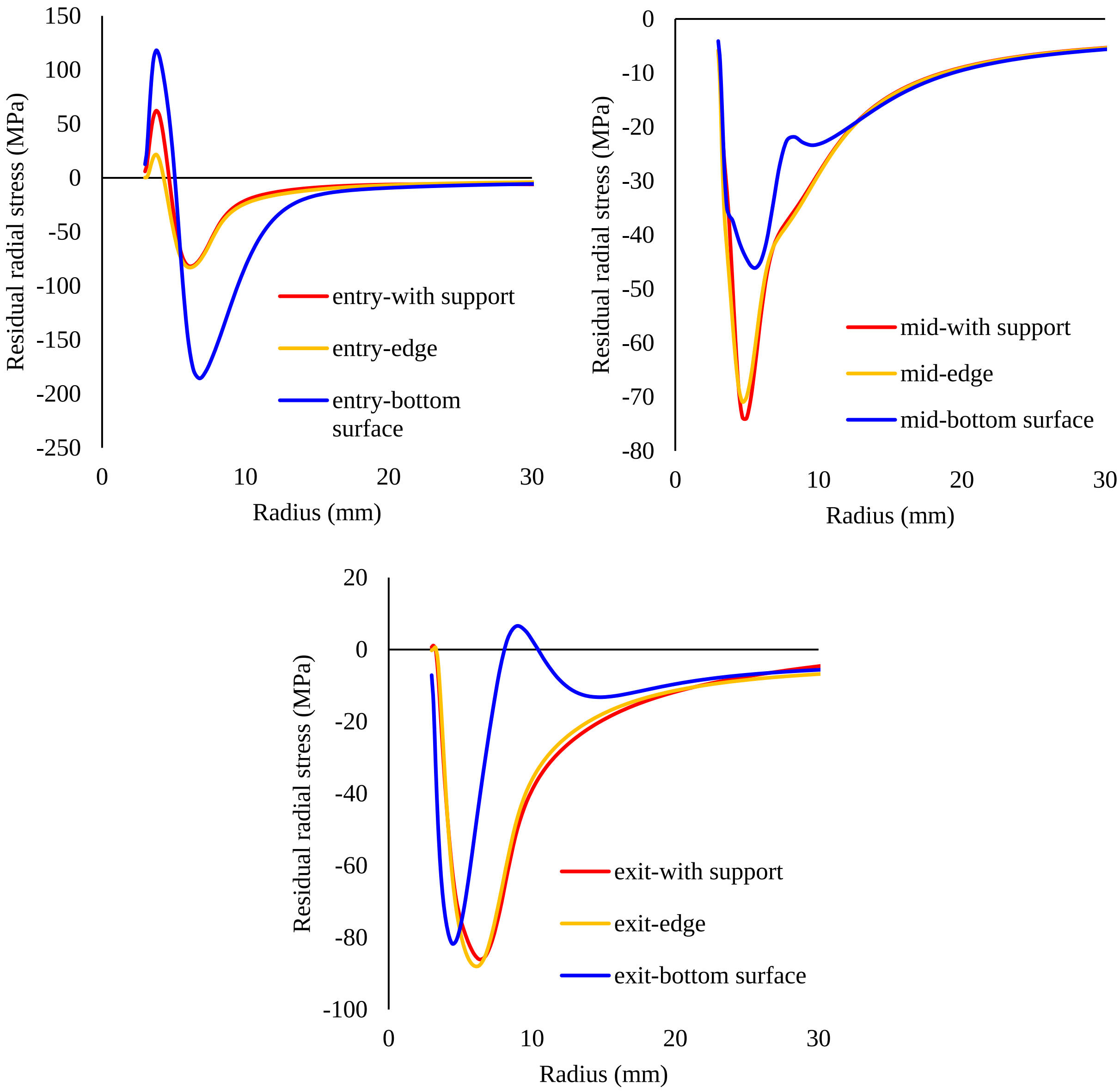

Figure 87. Residual radial stress distribution by three different boundary condition, including with support, fixed bottom surface and fixed edge of the work piece

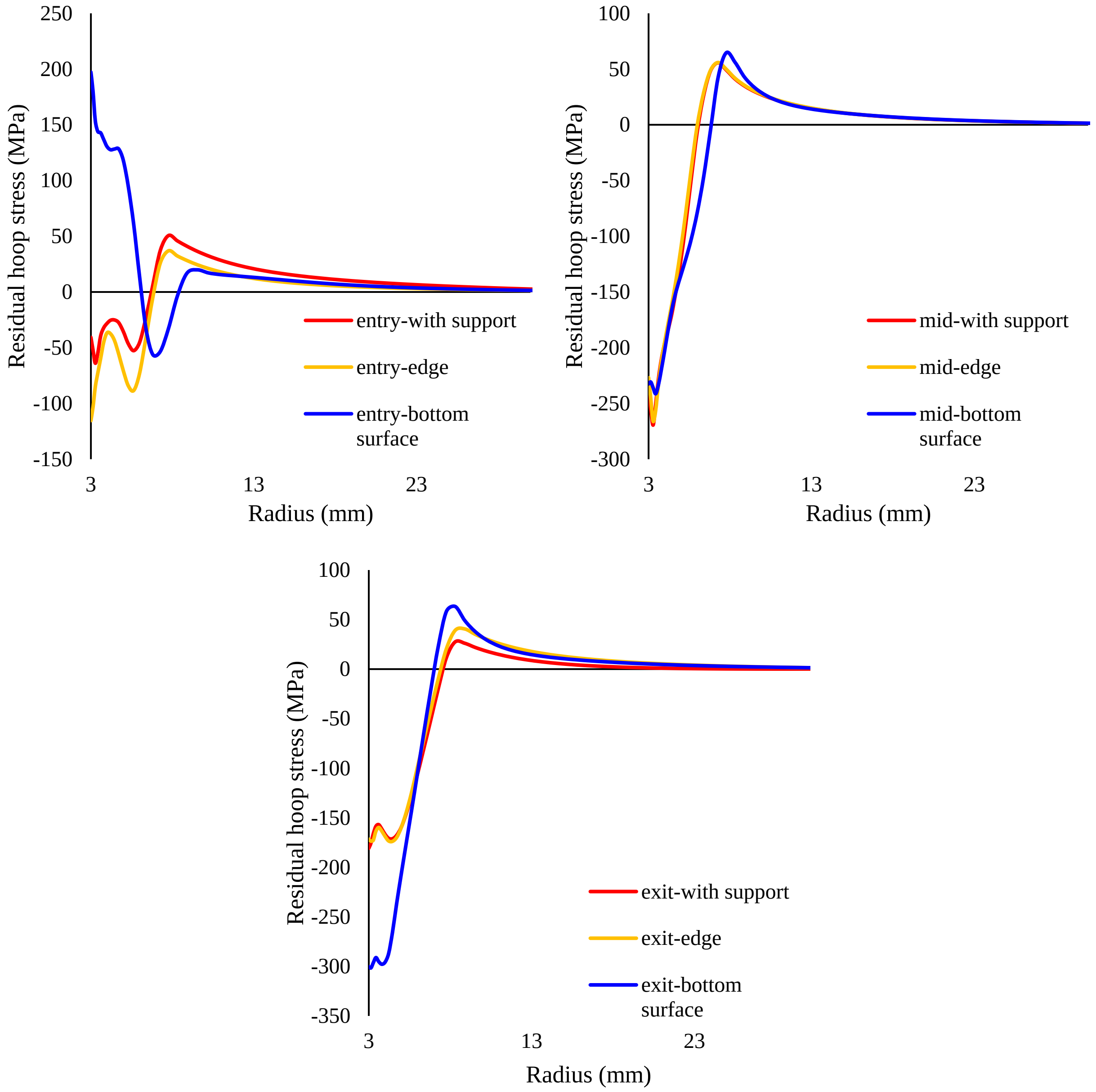

Figure 88. Residual hoop stress distribution by three different boundary condition

This comparison points out few interesting results. Firstly, the residual stress (especially hoop stress) at the entry side of the work piece, which is the critical point for fatigue due to lower residual stress, is more sensitive to different boundary conditions. Secondly, for the “edge” boundary condition, the mid plane and exit site shows similar results as the “support” boundary condition, while the results of hoop residual stress at the entry side is significantly different.

Therefore, the simpler FE model without support for the work piece may not be the best BC to use. The following results are from models with “support” for the work piece.

4.4.2 The effect of friction on the residual stress

The effect of friction between different parts in cold expansion process has been reported in literature. It was shown that residual stress at the entry face is the most-affected component ([139][144][136]). On the other hand, a more realistic boundary condition has proven that considering a support for work piece, significantly affect the hoop stress at entry face. In this regard, examining the effect of friction with this new boundary conditions seems necessary. To do so, six different configurations of the contact between mandrel and split sleeve and split sleeve and workpiece were considered. In following graphs, the radius is measured from hole center.

Table 15. Different frictions considered in ABAQUS

Components	Friction coefficient value	symbol
Mandrel-inner surface of split sleeve	0.1, 0.2	ms
Outer surface of split sleeve-work piece	0.1, 0.2	sw
Mandrel-inner surface of split sleeve and Outer surface of split sleeve-work piece	0, 0.2	msw

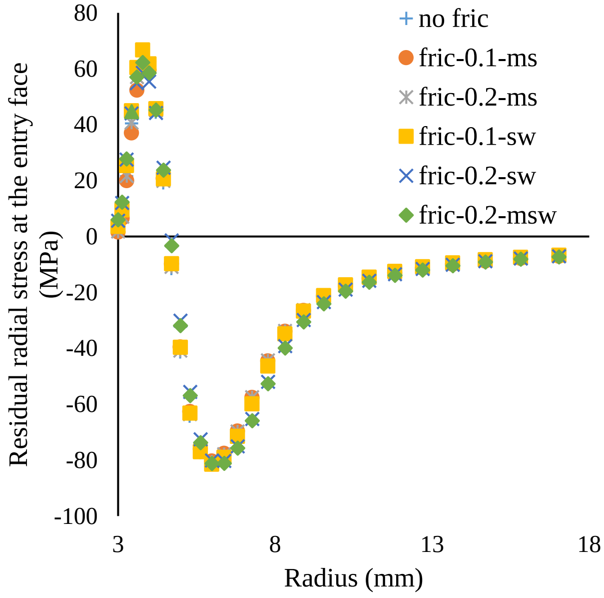

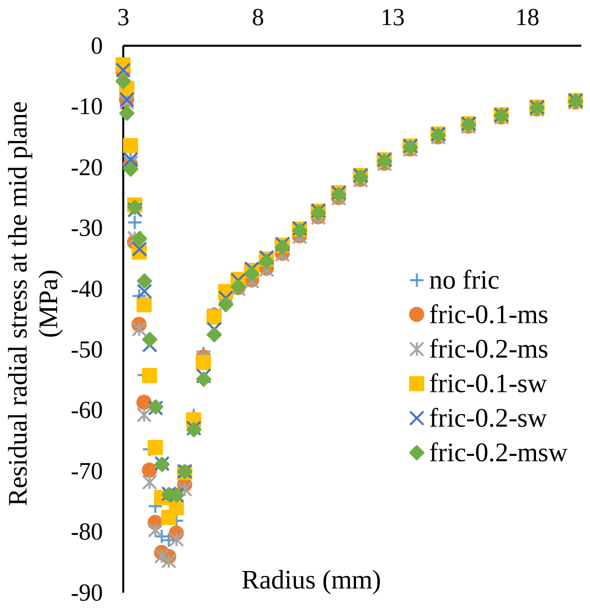

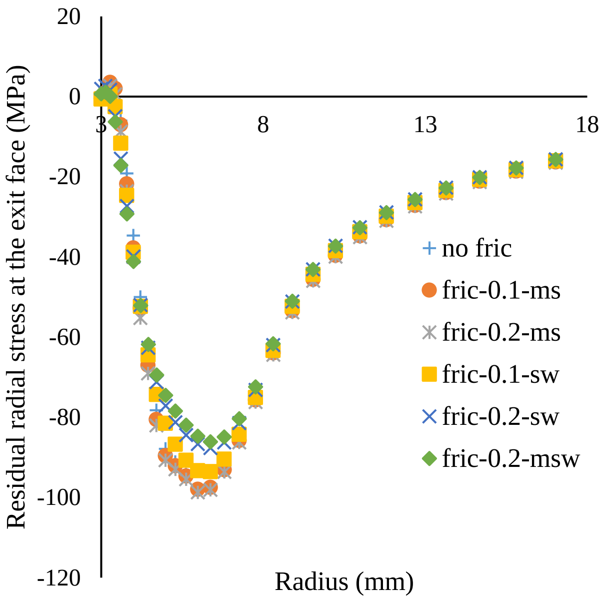

Figure 89. Residual radial stress distribution on (from left to right) entry, mid plane and exit face for different frictions

The values of friction coefficient were chosen based on recommendations by literature [144]. Residual radial stress at the entry side is roughly the same for all of the above-mentioned configurations. For the mid plane and exit side, friction between mandrel and split sleeve results in the highest maximum compressive residual stress. As expected, residual hoop stress is more sensitive to the friction. The hoop stress on the entry side at notch root gets the lowest value in the case that there is friction between mandrel and sleeve. For the exit side, due to reverse yielding, the residual hoop stress has a smaller value close to the notch root. On the exit side, in the case of friction coefficient of 0.1 between split sleeve and work piece, the residual hoop stress has the highest absolute value, since the unloading seems to be elastic, but on the other hand, the residual hoop on the entry side with this configuration has a smaller value in comparison with the no friction scenario. The hoop stress distribution on the mid plane is not a function of friction. The hoop stress distribution is shown in the following figure.

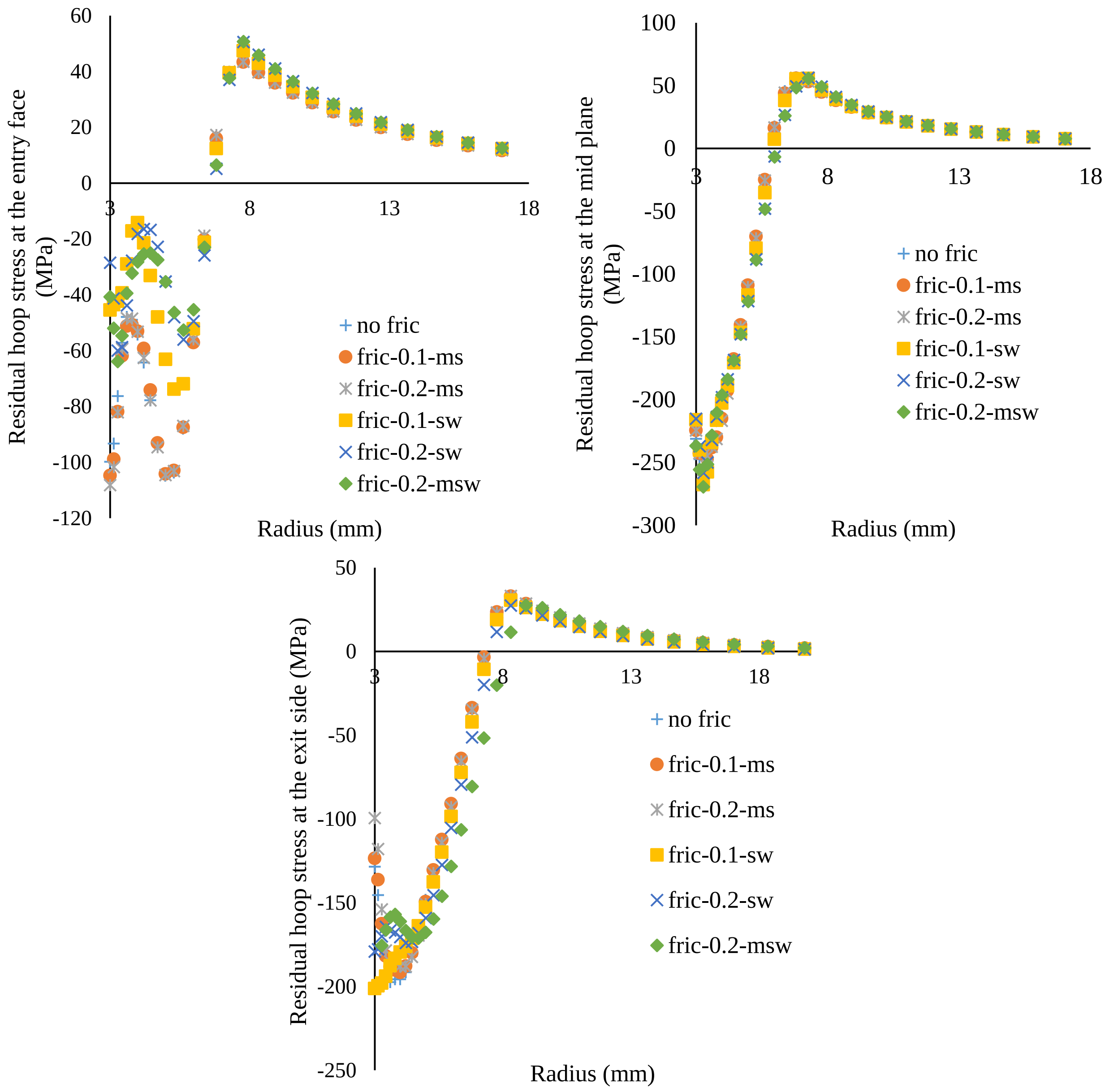

Figure 90. Residual hoop stress distribution on (from left to right) entry, mid plane and exit face for different frictions

4.4.3 Proposing a FE model for double cold expansion

Surprisingly, FE models of double cold expansion process are not well documented in literature. Among available models, some consider the ball expansion to avoid the complexity of the split sleeve process ([147]), while others ([145][146]), model a tapered mandrel as the way of modeling the cold expansion process. To the best of author's knowledge, there is no FE model for double split sleeve cold expansion.

As shown in section 4.4.1, common FE models in literature with simple boundary conditions, are unable to predict the residual stress accurately, especially on the entry side. Therefore, the support of the work piece should also be considered in the double cold expansion model. Since the tapered part of the mandrel is not symmetric with respect to its maximum diameter section, for the second pass of cold expansion, a mandrel with same geometry but rotated along x axis was implemented in the following model. Due to bulging around the exit face of the notch after the first pass, the surface, which the support is in contact with, is not flat for the second pass. To consider the effect of this, the structure was assembled in such a way that there was a small gap between the support of the second pass and the work piece in the initial assembly. This gap was chosen based on the bulging around the notch in the first pass, measured from the single cold expansion in ABAQUS.

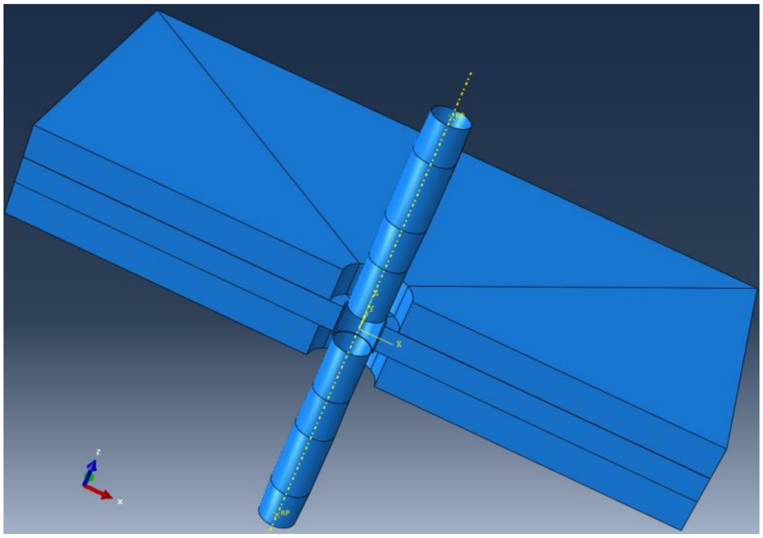

Figure 91. FE model for double cold expansion

Figure 92 shows the results of 4% cold expansion (initial). The residual hoop stress at the entry side (of the first pass) is the most affected, while on the exit side and the mid plane the effect of double cold expansion is not considerable. The results of the residual stress predicted by the proposed model is in agreement with the trend observed in the XRD measurements of double and single cold expansion. Due to the increase in the value of hoop residual stress at the entry side while the on the exit side the change is not significant, the distribution of residual stress through thickness is more uniform after double cold expansion.

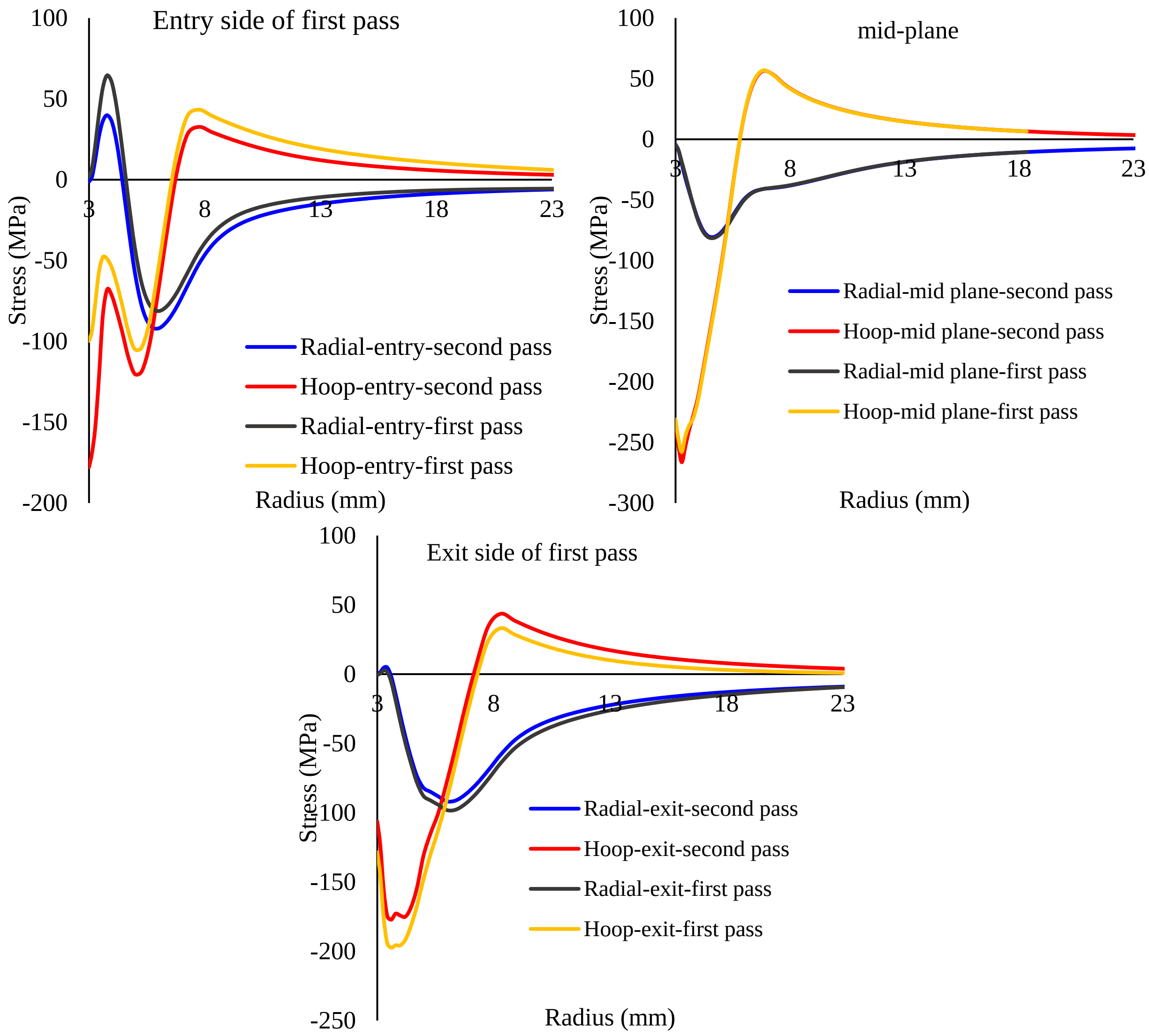

Figure 92. Residual stress of opposite direction double cold expansion versus single cold expansion

As Figure 92 clearly shows, residual hoop stress at the entry side (of the first pass) is the most affected, while on the exit side at the mid plane, the effect of double cold expansion is minimal, which is in agreement with the trend observed in the XRD measurements of double and single cold expansion. With increase of the residual hoop stress at the entry side, the distribution of residual stress through thickness is more uniform after double cold expansion. In a qualitative comparison, the effect of the second pass of expansion agrees with XRD measurements (Figure 93) on 4% (initial) cold expansion. This measurements confirms a significant increase in the value of hoop residual stress at entry site, while the value on the exit site is less affected. In a quantitative comparison, values of FE does not agree with experiment, due to lack of accurate model to predict the unloading behavior.

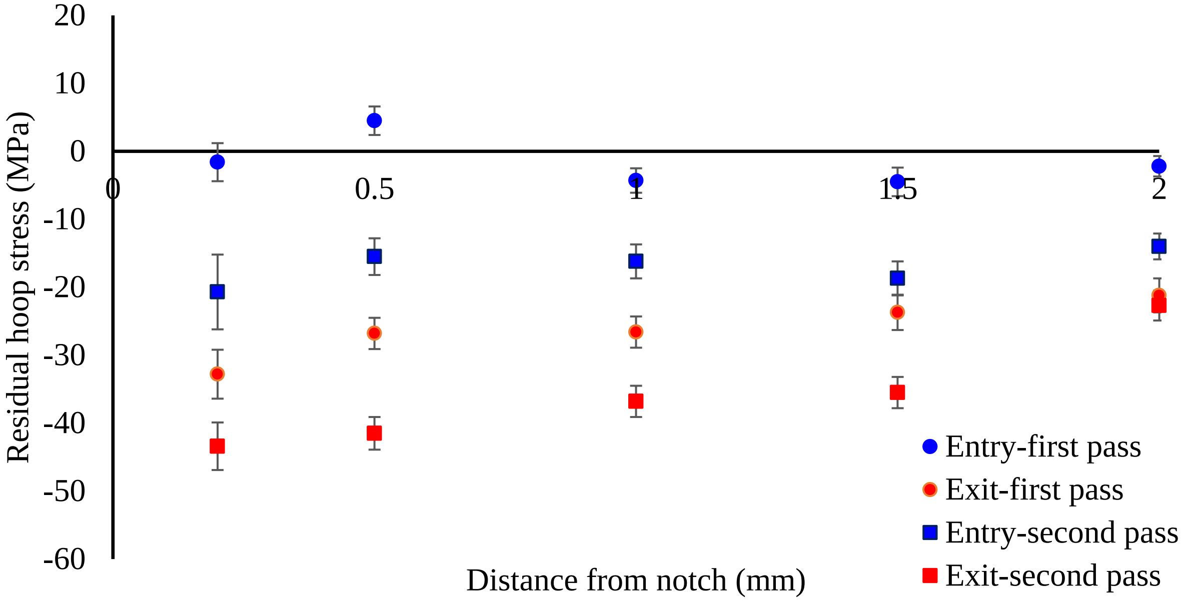

Figure 93. Residual stress measurement on 4% (initial) double cold expansion, 4mm sheet

Chapter 5. Conclusions and future work

This study had two main objectives: experimental and numerical studies of the cold expansion of magnesium AZ31B sheets. In the experimental part, first of all the feasibility of cold expansion of a central hole in a rolled AZ31B magnesium alloy has been investigated. The following conclusions can be made from this part of the study:

- Split sleeve cold expansion of AZ31B magnesium sheet with 3.18 mm thickness up to 6% without local damage (inducing macro and/or micro cracks) is feasible.
- Generated residual stresses are not uniform through the thickness and have lower values at the entry face.
- Different percentages of cold expansion result in different amounts of fatigue life improvement in the AZ31B sheet.
- A high percentage of cold expansion can cause micro-cracks inside the material, which can result in a shortening the fatigue life.
- In fatigue tests of cold expanded samples both crack initiation and propagation life increase compared to untreated samples.
- The improvement in fatigue life depends on the stress level. For low cycle fatigue (high stress amplitudes) the improvement factor is around 2.5x and in the high cycle fatigue (lower stress amplitudes) is as high 10x.
- The main improvement is due to the presence of favorable residual stresses that resulted in delay in crack initiation (i.e., when the crack reaches the notch surface). Besides, possible grain refinement can also be a reason of the observed fatigue life improvement.
- In untreated samples, crack initiation occurs at the notch edge in multiple locations, in both low and high cycle fatigue. In cold expanded samples, in high cycle fatigue, crack initiation occurs at notch root, but fewer initiation points were observed. In contrast, in high cycle fatigue of cold expanded sample, crack initiation happens at subsurface. The evolution of texture due to cold expansion, grain refinement and residual stress are the possible reasons of this phenomenon.

- In the modeling part, VMP and ABAQUS were implemented to model the process. The following conclusions can be made:

  - Compressive stress is dominant in the biaxial stress states of the elements during loading phase of the process. Therefore, considering only compression behavior of the material in the ABAQUS yields similar results to VMP, in which asymmetric behavior is considered.
  - According to the experimental measurements of the radial displacement field around the notch during loading, both VMP and ABAQUS predicted this displacement with good accuracy. The results of VMP are closest to the experimental measurements.
  - For the unloading part, both VMP and ABAQUS over predict the residual stress field as compared to the XRD measurements. VMP with its capability of considering actual behavior was expected to yield better predictions, which suggests that the current way of considering unloading behavior and the effect of material asymmetry in the VMP model is not sufficient. As a side note, it should be mentioned that low values of residual stress mean that reverse yield occurs sooner than what predicted by VMP.

Future work

As a result of this research, the following suggestions for future work can be made:

- For sake of modelling, series of biaxial loading-unloading tests with different values of strain can provide a better understanding of unloading behavior from a biaxial stress state. To assign an unloading curve to each element at the end of loading, consideration of other criteria s such as plastic work should be examined. To do so, the amount of plastic work each elements gain during loading can be compared to that of uniaxial curve.
- Effect of plate thickness on residual stress field: differences in the residual stress distribution on thick and thin plates should be examined. To do so, specimens from same sheet machined to different thickness can be investigated. Difference in residual stress in

thick and thin plates can help understanding the effect of sheet thickness on residual stress distribution, which will be beneficial for optimizing the process.

- A next step is to adopt a fatigue damage model and predict the life using available experimental residual stress values. Since considering the effect of residual stress is not efficient in stress-based approach (S-N), strain-based approaches such as Smith-Watson-Topper with capability of dealing with residual stress is suggested. To do so, using available data for of SWT parameter for smooth specimen as well as using Neuber or Glinka’s rule to calculate strain at notch root is required.
- Examining the difference between residual stress distribution on opposite direction double cold expanded and same direction double cold expanded samples and the effect on fatigue life, can be beneficial for the sake of optimizing the process from residual and fatigue life point of view. It is expected to have a more uniform residual stress in opposite direction double expansion compared to a single pass. Experimental validation of the superiority of opposite direction versus same direction double cold expansion is of significant importance.

References

[1] M. Meinshausen, N. Meinshausen, W. Hare, S. C. B. Raper, K. Frieler, R. Knutti, D. J. Frame, and M. R. Allen, “Greenhouse-gas emission targets for limiting global warming to 2 degrees C.,” *Nature*, vol. 458, no. 7242, pp. 1158–1162, 2009.

[2] E. Nederhoff, *Transport Energy and CO2 : Moving towards Sustainability - Books - OECD iLibrary*. 2009.

[3] B. Terefe, “Greenhouse Gas Emissions From Private Vehicles in Canada, 1990 to 2007,” 2007.

[4] G. S. Cole and a. M. Sherman, “Light weight materials for automotive applications,” *Mater. Charact.*, vol. 35, no. 1, pp. 3–9, 1995.

[5] E. A. Starke and J. T. Staley, “Application of modern aluminum alloys to aircraft,” *Prog. Aerosp. Sci.*, vol. 32, no. 2–3, pp. 131–172, 1996.

[6] H. Friedrich and S. Schumann, “Research for a ‘new age of magnesium’ in the automotive industry,” *J. Mater. Process. Technol.*, vol. 117, no. 3, pp. 276–281, 2001.

[7] A. Stalmann, W. Sebastian, H. Friedrich, S. Schumann, and K. Dröder, “Properties and processing of magnesium wrought products for automotive applications,” *Adv. Eng. Mater.*, vol. 3, no. 12, pp. 969–974, 2001.

[8] L. Ostrovsky and Y. Henn, “Present state and future of magnesium application in aerospace industry,” *Int. Conf. "New Challenges Aeronaut. ASTEC 07*, pp. 1–5, 2007.

[9] G. Song and a. Atrens, “Understanding Magnesium Corrosion—A Framework for Improved Alloy Performance,” *Adv. Eng. Mater.*, vol. 5, no. 12, pp. 837–858, 2003.

[10] Y. Fu, E. Ge, H. Su, J. Xu, and R. Li, “Cold expansion technology of connection holes in aircraft structures: A review and prospect,” *Chinese J. Aeronaut.*, vol. 28, no. 4, pp. 961–973, 2015.

[11] G. L. Kulak, J. W. Fisher, and J. H. A. Struik, *Guide to design criteria for bolted and riveted joints*, vol. 15, no. 1. 1988.

[12] I. Stephens, Ralph, A. Fatemi, R. Stephens, Robert, and O. Fuchs, Henry, “Metal Fatigue in Engineering,” *Journal of Engineering Materials and Technology*. p. 472, 2001.

[13] M. A. S. Torres and H. J. C. Voorwald, “An evaluation of shot peening, residual stress and stress relaxation on the fatigue life of AISI 4340 steel,” *Int. J. Fatigue*, vol. 24, pp. 877–

886, 2002.

[14] Y. Sano, M. Obata, T. Kubo, N. Mukai, M. Yoda, K. Masaki, and Y. Ochi, “Retardation of crack initiation and growth in austenitic stainless steels by laser peening without protective coating,” *Mater. Sci. Eng. A*, vol. 417, no. 1–2, pp. 334–340, 2006.

[15] H. D. Gopalakrishna, H. N. Narasimha Murthy, M. Krishna, M. S. Vinod, and A. V. Suresh, “Cold expansion of holes and resulting fatigue life enhancement and residual stresses in Al 2024 T3 alloy - An experimental study,” *Eng. Fail. Anal.*, vol. 17, no. 2, pp. 361–368, 2010.

[16] D. A. Clark and W. S. Johnson, “Temperature effects on fatigue performance of cold expanded holes in 7050-T7451 aluminum alloy,” *Int. J. Fatigue*, vol. 25, no. 2, pp. 159–165, 2003.

[17] T. Ozdemir and L. Edwards, “Through-Thickness Residual Stress Distribution After the Cold Expansion of Fastener Holes and Its Effect on Fracturing,” *J. Eng. Mater. Technol.*, vol. 126, no. 1, p. 129, 2004.

[18] R. A. Pell, P. W. Beaver, J. Y. Mann, and J. G. Sparrow, “Fatigue of ThickSection ColdExpanded Holes With and Without Cracks,” *Fatigue Fract. Eng. Mater. Struct.*, vol. 12, no. 6, pp. 553–567, 1989.

[19] M. O. Andar, T. Kuwabara, and D. Steglich, “Material modeling of AZ31 Mg sheet considering variation of r-values and asymmetry of the yield locus,” *Mater. Sci. Eng. A*, vol. 549, pp. 82–92, 2012.

[20] S. H. Park, S. G. Hong, W. Bang, and C. S. Lee, “Effect of anisotropy on the low-cycle fatigue behavior of rolled AZ31 magnesium alloy,” *Mater. Sci. Eng. A*, vol. 527, no. 3, pp. 417–423, 2010.

[21] M. Knezevic, A. Levinson, R. Harris, R. K. Mishra, R. D. Doherty, and S. R. Kalidindi, “Deformation twinning in AZ31: Influence on strain hardening and texture evolution,” *Acta Mater.*, vol. 58, no. 19, pp. 6230–6242, 2010.

[22] X. Y. Lou, M. Li, R. K. Boger, S. R. Agnew, and R. H. Wagoner, “Hardening evolution of AZ31B Mg sheet,” *Int. J. Plast.*, vol. 23, no. 1, pp. 44–86, 2007.

[23] S. B. Behravesh, “Fatigue Characterization and Cyclic Plasticity Modeling of Magnesium Spot-Welds,” University of Waterloo, 2013.

[24] M. A. Khayamian, B. Behravesh, and H. Jahed, “Incorporation of asymmetric yield and hardening behaviour in axisymmetric elastoplastic problems,” *Mater. Des.*, vol. 99, pp.

490–499, 2016.

[25] A. Nadai, “Theory of the Expanding of Boiler and Condenser Tube Joints Through Rolling,” *TRANS.ASME*, vol. 65, pp. 865–880, 1943.

[26] J. Chang, “Analytical prediction of fatigue crack growth at cold-worked fastener holes,” *16TH Struct. Dyn. Mater. Conf.*, 1975.

[27] Rich and Impellizzeri, “Fatigue analysis of cold-worked and interference fit fastener holes,” *ASTM Spec Tech Publ 637*, pp. 153 – 175, 1977.

[28] S. Poolsuk and W. N. Sharpe, “Measurement of the Elastic-Plastic Boundary Around Coldworked ",” *J. Appl. Mech.*, vol. 45, no. 78, 1978.

[29] G. S. Wang, “An elastic-plastic solution for a normally loaded center hole in a finite circular body,” *Int. J. Press. Vessel. Pip.*, vol. 33, no. 4, pp. 269–284, 1988.

[30] D. L. Ball, “ElasticPlastic Stress Analysis of Cold Expanded Fastener Holes,” *Fatigue Fract. Eng. Mater. Struct.*, vol. 18, no. 1, pp. 47–63, 1995.

[31] J. Kim, H. Ryou, D. Kim, D. Kim, W. Lee, S. H. Hong, and K. Chung, “Constitutive law for AZ31B Mg alloy sheets and finite element simulation for three-point bending,” *Int. J. Mech. Sci.*, vol. 50, no. 10–11, pp. 1510–1518, 2008.

[32] M. Li, X. Y. Lou, J. H. Kim, and R. H. Wagoner, “An efficient constitutive model for room-temperature, low-rate plasticity of annealed Mg AZ31B sheet,” *Int. J. Plast.*, vol. 26, no. 6, pp. 820–858, 2010.

[33] M. G. Lee, S. J. Kim, R. H. Wagoner, K. Chung, and H. Y. Kim, “Constitutive modeling for anisotropic/asymmetric hardening behavior of magnesium alloy sheets: Application to sheet springback,” *Int. J. Plast.*, vol. 25, no. 1, pp. 70–104, 2009.

[34] a. Staroselsky and L. Anand, “A constitutive model for hcp materials deforming by slip and twinning: Application to magnesium alloy AZ31B,” *Int. J. Plast.*, vol. 19, no. 10, pp. 1843–1864, 2003.

[35] S. R. Agnew and Ö. Duygulu, “Plastic anisotropy and the role of non-basal slip in magnesium alloy AZ31B,” *Int. J. Plast.*, vol. 21, no. 6, pp. 1161–1193, 2005.

[36] H. Jahed and R. N. Dubey, “An axisymmetric method of elastic-plastic analysis capable of predicting residual stress field,” *J. Press. Vessel Technol.*, vol. 119, no. 3, pp. 264–273, 1997.

[37] T. Al-Samman and G. Gottstein, “Room temperature formability of a magnesium AZ31

alloy: Examining the role of texture on the deformation mechanisms," *Mater. Sci. Eng. A*, vol. 488, no. 1–2, pp. 406–414, 2008.

[38] M. K. Kulekci, "Magnesium and its alloys applications in automotive industry," *Int. J. Adv. Manuf. Technol.*, vol. 39, no. 9–10, pp. 851–865, 2008.

[39] A. A. Roostaei and H. Jahed, "Role of loading direction on cyclic behaviour characteristics of AM30 extrusion and its fatigue damage modelling," *Mater. Sci. Eng. A*, vol. 670, pp. 26–40, 2016.

[40] B. L. Mordike and T. Ebert, "Magnesium Properties - applications - potential," *Mater. Sci. Eng. A*, vol. 302, no. 1, pp. 37–45, 2001.

[41] C. Balwert, N. Hort, and K.U. Kainer, "Automotive applications of magnesium and its alloys," *Trans. Indian Inst. Met.*, vol. 57, no. 4, pp. 397–408, 2004.

[42] C. C. Chao, "Assessment of carbon emission costs for air cargo transportation," *Transp. Res. Part D Transp. Environ.*, vol. 33, pp. 186–195, 2014.

[43] J. Hirsch and T. Al-Samman, "Superior light metals by texture engineering: Optimized aluminum and magnesium alloys for automotive applications," *Acta Mater.*, vol. 61, no. 3, pp. 818–843, 2013.

[44] M. Avedesian and H. Baker, *ASM Handbook: Magnesium and Magnesium Alloys*. ASM Specialty Handbook, 1999.

[45] P. D. Caton, "Magnesium- an Old Material with new Applications," *Mater. Des.*, vol. 12, no. 6, pp. 137–139, 1991.

[46] C. S. Roberts, *The deformation of magnesium. Magnesium and its Alloys*. New York: Wiley, 1964.

[47] V. Tabacaru and N. Oancea, "Sheet metal forming of magnesium wrought alloys - Formability and process technology," *J. Mater. Process. Technol.*, vol. 115, no. 1, pp. 14–19, 2001.

[48] C. Bettles and M. Gibson, "Current wrought magnesium alloys: Strengths and weaknesses," *Jom*, vol. 57, no. 5, pp. 46–49, 2005.

[49] F. K. Chen and T. Bin Huang, "Formability of stamping magnesium-alloy AZ31 sheets," *J. Mater. Process. Technol.*, vol. 142, no. 3, pp. 643–647, 2003.

[50] G. I. Taylor, "Plastic strain in metals," *Twenty-eighth May Lecture to the Institute of Metals*. pp. 307–325, 1938.

[51] B. c. Wonsiewicz and W. A. Backofen, "PLASTICITY OF MAGNESIUM CRYSTALS," *Trans. Metall. Soc. Aime*, vol. 239, no. 9, p. 1422-, 1967.

[52] P. Flynn Ward, J. Mote, and J. . Dorn, "On the thermally activated mechanism of prismatic slip in magnesium single crystals," *Trans. Met. Soc. AIME*, vol. 221, pp. 1148–1154, 1969.

[53] R. . Reed-Hill and W. D. Robertson, "Pyramidal Slip in Magnesium," *Trans. Metall. Soc. AIME*, vol. 221, pp. 256–259, 1958.

[54] H. Wang, P. Wu, and J. Wang, "Numerical Assessment of the Role of Slip and Twinning in Magnesium Alloy AZ31B During Loading Path Reversal," *Metall. Mater. Trans. A Phys. Metall. Mater. Sci.*, vol. 46, no. 7, pp. 3079–3090, 2015.

[55] R. W. Hertzberg, *Deformation and fracture mechanics of engineering materials*. NEW YORK: Wiley, 1996.

[56] B. c. Wonsiewicz and W. A. Backofen, "PLASTICITY OF MAGNESIUM CRYSTALS," *Trans. Metall. Soc. Aime*, vol. 239, pp. 1422–1431, 1967.

[57] H. Takuda, H. Fujimoto, and N. Hatta, "Modelling on flow stress of Mg-Al-Zn alloys at elevated temperatures," *J. Mater. Process. Technol.*, vol. 80–81, pp. 513–516, 1998.

[58] Z. X. Guo, *The deformation and processing of structural material*. Woodhead Pub Limited, 2005.

[59] L. Jiang, "EFFECT OF TWINNING ON TEXTURE AND STRAIN," McGill University, 2007.

[60] H. Fan and J. A. El-Awady, "Molecular Dynamics Simulations of Orientation Effects During Tension, Compression, and Bending Deformations of Magnesium Nanocrystals," *J. Appl. Mech.*, vol. 82, no. 10, p. 101006, 2015.

[61] W. Schmid, E., Boas, *Kristallplastizita*. Berlin: t. Julius Springer, 1935.

[62] M. . Yoo, "Slip, twinning, and fracture in hexagonal close packed metals," *Met. Trans*, vol. A12, no. 409–418, 1981.

[63] M. R. Barnett, "Twinning and the ductility of magnesium alloys. Part I: 'Tension' twins," *Mater. Sci. Eng. A*, vol. 464, no. 1–2, pp. 1–7, 2007.

[64] D. W. Brown, S. R. Agnew, M. A. M. Bourke, T. M. Holden, S. C. Vogel, and C. N. Tomé, "Internal strain and texture evolution during deformation twinning in magnesium," *Mater. Sci. Eng. A*, vol. 399, no. 1–2, pp. 1–12, 2005.

[65] M. R. Barnett, "Twinning and the ductility of magnesium alloys. Part II. 'Contraction'

twins," *Mater. Sci. Eng. A*, vol. 464, no. 1–2, pp. 8–16, 2007.

[66] E. W. Kelly and W. Hosford, "Plane-strain compression of magesium and magnesium alloy crystals," *Trans Met Soc AIME*, vol. 242, no. 1, pp. 5–13, 1968.

[67] M. R. Barnett, "A taylor model based description of the proof stress of magnesium AZ31 during hot working," *Metall. Mater. Trans. A*, vol. 34, no. 9, pp. 1799–1806, 2003.

[68] S. M. H. Karparvarfard, S. K. Shaha, S. B. Behravesh, H. Jahed, and B. W. Williams, "Microstructure, texture and mechanical behavior characterization of hot forged cast ZK60 magnesium alloy," *J. Mater. Sci. Technol.*, vol. 33, no. 9, pp. 907–918, 2017.

[69] D. Toscano, S. K. Shaha, B. Behravesh, H. Jahed, and B. Williams, "Effect of forging on the low cycle fatigue behavior of cast AZ31B alloy," *Mater. Sci. Eng. A*, vol. 706, no. May, pp. 342–356, 2017.

[70] D. Toscano, S. K. Shaha, B. Behravesh, H. Jahed, and B. Williams, "Effect of Forging on Microstructure, Texture, and Uniaxial Properties of Cast AZ31B Alloy," *J. Mater. Eng. Perform.*, vol. 26, no. 7, pp. 3090–3103, 2017.

[71] A. Hadadzadeh, M. A. Wells, S. K. Shaha, H. Jahed, and B. W. Williams, "Role of compression direction on recrystallization behavior and texture evolution during hot deformation of extruded ZK60 magnesium alloy," *J. Alloys Compd.*, vol. 702, pp. 274–289, 2017.

[72] A. Hadadzadeh, S. K. Shaha, M. A. Wells, H. Jahed, and B. W. Williams, "Microstructure and Texture Evolution During Hot Deformation of Cast-Homogenized ZK60 Magnesium Alloy," *Magnes. Technol. 2017*, pp. 513–519, 2017.

[73] R. Jahadi, M. Sedighi, and H. Jahed, "ECAP effect on the micro-structure and mechanical properties of AM30 magnesium alloy," *Mater. Sci. Eng. A*, vol. 593, pp. 178–184, 2014.

[74] L. Wu, A. Jain, D. W. Brown, G. M. Stoica, S. R. Agnew, B. Clausen, D. E. Fielden, and P. K. Liaw, "Twinning-detwinning behavior during the strain-controlled low-cycle fatigue testing of a wrought magnesium alloy, ZK60A," *Acta Mater.*, vol. 56, no. 4, pp. 688–695, 2008.

[75] W. Muhammad, M. Mohammadi, J. Kang, R. K. Mishra, and K. Inal, "An elasto-plastic constitutive model for evolving asymmetric/anisotropic hardening behavior of AZ31B and ZEK100 magnesium alloy sheets considering monotonic and reverse loading paths," *Int. J. Plast.*, vol. 70, pp. 30–59, 2015.

[76] E. Kalatehmollaei, H. Mahmoudi-Asl, and H. Jahed, "An asymmetric elastic-plastic analysis of the load-controlled rotating bending test and its application in the fatigue life estimation of wrought magnesium AZ31B," *Int. J. Fatigue*, vol. 64, pp. 33–41, 2014.

[77] E. A. Ball and P. B. Prangnell, "Tensile-compressive yield asymmetries in high strength wrought magnesium alloys," *Scr. Metall. Mater.*, vol. 31, no. 2, pp. 111–116, 1994.

[78] C. Lv, T. Liu, D. Liu, S. Jiang, and W. Zeng, "Effect of heat treatment on tension-compression yield asymmetry of AZ80 magnesium alloy," *Mater. Des.*, vol. 33, no. 1, pp. 529–533, 2012.

[79] J. Casey and H. Jahedmotlagh, "The strength-differential effect in plasticity," *Int. J. Solids Struct.*, vol. 20, no. 4, pp. 377–393, 1984.

[80] J. F. Shackelford, *Introduction to materials science for engineers*. Prentice Hall, 2009.

[81] H. T. Jeong and T. K. Ha, "Texture development in a warm rolled AZ31 magnesium alloy," *J. Mater. Process. Technol.*, vol. 187–188, pp. 559–561, 2007.

[82] M. T. Tucker, M. F. Horstemeyer, P. M. Gullett, H. El Kadiri, and W. R. Whittington, "Anisotropic effects on the strain rate dependence of a wrought magnesium alloy," *Scr. Mater.*, vol. 60, no. 3, pp. 182–185, 2009.

[83] J. Albinmousa, H. Jahed, and S. Lambert, "Cyclic axial and cyclic torsional behaviour of extruded AZ31B magnesium alloy," *Int. J. Fatigue*, vol. 33, no. 11, pp. 1403–1416, 2011.

[84] A. S. Khan, A. Pandey, T. Gnäupel-Herold, and R. K. Mishra, "Mechanical response and texture evolution of AZ31 alloy at large strains for different strain rates and temperatures," *Int. J. Plast.*, vol. 27, no. 5, pp. 688–706, 2011.

[85] J. Bohlen, M. R. Nurnberg, J. W. Senn, D. Letzig, and S. R. Agnew, "The texture and anisotropy of magnesium-zinc-rare earth alloy sheets," *Acta Mater.*, vol. 55, no. 6, pp. 2101–2112, 2007.

[86] S. B. Behravesh, H. Jahed, S. B. Lambert, and M. Chengji, "Constitutive Modeling for Cyclic Behavior of AZ31B Magnesium Alloy and its Application," *Adv. Mater. Res.*, vol. 891, pp. 809–814, 2014.

[87] A. Styczynski, C. Hartig, J. Bohlen, and D. Letzig, "Cold rolling textures in AZ31 wrought magnesium alloy," *Scr. Mater.*, vol. 50, no. 7, pp. 943–947, 2004.

[88] A. N. Chamos, S. G. Pantelakis, G. N. Haidemenopoulos, and E. Kamoutsi, "Tensile and fatigue behaviour of wrought magnesium alloys AZ31 and AZ61," *Fatigue Fract. Eng.*

Mater. Struct., vol. 31, no. 9, pp. 812–821, 2008.

[89] S. B. Behravesh, H. Jahed, and S. Lambert, “Fatigue characterization and modeling of AZ31B magnesium alloy spot-welds,” *Int. J. Fatigue*, vol. 64, pp. 1–13, 2014.

[90] H. Wang, P. D. Wu, and J. Wang, “Modeling inelastic behavior of magnesium alloys during cyclic loading-unloading,” *Int. J. Plast.*, vol. 47, pp. 49–64, 2013.

[91] K. Piao, J. K. Lee, J. H. Kim, H. Y. Kim, K. Chung, F. Barlat, and R. H. Wagoner, “A sheet tension/compression test for elevated temperature,” *Int. J. Plast.*, vol. 38, pp. 27–46, 2012.

[92] A. Jain and S. R. Agnew, “Modeling the temperature dependent effect of twinning on the behavior of magnesium alloy AZ31B sheet,” *Mater. Sci. Eng. A*, vol. 462, no. 1–2, pp. 29–36, 2007.

[93] N. T. Nguyen, O. S. Seo, C. A. Lee, M. G. Lee, J. hoon Kim, and H. Y. Kim, “Mechanical behavior of AZ31B Mg alloy sheets under monotonic and cyclic loadings at room and moderately elevated temperatures,” *Materials (Basel).*, vol. 7, no. 2, pp. 1271–1295, 2014.

[94] H. Wang, P. D. Wu, J. Wang, and C. N. Tomé, “A crystal plasticity model for hexagonal close packed (HCP) crystals including twinning and de-twinning mechanisms,” *Int. J. Plast.*, vol. 49, pp. 36–52, 2013.

[95] R. K. Boger, R. H. Wagoner, F. Barlat, M. G. Lee, and K. Chung, “Continuous, large strain, tension/compression testing of sheet material,” *Int. J. Plast.*, vol. 21, no. 12, pp. 2319–2343, 2005.

[96] N. T. Nguyen, M. G. Lee, J. H. Kim, and H. Y. Kim, “A practical constitutive model for AZ31B Mg alloy sheets with unusual stress-strain response,” *Finite Elem. Anal. Des.*, vol. 76, pp. 39–49, 2013.

[97] S. Begum, D. L. Chen, S. Xu, and A. A. Luo, “Effect of strain ratio and strain rate on low cycle fatigue behavior of AZ31 wrought magnesium alloy,” *Mater. Sci. Eng. A*, vol. 517, no. 1–2, pp. 334–343, 2009.

[98] Y. Ochi, K. Masaki, T. Hirasawa, X. Wu, T. Matsumura, Y. Takigawa, and K. Higashi, “High Cycle Fatigue Property and Micro Crack Propagation Behavior in Extruded AZ31 Magnesium Alloys,” *Mater. Trans.*, vol. 47, no. 4, pp. 989–994, 2006.

[99] S. Ishihara, Z. Nan, and T. Goshima, “Effect of microstructure on fatigue behavior of AZ31 magnesium alloy,” *Mater. Sci. Eng. A*, vol. 468–470, no. SPEC. ISS., pp. 214–222, 2007.

[100] S. Begum, D. L. Chen, S. Xu, and A. A. Luo, “Low cycle fatigue properties of an extruded

AZ31 magnesium alloy," *Int. J. Fatigue*, vol. 31, no. 4, pp. 726–735, 2009.

[101] J. Koike, N. Fujiyama, D. Ando, and Y. Sutou, "Roles of deformation twinning and dislocation slip in the fatigue failure mechanism of AZ31 Mg alloys," *Scr. Mater.*, vol. 63, no. 7, pp. 747–750, 2010.

[102] M. Matsuzuki and S. Horibe, "Analysis of fatigue damage process in magnesium alloy AZ31," *Mater. Sci. Eng. A*, vol. 504, no. 1–2, pp. 169–174, 2009.

[103] S. H. Kim, S. G. Hong, J. H. Lee, C. S. Lee, J. Yoon, H. Yu, and S. H. Park, "Anisotropic in-plane fatigue behavior of rolled magnesium alloy with {10−12} twins," *Mater. Sci. Eng. A*, vol. 700, no. June, pp. 191–197, 2017.

[104] A. Gryguc, S. K. Shaha, H. Jahed, M. Wells, B. Williams, and J. McKinley, "Tensile and fatigue behaviour of as-forged AZ31B extrusion," *Frat. ed Integrita Strutt.*, vol. 10, no. 38, pp. 251–258, 2016.

[105] S. B. Dayani, S. K. Shaha, R. Ghelichi, J. F. Wang, and H. Jahed, "The impact of AA7075 cold spray coating on the fatigue life of AZ31B cast alloy," *Surf. Coatings Technol.*, vol. 337, no. June 2017, pp. 150–158, 2018.

[106] B. Marzbanrad, E. Toyserkani, and H. Jahed, "Cyclic hysteresis of AZ31B extrusion under load-control tests using embedded sensor technology," *Fatigue Fract. Eng. Mater. Struct.*, vol. 40, no. 2, pp. 221–232, Feb. 2017.

[107] J. Albinmousa and H. Jahed, "Multiaxial effects on LCF behaviour and fatigue failure of AZ31B magnesium extrusion," *Int. J. Fatigue*, vol. 67, pp. 103–116, 2014.

[108] J. Wang, D. Ju, F. Yin, and H. Zhao, "Microstructure evaluation and crack initiation crack for AZ31 sheet under biaxial stress," *Procedia Eng.*, vol. 10, pp. 2429–2434, 2011.

[109] F. Yang, S. M. Yin, S. X. Li, and Z. F. Zhang, "Crack initiation mechanism of extruded AZ31 magnesium alloy in the very high cycle fatigue regime," *Mater. Sci. Eng. A*, vol. 491, no. 1–2, pp. 131–136, 2008.

[110] J. Dallmeier, O. Huber, H. Saage, and K. Eigenfeld, "Uniaxial cyclic deformation and fatigue behavior of AM50 magnesium alloy sheet metals under symmetric and asymmetric loadings," *Mater. Des.*, vol. 70, pp. 10–30, 2015.

[111] J. Denk, J. Dallmeier, O. Huber, and H. Saage, "The fatigue life of notched magnesium sheet metals with emphasis on the effect of bands of twinned grains," *Int. J. Fatigue*, vol. 98, pp. 212–222, 2017.

[112] L. Wu, “Mechanical Behavior and the Role of Deformation Twinning in Wrought Magnesium Alloys Investigated Using Neutron and Synchrotron X-ray Diffraction,” University of Tennessee - Knoxville, 2009.

[113] J. P. Immarigeon, R. T. Holt, A. K. Koul, L. Zhao, W. Wallace, and J. C. Beddoes, “Lightweight materials for aircraft applications,” *Mater. Charact.*, vol. 35, no. 1, pp. 41–67, 1995.

[114] J. H. C. HEIKKENEN, FU-SHIONG LIN and E. A. STARKE, “The Low Cycle Fatigue Behavior of High Strength 7XXX-type Aluminum Alloys in the T7351 Condition,” vol. 51, pp. 17–23, 1981.

[115] K. Ohji, W. R. Miller, and J. Marin, “Cumulative Damage and Effect of Mean Strain in Low-Cycle Fatigue of a 2024-T351 Aluminum Alloy,” *J. Basic Eng.*, vol. 88, no. December, pp. 801–810, 1966.

[116] V. Achard, A. Daidie, M. Paredes, and C. Chirol, “Optimization of the Cold Expansion Process for Titanium Holes,” *Adv. Eng. Mater.*, vol. 19, no. 6, pp. 1–13, 2017.

[117] Y. li Wang, Y. li Zhu, S. Hou, H. xiao Sun, and Y. Zhou, “Investigation on fatigue performance of cold expansion holes of 6061-T6 aluminum alloy,” *Int. J. Fatigue*, vol. 95, pp. 216–228, 2017.

[118] S. Suresh, *Fatigue of Materials*. cambridge university press, 1998.

[119] J. L. Phillips, “Sleeve Coldworking of Fastener Holes,” *Air Force Mater. Lab. AFML-TR-74-10*, vol. I, 1974.

[120] M. E. Karabin, F. Barlat, and R. W. Schultz, “Numerical and experimental study of the cold expansion process in 7085 plate using a modified split sleeve,” *J. Mater. Process. Technol.*, vol. 189, no. 1–3, pp. 45–57, 2007.

[121] T. N. Chakherlou and J. Vogwell, “A novel method of cold expansion which creates near-uniform compressive tangential residual stress around a fastener hole,” *Fatigue Fract. Eng. Mater. Struct.*, vol. 27, no. 5, pp. 343–351, 2004.

[122] V. Lacarac, D. J. Smith, M. J. Pavier, and M. Priest, “Fatigue crack growth from plain and cold expanded holes in aluminum alloys,” *Int. J. Fatigue*, vol. 22, no. 3, pp. 189–203, 2000.

[123] J. Liu, H. Wu, J. Yang, and Z. Yue, “Effect of edge distance ratio on residual stresses induced by cold expansion and fatigue life of TC4 plates,” *Eng. Fract. Mech.*, vol. 109, pp. 130–137, 2013.

[124] J. Kang, W. S. Johnson, and D. a Clark, “Three-Dimensional Finite Element Analysis of the Cold Expansion of Fastener Holes in Two Aluminum Alloys,” *J. Eng. Mater. Technol.*, vol. 124, no. 2, pp. 140–145, 2002.

[125] K. Amjad, W.-C. Wang, and E. Patterson, “A comparison of split sleeve cold expansion in thick and thin plates,” *J. Strain Anal. Eng. Des.*, vol. 51, no. 5, pp. 375–386, 2016.

[126] O. Hoffman and G. Sachs, *Introduction to the Theory of Plasticity for Engineers*, vol. New York. 1953.

[127] R. G. Forman and y. C. Hsu, “Elastic-Plastic Analysis of an Infinite Sheet Having a Circular Hole Under Pressure,” *J. Appl. Mech.*, vol. 42, no. 2, pp. 347–352, 1975.

[128] J. Bauschinger, “Ueber die Veranderung der Elasticitatagrenze und dea Elasticitatamoduls verschiadener Metalle,” *Civilingenieur*, vol. 27, pp. 289–348, 1881.

[129] G. Clark, “Modelling Residual Stresses and Fatigue Crack Growth At Cold Expanded Fastener Holes,” *Fatigue Fract. Eng. Mater. Struct.*, vol. 14, no. 5, pp. 579–589, 1991.

[130] G. Clark, “Residual stresses in swage-autofrettaged thick-walled cylinders,” 1982.

[131] Guo Wanlin, “Elastic-plastic analysis of a finite sheet with a cold-worked hole,” *Eng. Fract. Mech.*, vol. 46, no. 3, pp. 465–472, 1993.

[132] M. Heller, R. Jones, and J. F. Williams, “Analysis of cold-expansion for cracked and uncracked fastener holes,” *Eng. Fract. Mech.*, vol. 39, no. 2, pp. 195–212, 1991.

[133] C. Poussard, M. J. Pavier, and D. J. Smith, “Analytical and finite element predictions of residual stresses in cold worked fastener holes,” *J. Strain Anal. Eng. Des.*, vol. 30, no. 4, pp. 291–304, 1995.

[134] A. A. Garcia-Granada, V. Lacarac, D. J. Smith, M. J. Pavier, R. Cook, and P. Holdway, “3D residual stresses around cold expanded holes in a new creep resistant aluminium alloy,” *Trans. Eng. Sci.*, vol. 25, pp. 103–116, 1999.

[135] N. C. Mahendra Babu, T. Jagadish, K. Ramachandra, and S. N. Sridhara, “A simplified 3-D finite element simulation of cold expansion of a circular hole to capture through thickness variation of residual stresses,” *Eng. Fail. Anal.*, vol. 15, no. 4, pp. 339–348, 2008.

[136] L. Yongshou, S. Xiaojun, L. Jun, and Y. Zhufeng, “Finite element method and experimental investigation on the residual stress fields and fatigue performance of cold expansion hole,” *Mater. Des.*, vol. 31, no. 3, pp. 1208–1215, 2010.

[137] P. Papanikos and S. A. Meguid, “Elasto-plastic finite-element analysis of the cold expansion

of adjacent fastener holes," *J. Mater. Process. Technol.*, vol. 92–93, pp. 424–428, 1999.

[138] M. Lapalme, M. Hoseini, P. Bocher, A. R. Colle, and M. Lévesque, "Realistic Cold Expansion Finite Element Model and Experimental Validations for Aluminium Alloys," *Exp. Mech.*, vol. 54, no. 5, pp. 841–855, 2014.

[139] X. Yuan, Z. F. Yue, S. F. Wen, L. Li, and T. Feng, "Numerical and experimental investigation of the cold expansion process with split sleeve in titanium alloy TC4," *Int. J. Fatigue*, vol. 77, pp. 78–85, 2015.

[140] P. F. P. De Matos, P. M. G. P. Moreira, P. P. Camanho, and P. M. S. T. De Castro, "Numerical simulation of cold working of rivet holes," *Finite Elem. Anal. Des.*, vol. 41, no. 9–10, pp. 989–1007, 2005.

[141] "FATIGUE LIFE ENHANCEMENT OF HOLES IN METAL STRUCTURES Over 40 Years of Technology Advancement and."

[142] S. J. Houghton and S. K. Campbell, "Identifying the residual stress field developed by hole cold expansion using finite element analysis," *Fatigue Fract. Eng. Mater. Struct.*, vol. 35, no. 1, pp. 74–83, 2012.

[143] T. N. Chakherlou, M. Shakouri, A. B. Aghdam, and A. Akbari, "Effect of cold expansion on the fatigue life of Al 2024-T3 in double shear lap joints: Experimental and numerical investigations," *Mater. Des.*, vol. 33, no. 1, pp. 185–196, 2012.

[144] S. Ismonov, S. R. Daniewicz, J. Newman J. C., M. R. Hill, and M. R. Urban, "Three Dimensional Finite Element Analysis of a Split-Sleeve Cold Expansion Process," *J. Eng. Mater. Technol.*, vol. 131, no. 3, p. 31007, 2009.

[145] M. Burlat, "Effect of Re-Coldworking on Fatigue Life Enhancement of a Fastener Hole," vol. 18, no. 7, pp. 765–775, 1995.

[146] M. Elajrami, R. Miloud, H. Melouki, and F. B. Boukhoulda, "Numerical study of the effect of double cold expansion of rivet hole on the residual stresses distribution," *Proc. Inst. Mech. Eng. Part B J. Eng. Manuf.*, vol. 227, no. 4, pp. 621–626, 2013.

[147] M. Su, A. Amrouche, G. Mesmacque, and N. Benseddiq, "Numerical study of double cold expansion of the hole at crack tip and the influence on the residual stresses field," *Comput. Mater. Sci.*, vol. 41, no. 3, pp. 350–355, 2008.

[148] M. Burlat, D. Julien, M. Lévesque, T. Bui-Quoc, and M. Bernard, "Effect of local cold working on the fatigue life of 7475-T7351 aluminium alloy hole specimens," *Eng. Fract.*

Mech., vol. 75, no. 8, pp. 2042–2061, 2008.

[149] C. P. Stack and R. I. Stephens, “Effect of split-sleeve cold-expansion on the fatigue resistance of hot-rolled 1020 steel,” *Int. J. Fatigue*, vol. 11, no. 5, pp. 327–334, 1989.

[150] J. M. Mínguez and J. Vogwell, “Fatigue life of an aerospace aluminium alloy subjected to cold expansion and a cyclic temperature regime,” *Eng. Fail. Anal.*, vol. 13, no. 6, pp. 997–1004, 2006.

[151] D. L. Ball and D. R. Lowry, “Experimental Investigation on the Effects of Cold Expansion of Fastener Holes,” *Fatigue Fract. Eng. Mater. Struct.*, vol. 21, no. 1, pp. 17–34, 1998.

[152] M. S. Rana, C. Makabe, and G. Fujiwara, “The effect of hole shape on the extent of fatigue life improvement by cold expansions,” *Eng. Fail. Anal.*, vol. 16, no. 7, pp. 2081–2090, 2009.

[153] V. Achard, A. Daidie, M. Paredes, and C. Chirol, “Cold expansion process on hard alloy holes-experimental and numerical evaluation,” *Mech. Ind.*, vol. 17, no. 3, p. 303, 2016.

[154] V. . Lacarac, D. . Smith, and M. . Pavier, “The effect of cold expansion on fatigue crack growth from open holes at room and high temperature,” *Int. J. Fatigue*, vol. 23, pp. 161–170, 2001.

[155] W. Z. Yan, X. S. Wang, H. S. Gao, and Z. F. Yue, “Effect of split sleeve cold expansion on cracking behaviors of titanium alloy TC4 holes,” *Eng. Fract. Mech.*, vol. 88, pp. 79–89, 2012.

[156] A. T. ÖZdemir and L. Edwards, “Relaxation of Residual Stresses At Cold-Worked Fastener Holes Due To Fatigue Loading,” *Fatigue Fract. Eng. Mater. Struct.*, vol. 20, no. 10, pp. 1443–1451, 1997.

[157] J. M. M. J. Vogwell, T Navid-Chakherlou, “The Effect of Cold Expansion on the Fatigue resistance of fastener holes,” *10th Int. Congr. Fract.*, vol. 130, no. 3, p. 7, 2008.

[158] M. Elajrami, R. Miloud, H. Milouki, and F. B. Boukhoulda, “Experimental investigation of the effect of double cold expansion on the residual stresses distribution and on the fatigue life of rivet hole,” *J. Brazilian Soc. Mech. Sci. Eng.*, vol. 38, no. 8, pp. 2527–2532, 2016.

[159] D. Stefanescu, “Experimental study of double cold expansion of holes,” *J. Strain Anal. Eng. Des.*, pp. 339–347, 2003.

[160] H. D. Gopalakrishna, H. N. Narasimha Murthy, M. Krishna, M. S. Vinod, and a. V. Suresh, “Cold expansion of holes and resulting fatigue life enhancement and residual stresses in Al

2024 T3 alloy - An experimental study," *Eng. Fail. Anal.*, vol. 17, no. 2, pp. 361–368, 2010.

[161] A. Amrouche, G. Mesmacque, S. Garcia, and A. Talha, "Cold expansion effect on the initiation and the propagation of the fatigue crack," *Int. J. Fatigue*, vol. 25, no. 9–11, pp. 949–954, 2003.

[162] A. Amrouche, M. Su, A. Aid, and G. Mesmacque, "Numerical study of the optimum degree of cold expansion: Application for the pre-cracked specimen with the expanded hole at the crack tip," *J. Mater. Process. Technol.*, vol. 197, no. 1–3, pp. 250–254, 2008.

[163] S. Pasta, "Fatigue crack propagation from a cold-worked hole," *Eng. Fract. Mech.*, vol. 74, no. 9, pp. 1525–1538, 2007.

[164] T. Ozdemir and L. Edwards, "Through-Thickness Residual Stress Distribution After the Cold Expansion of Fastener Holes and Its Effect on Fracturing," *J. Eng. Mater. Technol.*, vol. 126, no. 1, p. 129, 2004.

[165] Nadai, *Plasticity*. London: McGraw-Hill.

[166] H. Jahed, R. Sethuraman, and R. N. Dubey, "A variable material property approach for solving elastic-plastic problems," *Int. J. Press. Vessel. Pip.*, vol. 71, no. 3, pp. 285–291, 1997.

[167] S. Faghih, H. Jahed, and S. B. Behravesh, "Variable Material Properties (VMP) Approach: A Review on Twenty Years of Progress," *J. Press. Vessel Technol.*, 2018.

[168] H. Jahed and M. Noban, "ch04 Proportional analysis of non-proportional loadings," *Adv. Fatigue, Fract. Damage Assess. Mater.*, vol. 1, pp. 15–53, 2005.

[169] H. Jahed, S. B. Lambert, and R. N. Dubey, "Total Deformation Theory for Non Proportional Loading," *Int. J. Press. Vessel. Pip.*, vol. 75, no. 8, pp. 633–642, 1998.

[170] M. Noban, H. Jahed, E. Ibrahim, and A. Ince, "Load path sensitivity and fatigue life estimation of 30CrNiMo8HH," *Int. J. Fatigue*, vol. 37, pp. 123–133, 2012.

[171] A. P. Parker, "A Re-Autofrettage Procedure for Mitigation of Bauschinger Effect in Thick Cylinders," *J. Press. Vessel Technol.*, vol. 126, no. 4, pp. 451–454, 2004.

[172] A. P. Parker, "An Improved Method for Recovering Residual Stress From Strain Measurements in Cylinders and Rings," *Vol. 5 High Press. Technol. Nondestruct. Eval. Pipeline Syst. Student Pap. Compet.*, vol. 2006, pp. 133–138, 2006.

[173] M. C. Gibson, A. Hameed, J. G. Hetherington, and A. P. Parker, "Custom Material Modeling within FEA for use in Autofrettage Simulation," in *ASME 2007 Pressure Vessels*

and Piping Conference (PVP2007), 20077, pp. 19–35.

[174] H. Jahed, B. A. Moghadam, and M. Shambooli, “Re-Autofrettage,” *J. Press. Vessel Technol.*, vol. 128, no. 2, p. 223, 2006.

[175] H. Jahed, M. R. Faritus, and Z. Jahed, “Residual Stress Measurements in an Autofrettage Tube Using Hole Drilling Method,” *J. Press. Vessel Technol.*, vol. 134, no. 5, p. 51501, 2012.

[176] M. Maleki, G. H. Farrahi, B. Haghpanah Jahromi, and E. Hosseinian, “Residual stress analysis of autofrettaged thick-walled spherical pressure vessel,” *Int. J. Press. Vessel. Pip.*, vol. 87, no. 7, pp. 396–401, 2010.

[177] A. P. Parker and X. Huang, “Autofrettage and Reautofrettage of a Spherical Pressure Vessel,” *J. Press. Vessel Technol.*, vol. 129, no. February 2007, p. 83, 2007.

[178] H. Darijani, N. Shamsaei, R. Naghdabadi, and M. D. Sararoudi, “Elastoplastic stress study in thick-walled spherical vessels considering finite deformation,” in *Proceedings of 8th Biennial ASME Conference on Engineering Systems Design and Analysis*, 2006, pp. 475–482.

[179] A. P. Parker and X. Huang, “Autofrettage of a Spherical Pressure Vessel,” *J. Press. Vessel Technol.*, vol. 129, p. 83, 2007.

[180] M. Mohammadi, G. H. Farrahi, and S. H. Hoseini, “Material Removal Simulation of Aluminum Compound Tubes With Incorporating Real Unloading Behavior,” in *Pressure Vessels and Piping Division Conference*, 2007, vol. 3, pp. 195–201.

[181] A. P. Parker, “Compound and Monobloc Cylinders Incorporating Reverse-Autofrettage to Reduce External Hoop Stresses,” in *Pressure Vessels & Piping Conference*, 2012, pp. 213–220.

[182] A. P. Parker, “Bauschinger Effect Design Procedures for Compound Tubes Containing an Autofrettaged Layer,” *J. Press. Vessel Technol.*, vol. 123, no. 2, pp. 203–206, 2001.

[183] M. R. Farimani and H. E. Toussi, “Plastic limit speed of FGM disc due to the variation of temperature and material composition,” *J. Reinf. Plast. Compos.*, vol. 32, no. 17, pp. 1257–1267, 2013.

[184] M. H. Hojjati and a. Hassani, “Theoretical and numerical analyses of rotating discs of non-uniform thickness and density,” *Int. J. Press. Vessel. Pip.*, vol. 85, no. 10, pp. 694–700, 2008.

[185] S. Sherkati and H. Jahed, “Thermoplastic Analysis of Inhomogeneous Rotating Disk with Variable Thickness,” in *Proceeding of the EMAS Conference of Fatigue*, 2000, pp. 229–238.

[186] B. Farshi and J. Bidabadi, “Optimum Design of Inhomogeneous Rotating Disks for Minimum Creep Induced Radial Displacement,” *J. Press. Vessel Technol.*, vol. 133, no. 5, p. 51206, 2011.

[187] B. Farshi and J. Bidabadi, “Optimum design of inhomogeneous rotating discs under secondary creep,” *Int. J. Press. Vessel. Pip.*, vol. 85, no. 7, pp. 507–515, 2008.

[188] B. H. Jahromi, H. Nayeb-Hashemi, and A. Vaziri, “Elasto-plastic stresses in a functionally graded rotating disk,” *J. Eng. Mater. Technol.*, vol. 134, no. 2, p. 21004, 2012.

[189] B. Haghpanah Jahromi, G. H. Farrahi, M. Maleki, H. Nayeb-Hashemi, and a. Vaziri, “Residual stresses in autofrettaged vessel made of functionally graded material,” *Eng. Struct.*, vol. 31, no. 12, pp. 2930–2935, 2009.

[190] B. H. Jahromi, a. Ajdari, H. Nayeb-Hashemi, and a. Vaziri, “Autofrettage of layered and functionally graded metal-ceramic composite vessels,” *Compos. Struct.*, vol. 92, no. 8, pp. 1813–1822, 2010.

[191] Y. T. Gu, Q. X. Wang, K. Y. Lam, and K. Y. Dai, “A pseudo-elastic local meshless method for analysis of material nonlinear problems in solids,” *Eng. Anal. Bound. Elem.*, vol. 31, no. 9, pp. 771–782, 2007.

[192] X. Y. Cui, G. R. Liu, G. Y. Li, G. Y. Zhang, and G. Y. Sun, “Analysis of elastic-plastic problems using edge-based smoothed finite element method,” *Int. J. Press. Vessel. Pip.*, vol. 86, no. 10, pp. 711–718, 2009.

[193] H. Jahed, S. B. Lambert, and R. N. Dubey, “Variable material property method in the analysis of cold-worked fastener holes,” *J. Strain Anal. Eng. Des.*, vol. 35, no. 2, pp. 137–142, 2000.

[194] H. Jahed and G. Ghanbari, “Actual Unloading Behavior and Its Significance on Residual Stress in Machined Autofrettaged Tubes,” *J. Press. Vessel Technol.*, vol. 125, no. 3, pp. 321–325, 2003.

[195] E. Kalateh Mollaei and H. Jahed, “Load Controlled Fatigue of AZ31B,” *J. Mech. Res. Appl.*, vol. 4, no. 2, pp. 41–47, 2013.

[196] B. Marzbanrad, “Behaviour of Magnesium Alloy Under Load-Control Cyclic Testing,”

University of Waterloo, 2015.

[197] H. Jahed and M. A. Khayamian, “An Anisotropic Axisymmetric Model for Wrought Magnesium Alloys,” *Int. J. Adv. Des. Manuf. Technol.*, vol. 5, no. 4, pp. 7–11, 2012.

[198] O. Cazacu and F. Barlat, “A criterion for description of anisotropy and yield differential effects in pressure-insensitive metals,” *Int. J. Plast.*, vol. 20, no. 11 SPEC. ISS., pp. 2027–2045, 2004.

[199] “Standard Test Methods for Tension Testing of Metallic Materials 1,” 2009.

[200] A. Yazdanmehr and H. Jahed, “Large strain compression-tension behavior of AZ31B rolled sheet in the rolling direction,” *UNPUBLISHED*.

[201] “west coast industry, engineering handout,WCI-EH92-4.1.”

[202] I. C. Noyan and J. B. Cohen, *Residual Stress - Measurement by Diffraction and Interpretation*. Springer Science+Business Media,LLC, 2013.

[203] M. J. Pavier, C. G. C. Poussard, and D. J. Smith, “Effect of residual stress around cold worked holes on fracture under superimposed mechanical load,” *Eng. Fract. Mech.*, vol. 63, no. 6, pp. 751–773, 1999.

[204] N. J. Rendler and I. Vigness, “Hole-drilling strain-gage method of measuring residual stresses,” *Exp. Mech.*, vol. 6, no. 12, pp. 577–586, 1966.

[205] H. Jahed, M. R. Faritus, and Z. Jahed, “Residual Stress Measurements in an Autofrettage Tube Using Hole Drilling Method,” *J. Press. Vessel Technol.*, vol. 134, no. 5, p. 51501, 2012.

[206] B. B. He, *Two-Dimensional X-Ray Diffraction*. John Wiley & Sons, 2009.

[207] W. C. Young and R. G. Budynas, *Roark’s Formulas for Stress and Strain*, vol. 7, no. 7th Edition. McGraw-Hill, 2002.

[208] T. Watanabe, “Grain Boundary Sliding and Stress Concentration during Creep,” *Metall. Trans. A*, vol. 14, no. April, pp. 531–545, 1983.

[209] J. Koike, R. Ohyama, T. Kobayashi, M. Suzuki, and K. Maruyama, “Grain-Boundary Sliding in AZ31 Magnesium Alloys at Room Temperature to 523 K,” *Mater. Trans.*, vol. 44, no. 4, pp. 445–451, 2003.

[210] A. Brückner-Foit and X. Huang, “Numerical simulation of micro-crack initiation of martensitic steel under fatigue loading,” *Int. J. Fatigue*, vol. 28, no. 9, pp. 963–971, 2006.

[211] Y. Xiong, “Microstructure damage evolution associated with cyclic deformation for

extruded AZ31B magnesium alloy," *Mater. Sci. Eng. A*, vol. 675, pp. 171–180, 2016.

[212] W. J. Kim and Y. K. Sa, "Micro-extrusion of ECAP processed magnesium alloy for production of high strength magnesium micro-gears," *Scr. Mater.*, vol. 54, no. 7, pp. 1391–1395, 2006.

[213] G. Ben Hamu, D. Eliezer, and L. Wagner, "The relation between severe plastic deformation microstructure and corrosion behavior of AZ31 magnesium alloy," *J. Alloys Compd.*, vol. 468, no. 1–2, pp. 222–229, 2009.

[214] A. Krishnaiah, U. Chakkingal, and P. Venugopal, "Production of ultrafine grain sizes in aluminium sheets by severe plastic deformation using the technique of groove pressing," *Scr. Mater.*, vol. 52, no. 12, pp. 1229–1233, 2005.

[215] P. Paris and F. Erdogan, "A critical analysis of crack propagation laws," *ASME J. Basic ENgrg.*, vol. 85, pp. 528–534, 1963.

[216] M. D. Sangid, "The physics of fatigue crack initiation," *Int. J. Fatigue*, vol. 57, pp. 58–72, 2013.

[217] D. V. Hutton, *Fundamentals of finite element analysis*. 2003.

[218] O. Cazacu, B. Plunkett, and F. Barlat, "Orthotropic yield criterion for hexagonal closed packed metals," *Int. J. Plast.*, vol. 22, no. 7, pp. 1171–1194, 2006.

[219] N. Chandola, R. A. Lebensohn, O. Cazacu, B. Revil-Baudard, R. K. Mishra, and F. Barlat, "Combined effects of anisotropy and tension-compression asymmetry on the torsional response of AZ31 Mg," *Int. J. Solids Struct.*, vol. 58, pp. 190–200, 2015.